Soil Moisture Map Construction by Sequential Data Assimilation Using an Extended Kalman Filter

by

Bernard Agyeman

A thesis submitted in partial fulfillment of the requirements for the degree of

Master of Science
in
Process Control

Department of Chemical and Materials Engineering

University of Alberta

Abstract

In response to rapid population growth and increased population densities, changes must occur in agriculture to meet the higher food demand. With a limited potential to increase arable cropland, irrigation has become an increasingly important tool to ensure sufficient global food supply. Increased levels of irrigation put more pressure on freshwater supply. Currently, the water-use efficiency in irrigation is estimated to be between 50% to 60% due to poor irrigation practices. A critical step towards mitigating the freshwater supply crisis is to increase the water-use efficiency in irrigation through precision irrigation. One important step towards precision irrigation is to close the irrigation decision loop to form a closed-loop irrigation system. To implement closed-loop irrigation, moisture sensing techniques must be employed to provide the required soil moisture information for feedback control. In the context of obtaining soil moisture measurements, microwave remote sensing can be useful and has demonstrated the capability of inferring the near-surface soil moisture quantitatively. Microwave sensors mounted on center pivot irrigation systems provide a feasible approach to measure soil moisture content. These sensors measure the moisture content as the center pivot rotates and provide the moisture information in the form of water content maps at the end of the pivot's rotation cycle. There however exist three main challenges with this approach which reduce the usability of the soil water content maps in the implementation of closed-loop irrigation. Firstly, it takes between two to three days for a center pivot to complete one rotation cycle which means that it also takes between two to three days to obtain a single water content map from the microwave sensors. This significant time delay in the soil moisture measurements means that continuous feedback and control cannot be effectively implemented. Secondly, the current approach lacks a predictive capability in the sense that the sensors cannot provide soil moisture information when the center pivot is stationary. Lastly, the current approach does not provide moisture information in the root zone, knowledge of which is required for closed-loop irrigation. This work seeks to find solutions to the aforementioned challenges and consequently propose a water content map construction procedure that is suitable for the implementation of closed-loop irrigation. Firstly, we propose an agro-hydrological modeling framework, specifically the cylindrical coordinates version of the Richards equation, which can naturally model a field equipped with a center pivot irrigation system. The measurements obtained from the microwave sensors are then integrated with the field model and a state estimator, the Extended Kalman filter, to form an information fusion system that will provide frequent estimates and predictions of soil moisture in the form of moisture content maps. The proposed information fusion system is first investigated with simulated microwave sensor measurements where its performance is analyzed based on extensive simulations. The information fusion system is then applied to a real case study where soil moisture measurements from passive microwave sensors are considered. We demonstrate the effectiveness of the proposed solution in effectively dealing with the challenges. Three performance evaluation criteria are used to validate the soil moisture estimates and predictions provided by the proposed information fusion system.

Acknowledgments

First and foremost, I thank God, the Almighty, for providing me the opportunity to undertake this research study and granting me the ability to complete it successfully.

My sincerest gratitude goes to my supervisor, Dr. Jinfeng Liu, for his guidance and support during my graduate study. At many stages during this research work, I benefited from his advice and his belief in my research topic inspired me.

I would like to thank all my colleagues from Process Systems and Control Engineering group for their support. Special thanks to Benjamin Decardi-Nelson, Song Bo, Soumya Sahoo, Xunyuan Yin, Jannatun Nahar, Su Liu, An Zhang, Jianbang Liu, Yi Zhang, Guoyang Yan, Rui Nian, Erfan Orouskhani, Sarupa Debnath, Aristarchus Gnanasekar, and Zhiyinan Huang.

I would also like to thank my parents and my siblings for their unconditional love and support. I would like to thank my friends, Amma Asantewaa Agyei Boakye and Benjamin Amoako, for their advice and support.

I would like to thank Ted Hams, Len Hingley, Jim Parker, Michael Ellefson, Steve Larocque, and Maik Wolleben for their assistance during the data collection and preprocessing. I would like to gratefully acknowledge financial support from the Natural Sciences and Engineering Research Council (NSERC) of Canada and Alberta Innovates.

Contents

List of Tables

List of Figures

Chapter 1

Introduction

1.1 Motivation

Over the last century, the world has witnessed a rapid increase in its population: from 1.8 billion in 1915 to 7.5 billion in 2017 [1]. The world's population is projected to increase by 31 percent from its current estimate of 7.7 billion to 9.8 billion by 2050 [2]. Over the same period, the average per capita income is also expected to rise [3]. Jointly, these two developments are driving up the global demand for food.

Freshwater and arable land constitute two of the most fundamental resources for food production. There is however a restriction on cropland expansion in the wake of the high global demand for food due to the high ecological and social trade-offs of clearing more land for agriculture [4]. With a limited potential to increase suitable cropland, agricultural irrigation becomes an increasingly important tool to ensure a sufficient global supply of food in the near future [5]. The expansion of irrigation will put further stress on rivers, lakes, and aquifers that are already depleted, raising concerns about the ability of the Earth to feed humans with its limited freshwater resources.

According to the United Nations, agriculture accounts for more than 70 percent of anthropogenic water withdrawals, with the main consumer being irrigation [6]. Currently, the water-use efficiency in irrigation is about 60 percent [7], which means that a significant portion of the water used in irrigation is wasted due to inefficient irrigation practices. Ensuring the near-optimal use of water through increased water-use efficiency in irrigation represents a popular and effective approach to reduce water losses in agricultural irrigation, thus mitigating the current water supply crisis. The above considerations motivate this thesis.

1.2 Problem Statement

Currently, most irrigation systems are implemented in an open-loop fashion. In an open-loop system, the operator makes the decision on the amount of water to be applied and the timing of the irrigation event. These decisions are made based on the operator's empirical knowledge of the crop's water requirements, soil type, and climatic factors. This one-way information flow approach often leads to excessive consumption of water resources. Closed-loop irrigation is a promising alternative to improve the water-use efficiency in irrigation and consequently reduce the consumption and wastage of water resources. In closed-loop systems, the operator develops a control strategy that takes over and makes detailed decisions on when to apply water and how much water to apply. Irrigation decisions are made and actions are carried out based on real-time soil moisture information as well as climatic and crop information. In this type of system, the feedback and control of the system are done continuously.

To implement closed-loop irrigation, various moisture sensing techniques must be employed to provide the required soil moisture information for feedback control. In-situ moisture probes are the most mature and reliable soil moisture sensing technique. These sensors are portable, easy to install and operate, and can provide continuous measurements at various depths of the field. However, it is very expensive to obtain a thorough water distribution of a large-scale field using these probes [8, 9, 10]. Non-invasive sensing techniques provide a more practical approach to capture the spatial variability of soil moisture. Some techniques in this category include ground penetrating radars, electrical resistivity tomography, electromagnetic induction, and microwave remote sensing.

Microwave soil moisture sensors have been demonstrated to have the capability of measuring the near-surface soil moisture quantitatively, providing soil moisture information for feedback control. Microwave sensors mounted on center pivots provide a feasible approach to measure the soil water content of fields equipped with center pivots irrigation systems. These sensors measure the soil moisture content at different locations of the field as the center pivot rotates and provide the soil moisture information in the form of soil water content maps at the end of the pivot's rotation cycle.

(a) Sensors on a center pivot. (b) Sample field. (c) Water content map.

Figure 1.1: Current microwave remote sensing approach.

Figure 1.1(c) shows the soil water content map generated by microwave sensors mounted on a center pivot shown in Figure 1.1(a) for the field shown in Figure 1.1(b).

There however exist three main challenges associated with this approach which reduce the usability of the soil water content maps in the implementation of closed-loop irrigation. Firstly, it takes between two to three days for a center pivot to complete one rotation cycle. This means that it also takes between two to three days to obtain a single water content map from the microwave sensors. This significant time delay in the soil moisture measurements means that continuous feedback and control cannot be effectively implemented. Secondly, the current approach lacks a predictive capability in the sense that the sensors cannot provide soil moisture information of the field when the center pivot is stationary. Lastly, the current approach cannot provide soil moisture information at greater depths below the soil surface. As a result, with the current approach, it is not possible to obtain soil moisture information in the root zone, knowledge of which is required for feedback control.

1.3 Proposed Solutions

This thesis seeks to improve the usability of the soil water content information provided by the microwave sensors in the implementation of closed-loop irrigation by addressing the three challenges associated with the current sensing approach. It aims to reduce the significant time delay associated with the current approach by constructing frequently updated water content maps, with update frequencies up to a few minutes, using the soil moisture information obtained from the microwave sensors. It also aims to incorporate a predictive capability into the current approach by proposing a suitable agro-hydrological framework or field model which can make soil moisture predictions based on the prevailing field conditions, in instances when the center pivot is stationary. Finally, it aims to provide soil moisture information at greater depths below the field surface and hence the root zone by integrating the soil moisture measurements provided by the microwave sensors with the field model.

1.4 Objectives

To address the aforementioned challenges, this thesis sets out to meet the following specific objectives:

- To develop an agro-hydrological framework, a field model, that naturally describes fields equipped with center pivots.
- To integrate the measurements from the microwave sensors, a state estimator, and the field model to form an information fusion system that will construct a soil water

content map to provide frequent soil water estimates and predictions.

Figure 1.2 provides a schematic and summary of the objectives that this thesis seeks to achieve.

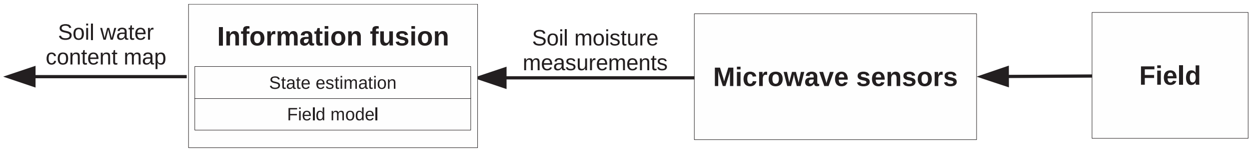

Figure 1.2: A schematic diagram illustrating the research objectives.

1.5 Thesis Outline and Contributions

This thesis is presented in 5 chapters, including this introductory chapter. Chapter 2 summarizes the available literature on several topics related to this work. In particular, it includes a summary of current soil water sensing technologies, a detailed description of the microwave remote sensing technique, and a summary of soil moisture estimation strategies. In Chapter 3, the Richards equation is considered as the field model for soil moisture predictions and estimation. Firstly, it is expressed in cylindrical coordinates, resulting in a partial differential equation (PDE). A finite difference (FD) scheme of the resulting PDE is developed. The Extended Kalman filter (EKF) estimation algorithm is also introduced. A simulation case study is described and the performance of the proposed approach is extensively studied based on simulations. In Chapter 4, actual measurements provided by microwave sensors mounted on a center pivot are considered. Data preprocessing methods carried out on the raw data are outlined. The measurements are then combined with the field model in the proposed information fusion system. The ability of the proposed approach to provide frequently updated maps is demonstrated together with its ability to provide soil moisture predictions. The chapter also demonstrates the ability of the proposed approach to provide soil moisture information at greater depths below the soil surface. The chapter concludes with a demonstration of the accuracy and consistency of the soil moisture estimates provided by the proposed approach. Chapter 5 provides a conclusion and suggestions for future work.

Chapter 2

Literature Review

The literature review consists of four sections. Section 1 is a review of the current soil moisture sensing technologies. Section 1 is further divided into two subsections where the two main types of soil moisture sensing categories are discussed. Section 2 provides a detailed discussion of microwave remote sensing. It is divided into three subsections where the two main types of microwave remote sensing (passive and active) are discussed in the first two subsections. The third subsection describes one of the major challenges associated with microwave remote sensing, which happens to be one of the challenges that this thesis seeks to address. In Section 3, soil moisture estimation is discussed. The chapter concludes with a summary of the review in Section 4.

2.1 Soil Moisture Sensing Technologies

The accurate quantification of soil moisture content is critical for developing closed-loop irrigation systems. Soil moisture content refers to the amount of water held within a unit of soil over a period of time. Soil water can be defined based on volume "volumetric moisture content (θ_v)" or mass "gravimetric moisture content (θ_w)". For irrigation purposes, the volumetric water content is typically used since (θ_v) is defined in terms of depth of water, which is similar to the irrigation application depth.

The volumetric moisture content in a unit of soil is directly measured using the gravimetric method [sometimes referred to as (thermo-) gravimetric method] in soil laboratories. The gravimetric method is the oldest and most direct method currently used for soil water content measurements and it remains the standard against which other methods are calibrated and compared [11, 12]. In this method, a known volume of soil (V_b) is dried at 221°F (105°C) until a constant weight is achieved [13]. The volume of water loss (V_w) is determined by recording the weight of the soil prior to and after the drying. The volumetric moisture content (θ_v) is obtained by solving Equation (2.1).

$$\theta_v = \frac{V_w}{V_b} \tag{2.1}$$

Even though the gravimetric method is one of the most reliable methods, it can be destructive (because soil samples must be removed from the field), time-consuming, expensive, and noncontinuous in nature. Thus, the gravimetric method is not suitable for the real-time monitoring of soil moisture. Consequently, other methods and technologies have been developed to measure the status of soil moisture. These methods do not directly measure the soil moisture content, but instead, estimate the volumetric moisture content from another property using a calibration equation.

2.1.1 Point Soil Moisture Measurement Methods

Among the indirect soil moisture measurement methods, the most mature and reliable techniques are the point measurement methods. The most common point measurement methods are the electromagnetic (EM) methods. The EM techniques are based on the dependency of the soil dielectric permittivity on the water content of the soil. The dielectric permittivity of liquid water dominates the dielectric permittivity of other soil components, thus water is the principal factor dictating the propagation of EM waves in soil. EM techniques include time- or frequency-domain reflectometry (TDR or FDR), time or frequency-domain transmissometry (TDT or FDT), as well as capacitance and impedance methods.

The TDR measurement principle is based on the propagation velocity of guided EM waves emitted by a pulse generator and propagated along the waveguides of the TDR probe into the soil. The propagation velocity is obtained by measuring the travel time along a known length of the TDR probe. The travel time depends on the electromagnetic properties of the soil [14]. Like the TDR, TDT sensors also measure the propagation velocity of EM waves, but, in this case, the EM waves travel along a closed transmission line. The measurement principle of the capacitance sensor is to measure soil moisture content through its effect on the dielectric constant by measuring the capacitance between two electrodes implanted in the soil using a system of probes [15]. A frequency excitation is usually given to the installed probes to enable the measurement of the dielectric constant. Typically, capacitance and impedance sensors operate at a frequency between 50 and 150 MHz, while TDR/FDR and TDT/FDT sensors operate at higher frequencies. TDR/FDR and TDT/FDT sensors are generally considered more accurate than the capacitance and impedance sensors since their measurements are less likely to be influenced by the electrical conductivity and the imaginary dielectric permittivity of the soil.

Other point methods are also available, such as neutron probes, which estimate soil moisture by measuring the number of hydrogen nuclei in soils; heat pulse sensors, which are based on the estimation of the thermal properties of soil; and fiber optic sensors, which rely on the attenuation or reflection of a light signal in the soil.

Point instruments can perform continuous nondestructive measurements of soil moisture content over a wide range of soils and with a very high temporal resolution. They are also portable, easy to install, and easy to operate. However, they are all invasive methods, which means they are restricted to local observation areas (less than 1 m^2), and may not be representative of the soil moisture variability within the field. Another disadvantage of point sensors is that they are expensive.

2.1.2 Non-invasive Sensing Techniques

These are contactless sensing techniques that allow the continuous determination of soil moisture from field to catchment scales. They provide a more feasible approach to capture the spatial variability of soil moisture.

Non-invasive sensing techniques include geophysical methods such as the ground penetrating radar (GPR), electromagnetic induction (EMI), and electrical resistivity tomography (ERT). These geophysical methods allow for measuring different soil electrical properties such as electrical conductivity or resistivity, which can be translated to the soil moisture using various petrophysical models [16]. Conventional GPR systems consist of two antennas: a transmitting antenna that emits high frequency (1 MHz to 1 GHz) electromagnetic waves into the subsurface, and a receiving antenna that detects the back-propagating electromagnetic waves [17]. The propagation velocity of the electromagnetic waves is used to determine the soil dielectric permittivity, which is directly related to soil moisture content [18]. An EMI system measures the ground electrical conductivity and it has a receiver at one end and a transmitter loop at the other. The transmitter end is energized and this creates magnetic field loops in the ground. These magnetic loops produce electrical field loops, which in turn create a secondary magnetic field. At low induction numbers, the combined primary and secondary magnetic fields measured in the receiver are proportional to the ground electrical conductivity [19]. The ground electrical conductivity obtained with the EMI is influenced by soil properties such as salinity, temperature, and soil moisture content [20]. The ERT technique is a direct current (or low-frequency alternating current) method of determining the electrical resistivity in soil, where electrodes are inserted in the ground [13]. Soil moisture content can then be determined using the electrical resistivity measurements provided by the ERT.

Remotely sensed measurements of soil moisture are made using instruments that do not come into direct contact with the soil. Changes in soil moisture are inferred through the soil's influence on potential fields, such as the electric, magnetic, and gravitational fields.

There are two main advantages of remote sensing: the ability to make measurements over large spatial areas with a single instrument on mobile support (such as a satellite or an airplane), which is more cost-effective and eliminates errors introduced by variability between sensors, and the ability to make measurements in isolated and inaccessible areas where it is not feasible to make using in situ measurement techniques. Thus, remote sensing is the only soil sensing technique that is capable of providing regular and reliable large-scale measurements of soil moisture, including global measurements [21]. Currently, there exist three main remote sensing methods. The first two methods consider either the naturally emitted electromagnetic radiation by the target (passive remote sensing); or the scattered radiation by the target after it has been illuminated with a known source of radiation (active remote sensing). In the third method, changes in the gravitational potential field above the soil, which are related to changes in the density of the soil, and thus soil moisture, are measured. Currently, measurements of soil moisture using this method are only available at very large scales, 600 to 1000 km [22], only the passive and active methods can produce measurements at the small watershed scale. In the passive method, a remote sensing instrument called a radiometer is used to measure naturally emitted radiation from the soil. Like all matter, soil emits radiation, and this emission increases with temperature. The dielectric properties of the soil and its surface roughness determine how closely the soil surface resembles a perfect emitter (blackbody). The fraction of the total possible radiation (blackbody radiation) that is emitted is called the emissivity of the soil. Emissivity varies between 0 and 1. The value of the emissivity is essentially a linear function of the soil moisture content. At infrared wavelengths, soil emissivity is close to unity regardless of the soil moisture and so infrared radiometry is an effective method of soil surface temperature measurement. In the microwave region (wavelengths from meters to millimeters), soil emissivity is a strong function of soil moisture [23, 24]. Similarly, microwave radiometry, just like infrared radiometry, is an effective method for measuring the soil surface temperature. In the active method, remote sensors measure radiation scattered by the soil. Radars launch an electromagnetic wave toward the soil surface and then records the radiation scattered by the soil. The fraction of radiation scattered by a soil surface is a function of its moisture content. Radar at microwave frequencies is considered to be the most effective active remote sensing technique for the measurement of soil moisture [13].

In the sequel, a detailed description of microwave remote sensing is provided since the measurements employed in this thesis are obtained from microwave sensors.

2.2 Microwave Remote Sensing

An increasing amount of important environmental and resource information such as soil moisture content is being derived from remote sensors that operate in the microwave portion of the electromagnetic spectrum. The microwave region of the electromagnetic spectrum covers wavelengths within the approximate range of 1 mm to 1 m. Two unique features characterize microwave energy from a remote sensing standpoint:

1. Microwaves can penetrate the atmosphere under almost all conditions. Microwave energy can penetrate haze, light rain, snow, clouds, and smoke, depending on its wavelength.

2. Microwave reflections or emissions of microwaves from materials on the earth bear no direct relationship to their counterparts in the visible or thermal portions of the spectrum. For example, surfaces that appear rough in the visible portion of the spectrum may be smooth as seen by microwaves. In general, microwave responses afford us a significantly different view of the environment.

When used to measure soil moisture, microwave remote sensors provide a direct measurement of the near-surface soil moisture for a range of vegetation cover conditions within reasonable error bounds [25]. Sensors operating at very low microwave frequencies (less than 6 GHz) provide the best soil moisture information. Microwave sensors rely on the large difference between the dielectric constants of water (80) and other soil components (4) to provide the soil moisture information of a field [25]. The main relationship required to utilize microwave remote sensing is the relationship surface reflectivity r, the primary information provided by all kinds of microwave sensors, and soil moisture. The Fresnel equations are generally used to provide this relationship [26]. These equations measure r as a function of dielectric constant k and the view angle θ, depending on the polarization of the sensor (vertical-V or horizontal-H).

$$r^V = \left| \frac{kcos\theta - \sqrt{k - sin^2\theta}}{kcos\theta + \sqrt{k - sin^2\theta}} \right|^2 \tag{2.2}$$

$$r^H = \left| \frac{cos\theta - \sqrt{k - sin^2\theta}}{cos\theta + \sqrt{k - sin^2\theta}} \right|^2 \tag{2.3}$$

The dielectric constant (k) of the soil can be estimated using r, θ, and the polarization (H or V) of the sensor. Using the estimate of k and soil texture information, inversion models can be used to estimate the volumetric soil moisture [25], with measuring depths approximately equal to one-fourth the wavelength of the microwave.

Two primary microwave remote sensing approaches exist, passive and active.

2.2.1 Passive Microwave Sensors

In passive methods, very sensitive detectors called radiometers are used to measure naturally emitting thermal radiation from the soil surface at microwave frequencies (between 1 and 12 GHz) [27]. The intensity of the thermal emission is proportional to the product of the thermodynamic temperature of the soil T(K) and its emissivity e(-). Because the emitted radiation is proportional to the physical temperature of the object, the quantity measured by a passive microwave sensor is known as *brightness temperature*, $T_B(K)$ [27, 28]. The soil emissivity is related to soil reflectivity, r(-), by $e = 1 - r$. The reflectivity provides a link to the Fresnel equations and thus soil moisture for passive microwave sensors.

The presence of vegetation has a major impact on the measurements provided by passive sensors. Vegetation attenuates microwave signals from the soil and also adds a microwave emission of its own to the microwave measurement, thereby reducing the sensitivity of the retrieval algorithm to changes in the soil water content. This attenuation increases with increasing microwave frequency, and so it is important to operate passive sensors at low frequencies.

2.2.2 Active Microwave Sensors

In active methods, also known as radar, a microwave pulse is sent and received. The power of the received pulse is compared to that which was sent to yield a variable called the *backscaterring coefficient* (σ^o). This coefficient can be related to the surface reflectivity [26], which can then be used to determine the surface soil moisture of the field using the Fresnel equations. Active microwave techniques are capable of estimating surface soil moisture patterns at the field scale from airborne as well as spaceborne platforms. The two most common types of radars are synthetic aperture radars (SAR) and scatterometers. In the SAR, the microwave signal is further processed to obtain an image. Scatterometers are nonimaging radars. Estimating soil moisture content from radar backscatter is easier when there exists no vegetative cover on the field. In the presence of vegetation, the process becomes difficult since it requires the determination of the contribution of the soil itself from the vegetation.

2.2.3 Challenges Associated with Microwave Remote Sensing

Both passive and active techniques are sensitive to only the upper few centimeters of soil. This is because the microwave frequencies employed have emitting and penetration depths of approximately 5 cm. Thus, both methods provide near-surface measurements of soil moisture and fail to capture the total amount of moisture in the vadose zone. While the near-surface measurement is an important hydrological variable because of its effect on infiltration, runoff, and surface energy balance, the total amount in the vadose zone, specifically the root zone, is also an important factor due to its role in water management practices in agriculture. One feasible way to provide soil moisture information in the root zone from measurements provided by microwave remote sensors to integrate the near-surface measurements with numerical models [29]. The process of integrating soil moisture measurements, such as microwave remote sensing measurements, into numerical models is discussed in the next section.

2.3 Soil Moisture Estimation

As has already been mentioned, observed data from point soil moisture measurement methods are sparse and are thus limited in their spatial and temporal coverage of soil moisture. Though observations from non-invasive techniques such as remote sensing have the capability of capturing the spatial variability of soil moisture, one particularly important limitation of current remote sensing observations is that they only provide soil moisture information in a shallow surface layer. Consequently, observational data provided by the various soil moisture sensing techniques alone are not sufficient to provide accurate soil moisture information needed for feedback control.

Numerical models can be used to monitor soil moisture. These models provide spatially and temporally continuous predictions of soil moisture at specified space and time resolutions, and at various soil depths down to the water table. However, due to limited process knowledge and simplifications, numerical models are unable to predict soil moisture accurately. One such model is the Richards equation. The Richards equation is a partial differential equation (PDE) that describes the flow of water through unsaturated porous media under the action of gravity and capillarity.

By integrating numerical models with observational data, observational gaps can be filled and improved predictions of soil moisture can be obtained. The process of integrating observed data with numerical models is known as sequential data assimilation. The primary components of a sequential data assimilation system include observations, numerical modeling, and an analysis update. The observations used for large-scale soil moisture data assimilation systems include observations from point soil moisture sensing techniques or remote-sensing observations. The numerical modeling consists of two parts: (i) a predictive land surface model, such as the Richards equation, to dynamically propagate the state and (ii) a diagnostic observation model, such as the closed-form volumetric moisture content - capillary pressure head relationship provided by the van Genuchten model, to translate the state into the observed quantities. The analysis update combines the information from the observations and the model in an optimal fashion. Popular methods for the sequential assimilation of soil moisture observations include the extended Kalman filter (EKF) [30, 31], the ensemble Kalman filter (EnKF) [32, 33, 34, 35], the particle filter [36, 37] and the moving horizon estimator (MHE) [38, 39]. In [32], soil moisture estimates are obtained by assimilating L-band (1.4GHz) microwave radiobrightness observations into a land model using the EnKF. The land model used in this reference consists of mass and energy balance equations that describe the temporal and spatial distribution of soil moisture, soil temperature, and canopy temperature. In [33], a dual ensemble Kalman filter (DEnKF) was used to first estimate soil moisture using a standard KF and then to estimate the soil hydraulic parameters using an unscented Kalman filter by assimilating near-surface state observations into the one dimensional (1D) Richards equation. In [34], two EnKFs were used to estimate soil moisture and soil hydraulic parameters, separately, by assimilating soil moisture observations into a predictive hydrological model. In [35], simultaneous soil moisture and soil hydraulic parameters were based on the Common Land Model (CLM) by assimilating surface soil moisture observations. Also, the influence of brightness temperature assimilation on the estimation of soil moisture and soil hydraulic parameters. Reference [31] studied various assimilation techniques derived from the KF. In [38], simultaneous soil moisture and parameter estimation was based on assimilating tensiometer measurements into the 1D Richards equation using the MHE. Bo and Liu [39] proposed a decentralized framework for simultaneous soil moisture and parameter estimation based on the assimilation of capillary pressure head observations into the 3D Richards equations using the MHE.

2.4 Summary

The literature review has considered the current moisture sensing technologies. The two main types of sensing technologies have been outlined and specific methods under both types have been mentioned and discussed. The advantages and challenges associated with each type have also been outlined. The review has also considered microwave remote sensing in detail, discussed the principles underpinning microwave remote sensing, and further described the two types of microwave remote sensors. It mentioned the major challenge associated with microwave remote sensing and outlined how this challenge can be solved. Soil moisture estimation based on the assimilation of observed data into agro-hydrological models using the EKF, EnKF, particle filter, and the MHE was also reviewed.

Chapter 3

Soil Moisture Map Construction - Simulations

In this chapter, we provide simulation results to numerically demonstrate the good performance of the EKF and hence the effectiveness of the proposed information fusion system. We introduce the agro-hydrological system in Section 3.1 and then develop a mathematical model that is suitable for this work in Section 3.2. In Section 3.3, we provide a detailed description of the EKF algorithm. Section 3.4 begins with a description of the investigated field. The investigated field is then studied under four scenarios and the results of the EKF estimation in each scenario are provided. This chapter concludes with Section 3.5 where a summary of the simulation results is provided.

3.1 Development of the Agro-hydrological Framework

An agro-hydrological framework details the movement of water between crops, the soil and the atmosphere. Figure 3.1 provides a simple illustration of an agro-hydrological system.

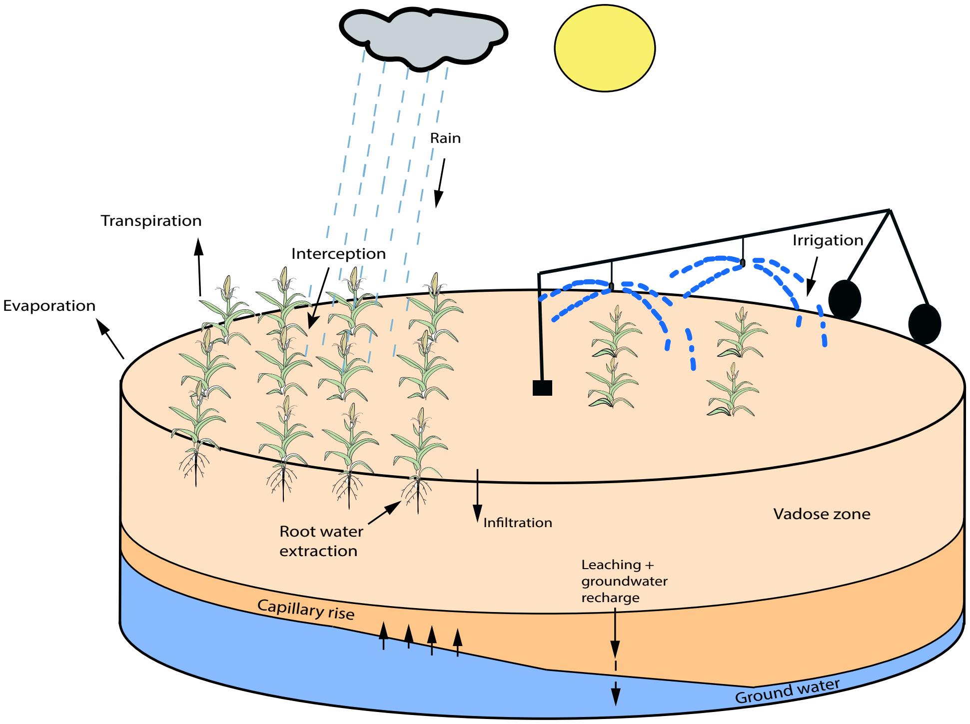

Figure 3.1: An agro-hydrological system.

For irrigation purposes, the region above the water table, known as the vadose zone, is usually considered. In an agro-hydrological system, water transport takes place primarily through irrigation, rain, evaporation, transpiration, infiltration, root water extraction, surface run-off and drainage. Depending on the prevailing water condition in the soil, rain or irrigation water may enter the soil at its surface. When the soil is unsaturated, water infiltrates into the soil and this continues until the soil becomes saturated. Under saturated conditions, infiltration stops and ponding begins to occur. After the ponding height has reached a certain level, run-off sets in. A portion of the rain or irrigated water is intercepted by the crop canopy. The roots of crops act as water sinks that extract water from the soil.

The transport of water in soil can be modeled using the Richards equation [40]. The

Richards equation can be expressed in a general form as:

$$\frac{\partial \theta}{\partial t} = C(h)\frac{\partial h}{\partial t} = \nabla.\ (K(h).\nabla\ (h+z)) - S(h,z) \tag{3.1}$$

In Equation (3.1), h (m) is the pressure head, θ ($\mathrm{m^3m^{-3}}$) is the volumetric water or moisture content, t (seconds) represents time, z (m) is the spatial coordinate, $K(h)$ ($\mathrm{ms^{-1}}$) is the unsaturated hydraulic water conductivity, $C(h)$ ($\mathrm{m^{-1}}$) is the capillary capacity, and $S(h,z)$ ($\mathrm{m^3m^{-3}s^{-1}}$) denotes the sink term.

3.1.1 Root Water Extraction Rate

Physically, the sink term, $S(h,z)$, represents the root water extraction rate which is defined as the volume of water taken up by the roots of crops per unit bulk volume of soil per unit time. To solve Equation (3.1), a function representing $S(h,z)$ is required. Simple empirical models have been developed to describe the root water extraction rate. In this work, the Feddes model is used to represent $S(h,z)$. In this model, the root water extraction rate is computed at the various depths of the soil using the potential transpiration rate, the rooting depth and the local prevailing soil water pressure head. Mathematically, the Feddes model [41] defines $S(h,z)$ as:

$$S(h,z) = \alpha(h)S_{\max}(h,z) \tag{3.2}$$

where $S_{\max}(h,z)$ ($\mathrm{m^3m^{-3}s^{-1}}$) is the maximum possible root extraction rate when soil water is not limiting and $\alpha(\cdot)$ is a dimensionless water stress reduction factor which is a function of the pressure head h (m). $\alpha(h)$ can be expressed as:

$$\alpha(h) = \begin{cases} 0 & h \leq h_1 \\ \frac{h-h_1}{h_2-h_1} & h_1 \leq h \leq h_2 \\ 1 & h_2 \leq h \leq h_3 \\ \frac{h_w-h}{h_w-h_3} & h_3 \leq h \leq h_w \end{cases} \tag{3.3}$$

where h_1 (m) is the pressure head below which roots start to extract water from the soil, h_2 (m) and h_3 (m) are the pressure heads between which optimal water uptake exists, and h_w (m) is the permanent wilting point pressure head [9]. In this work, optimum water uptake is assumed.

The Feddes model consists of two alternative models for $S_{\max}$: independent of depth and depth dependent. The independent of depth model is used in this work and it is expressed in [42]:

$$S_{\max} = \frac{\mathrm{TP}_p}{L} \tag{3.4}$$

where TP_p (ms^{-1}) is the potential transpiration rate and L (m) is the rooting depth. The potential transpiration rate, TP_p (ms^{-1}) is computed by:

$$\mathrm{TP}_p = \mathrm{ETP}_p - \mathrm{EV} \tag{3.5}$$

where ETP_p (ms^{-1}) is potential evapotranspiration (sum of potential transpiration and potential evaporation) and EV (ms^{-1}) is the potential evaporation rate computed as in [43] by:

$$\mathrm{EV} = \mathrm{ETP}_p \times \exp(-0.623\mathrm{LAI}) \tag{3.6}$$

where LAI ($\mathrm{m}^2\mathrm{m}^{-2}$) is the Leaf Area Index function.

Potential evapotranspiration, ETP_p (ms^{-1}) can be computed by:

$$\mathrm{ETP}_p = K_c \mathrm{PET} \tag{3.7}$$

where PET (ms^{-1}) is the reference evapotranspiration which is computed from meteorological data using the Penman-Monteith equation and K_c $(-)$ is the crop coefficient.

3.2 Cylindrical Coordinates Version of the Richards Equation

In this work, to describe the circular movement of the center pivot, we model a field equipped with a center pivot irrigation system with the cylindrical coordinates version of the Richards equation. Specifically, Equation (3.1) is expressed in terms of r, θ, and z where r (m) represents the radial direction which denotes the radius of the field, θ represents the azimuthal direction which denotes the angle of rotation of the center pivot, and z (m) is the axial direction which represents the depth of soil under consideration.

To express the Richards equation in cylindrical coordinates, the gradient (∇) and divergence ($\nabla.$) operators present in Equation (3.1) are expressed in their cylindrical forms. In cylindrical coordinates, the gradient operator is defined as:

$$\nabla \coloneqq \frac{\partial}{\partial r}\hat{r} \; + \; \frac{1}{r}\frac{\partial}{\partial \theta}\hat{\theta} \; + \; \frac{\partial}{\partial z}\hat{z} \tag{3.8}$$

where $\hat{r}$, $\hat{\theta}$, $\hat{z}$ are the unit vectors in the radial, azimuthal and axial directions respectively. The divergence of a continuously differentiable vector field F in the cylindrical coordinate system is defined as:

$$\nabla.F \coloneqq \frac{1}{r}\frac{\partial}{\partial r}(rF_r) + \frac{1}{r}\frac{\partial F_\theta}{\partial \theta} + \frac{\partial F_z}{\partial z} \tag{3.9}$$

where F_r, F_θ, and F_z are the components of the vector field F in the radial, azimuthal and axial directions respectively. Applying the operators to the corresponding terms in Equation (3.1) yields the cylindrical coordinates version of the Richards equation which is expressed as:

$$C(h)\frac{\partial h}{\partial t} = \frac{1}{r}\frac{\partial}{\partial r}\left[rK(h)\frac{\partial h}{\partial r}\right] + \frac{1}{r}\frac{\partial}{\partial \theta}\left[\frac{K(h)}{r}\frac{\partial h}{\partial \theta}\right] + \frac{\partial}{\partial z}\left[K(h)\left(\frac{\partial h}{\partial z} + 1\right)\right] - S(h, z) \tag{3.10}$$

The cylindrical coordinates version of the Richards equation is a nonlinear elliptic-parabolic partial differential equation (PDE) with respect to the spatial ($r,\ \theta,\ z$) and temporal (t) variables respectively.

The soil hydraulic functions $\theta(h)$, $K(h)$ and $C(h)$ in Equations (3.1) and (3.10) are described by the Mualem-van Genucthen model [44]:

$$\theta(h) = \theta_r + (\theta_s - \theta_r)\left[\frac{1}{1 + (-\alpha h)^n}\right]^{1-\frac{1}{n}} \tag{3.11}$$

$$K(h) = K_s\left[(1 + (-\alpha h)^n)^{-\left(\frac{n-1}{n}\right)}\right]^{\frac{1}{2}} \times \left[1 - \left[1 - \left[(1 + (-\alpha h)^n)^{-\left(\frac{n-1}{n}\right)}\right]^{\frac{n}{n-1}}\right]^{\frac{n-1}{n}}\right]^2 \tag{3.12}$$

$$C(h) = (\theta_s - \theta_r)\ \alpha n\ \left[1 - \frac{1}{n}\right]\ (-\alpha h)^{n-1}[1 + (-\alpha h)^n]^{-\left(2-\frac{1}{n}\right)} \tag{3.13}$$

where θ_s ($\mathrm{m^3m^{-3}}$), θ_r ($\mathrm{m^3m^{-3}}$), K_s ($\mathrm{ms^{-1}}$) are the saturated volumetric moisture content, residual moisture content and saturated hydraulic conductivity respectively and n, α are curve-fitting soil hydraulic properties.

Equation (3.10) is solved using these explicit expressions between the dependent variables θ, K, C and h.

3.2.1 Finite Difference Model Development

Obtaining an analytical solution to Equation (3.10) is difficult due to its nonlinearity, thus we employ a numerical technique to solve the PDE. In this work, the method of lines (MOL) approach is used. In the MOL approach, the PDE is discretized with respect to its spatial variables ($r,\ \theta,\ z$). This converts the PDE to a set of ordinary differential equations (ODEs), which can then be solved using well established numerical methods for ODEs.

The central difference scheme is used to approximate the derivatives (discretize) with respect to the r, θ, and z variables. The detailed approximation procedure in the r, θ, and z directions is described next.

3.2.1.1 Discretization in the Radial Direction

$$\frac{1}{r}\frac{\partial}{\partial r}\left[rK(h)\frac{\partial h}{\partial r}\right]\bigg|_{e_r,e_\theta,k} \approx \frac{1}{r_{e_r,e_\theta,k}\Delta r_i}\left[r_{e_r+\frac{1}{2},e_\theta,k}K_{e_r+\frac{1}{2},e_\theta,k}(h)\left(\frac{h_{e_r+1,e_\theta,k}-h_{e_r,e_\theta,k}}{\Delta r_E}\right)- r_{e_r-\frac{1}{2},e_\theta,k}K_{e_r-\frac{1}{2},e_\theta,k}(h)\left(\frac{h_{e_r,e_\theta,k}-h_{e_r-1,e_\theta,k}}{\Delta r_W}\right)\right] \quad (3.14)$$

where $e_r \in [0, N_r+1]$, $e_\theta \in [0, N_\theta+1]$ and $k \in [0, N_z+1]$ represent the position indices in the radial, azimuthal and axial directions respectively. $e_r,\ e_\theta,\ k\ \subset\ \mathbb{Z}^+$. N_a is the total number of nodes (states) in the a direction. $\Delta r_E = r_{e_r+1,e_\theta,k} - r_{e_r,e_\theta,k}$, $\Delta r_W = r_{e_r,e_\theta,k} - r_{e_r-1,e_\theta,k}$ and $\Delta r_i = \frac{1}{2}(\Delta r_E + \Delta r_W)$. $r_{e_r\pm\frac{1}{2},e_\theta,k} = \frac{1}{2}(r_{e_r,e_\theta,k} + r_{e_r\pm1,e_\theta,k})$ and $K_{e_r\pm\frac{1}{2},e_\theta,k}(h) \approx \frac{1}{2}(K(h_{e_r,e_\theta,k}) + K(h_{e_r\pm1,e_\theta,k}))$. All the nodes in the radial direction are in the center of the e_r^{th} compartment, as shown in Figure 3.2. The subscripts $E,\ C,$ and W correspond to the coordinates $(e_r+1,\ e_\theta,\ k)$, $(e_r,\ e_\theta,\ k)$ and $(e_r-1,\ e_\theta,\ k)$ respectively.

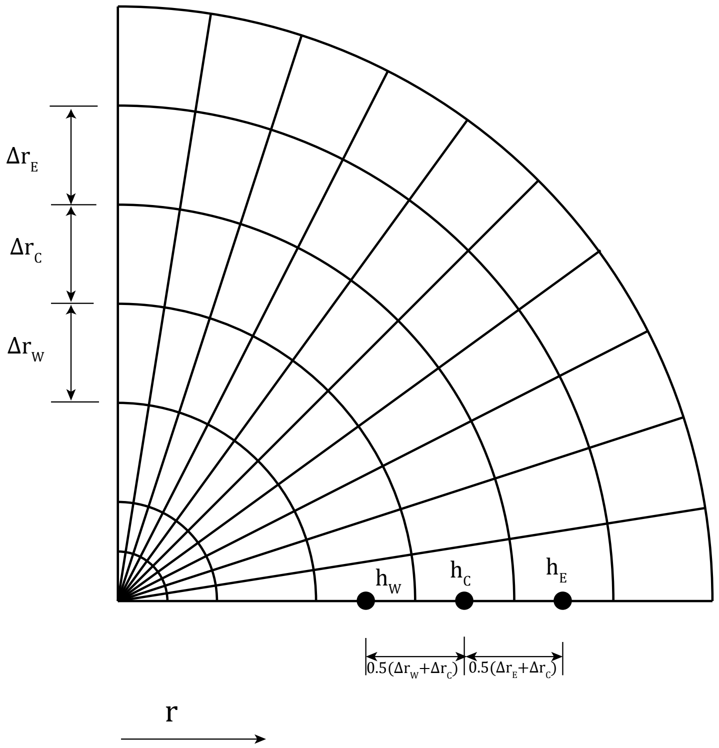

Figure 3.2: A schematic diagram of the radial discretization.

3.2.1.2 Discretization in the Azimuthal Direction

$$\frac{1}{r}\frac{\partial}{\partial\theta}\left[\frac{K(h)}{r}\frac{\partial h}{\partial\theta}\right]\Bigg|_{e_r,e_\theta,k} \approx \frac{1}{r_{e_r,e_\theta,k}\Delta\theta_j}\left[\frac{K_{e_r,e_\theta+\frac{1}{2},k}(h)}{r_{e_r,e_\theta+\frac{1}{2},k}}\left(\frac{h_{e_r,e_\theta+1,k}-h_{e_r,e_\theta,k}}{\Delta\theta_T}\right)- \frac{K_{e_r,e_\theta-\frac{1}{2},k}(h)}{r_{e_r,e_\theta-\frac{1}{2},k}}\left(\frac{h_{e_r,e_\theta,k}-h_{e_r,e_\theta-1,k}}{\Delta\theta_D}\right)\right] \tag{3.15}$$

where $\Delta\theta_T = \theta_{e_r,e_\theta+1,k} - \theta_{e_r,e_\theta,k}$, $\Delta\theta_D = \theta_{e_r,e_\theta,k} - \theta_{e_r,e_\theta-1,k}$ and $\Delta\theta_j = \frac{1}{2}(\Delta\theta_T + \Delta\theta_D)$. $r_{e_r,e_\theta\pm\frac{1}{2},k} = \frac{1}{2}(r_{e_r,e_\theta,k} + r_{e_r,e_\theta\pm1,k}) = r_{e_r,e_\theta,k}$ and $K_{e_r,e_\theta\pm\frac{1}{2},k}(h) \approx \frac{1}{2}(K(h_{e_r,e_\theta,k}) + K(h_{e_r,e_\theta\pm1,k}))$. All the nodes in the azimuthal direction are in the center of the e_θ^{th} compartment, as shown in Figure 3.3. The subscripts T, C, and D correspond to the coordinates $(e_r, e_\theta + 1, k)$, (e_r, e_θ, k) and $(e_r, e_\theta - 1, k)$ respectively.

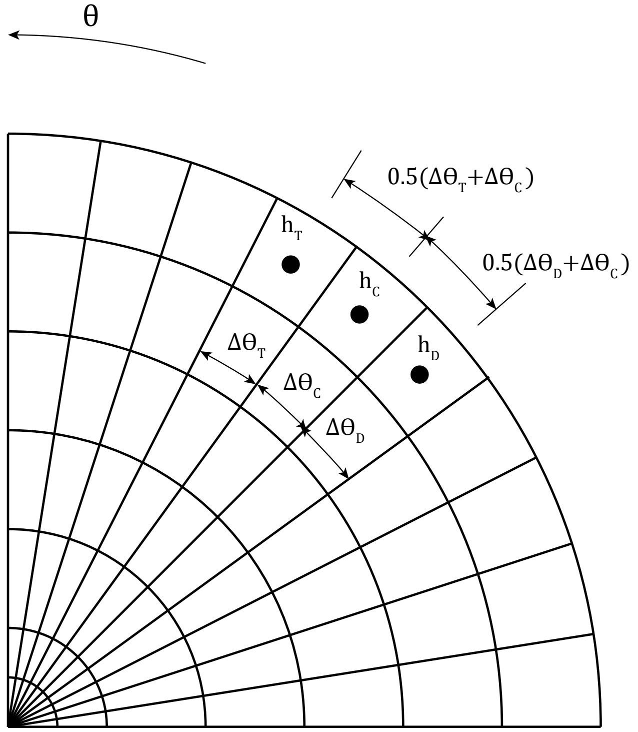

Figure 3.3: A schematic diagram of the azimuthal discretization.

3.2.1.3 Discretization in the Axial Direction

$$\frac{\partial}{\partial z}\left[K(h)\left(\frac{\partial h}{\partial z}+1\right)\right]\Bigg|_{e_r,e_\theta,k} \approx \frac{1}{\Delta z_k}\left[K_{e_r,e_\theta,k+\frac{1}{2}}(h)\left(\frac{h_{e_r,e_\theta,k+1}-h_{e_r,e_\theta,k}}{\Delta z_N}+1\right)\right.$$
$$\left. - K_{e_r,e_\theta,k-\frac{1}{2}}(h)\left(\frac{h_{e_r,e_\theta,k}-h_{e_r,e_\theta,k-1}}{\Delta z_S}+1\right)\right] \quad (3.16)$$

where $\Delta z_N = z_{e_r,e_\theta,k+1} - z_{e_r,e_\theta,k}$, $\Delta z_S = z_{e_r,e_\theta,k} - z_{e_r,e_\theta,k-1}$, $\Delta z_k = \frac{1}{2}(\Delta z_N + \Delta z_S)$ and $K_{e_r,e_\theta,k\pm\frac{1}{2}}(h) \approx \frac{1}{2}(K(h_{e_r,e_\theta,k}) + K(h_{e_r,e_\theta,k\pm1}))$. All the nodes in the axial direction are in the center of the k^{th} compartment, as shown in Figure 3.4. In Figure 3.4, the subscripts N, C, and S correspond to the coordinates $(e_r,\ e_\theta,\ k+1)$, $(e_r,\ e_\theta,\ k)$ and $(e_r,\ e_\theta,\ k-1)$ respectively.

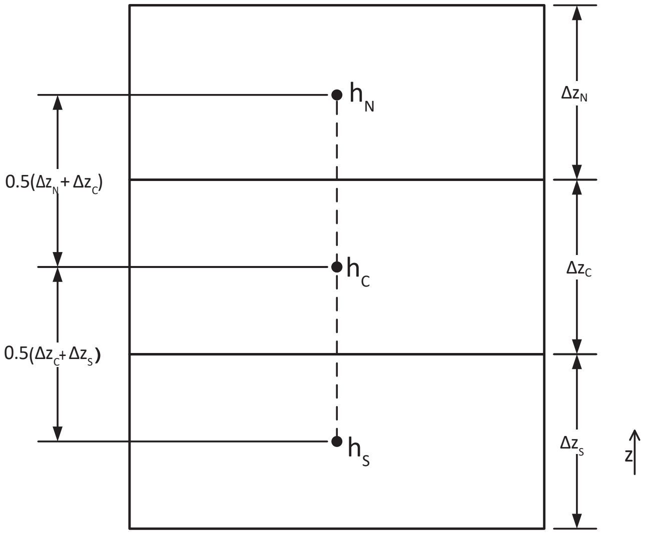

Figure 3.4: A schematic diagram of the axial discretization.

The resulting ODE, in terms of the temporal variable, is obtained by substituting Equations (3.14), (3.15) and (3.16) into Equation (3.10) as follows

$$\frac{dh}{dt} = \frac{1}{C_{e_r,e_\theta,k}(h)} \Bigg[\Bigg(\frac{1}{r_{e_r,e_\theta,k}\Delta r_i} \Bigg[r_{e_r+\frac{1}{2},e_\theta,k} K_{e_r+\frac{1}{2},e_\theta,k}(h) \Bigg(\frac{h_{e_r+1,e_\theta,k} - h_{e_r,e_\theta,k}}{\Delta r_E} \Bigg) - r_{e_r-\frac{1}{2},e_\theta,k} K_{e_r-\frac{1}{2},e_\theta,k}(h) \Bigg(\frac{h_{e_r,e_\theta,k} - h_{e_r-1,e_\theta,k}}{\Delta r_W} \Bigg) \Bigg] \Bigg) + \Bigg(\frac{1}{r_{e_r,e_\theta,k}\Delta\theta_j} \Bigg[\frac{K_{e_r,e_\theta+\frac{1}{2},k}(h)}{r_{e_r,e_\theta+\frac{1}{2},k}} \Bigg(\frac{h_{e_r,e_\theta+1,k} - h_{e_r,e_\theta,k}}{\Delta\theta_T} \Bigg) - \frac{K_{e_r,e_\theta-\frac{1}{2},k}(h)}{r_{e_r,e_\theta-\frac{1}{2},k}} \Bigg(\frac{h_{e_r,e_\theta,k} - h_{e_r,e_\theta-1,k}}{\Delta\theta_D} \Bigg) \Bigg] \Bigg) + \Bigg(\frac{1}{\Delta z_k} \Bigg[K_{e_r,e_\theta,k+\frac{1}{2}}(h) \Bigg(\frac{h_{e_r,e_\theta,k+1} - h_{e_r,e_\theta,k}}{\Delta z_N} + 1 \Bigg) - K_{e_r,e_\theta,k-\frac{1}{2}}(h) \Bigg(\frac{h_{e_r,e_\theta,k} - h_{e_r,e_\theta,k-1}}{\Delta z_S} + 1 \Bigg) \Bigg] \Bigg) - S(h,z) \Bigg] \quad (3.17)$$

3.2.2 Treatment of the Axis

In this work, L'Hopital's rule is applied to the first and second terms at the right hand side of Equation (3.10) in order to deal with the singularity that occurs at the axis ($r = 0$). The resulting equations are expressed as follows:

$$\lim_{r \to 0} \frac{1}{r} \frac{\partial}{\partial r} \left[r K(h) \frac{\partial h}{\partial r} \right] = \lim_{r \to 0} \frac{\frac{\partial}{\partial r} \left(\frac{\partial}{\partial r} \left[r K(h) \frac{\partial h}{\partial r} \right] \right)}{\frac{\partial}{\partial r} (r)} = 2 \frac{\partial}{\partial r} \left(K(h) \frac{\partial h}{\partial r} \right) \tag{3.18}$$

$$\lim_{r \to 0} \frac{1}{r} \frac{\partial}{\partial \theta} \left[\frac{K(h)}{r} \frac{\partial h}{\partial \theta} \right] = \lim_{r \to 0} \frac{\frac{\partial}{\partial r} \left(\frac{\partial}{\partial \theta} \left[K(h) \frac{\partial h}{\partial \theta} \right] \right)}{\frac{\partial}{\partial r} (r^2)} = \frac{1}{2} \frac{\partial}{\partial r} \left(\frac{\partial}{\partial r} \left(\frac{\partial}{\partial \theta} \left[K(h) \frac{\partial h}{\partial \theta} \right] \right) \right) \tag{3.19}$$

Substitution of Equations (3.18) and (3.19) into Equation (3.10) yields the cylindrical coordinates version of the Richards equation at $r = 0$:

$$C(h) \frac{\partial h}{\partial t} = 2 \frac{\partial}{\partial r} \left(K(h) \frac{\partial h}{\partial r} \right) + \frac{1}{2} \frac{\partial}{\partial r} \left(\frac{\partial}{\partial r} \left(\frac{\partial}{\partial \theta} \left[K(h) \frac{\partial h}{\partial \theta} \right] \right) \right) + \frac{\partial}{\partial z} \left[K(h) \left(\frac{\partial h}{\partial z} + 1 \right) \right] - S(h, z) \tag{3.20}$$

3.2.3 Boundary Conditions

Equation (3.17) is solved numerically for the following boundary equations which are applicable to fields equipped with a center pivot irrigation system:

$$\frac{\partial h(r, \theta, z, t)}{\partial r} = 0 \qquad \text{at} \quad (r = 0,\ \theta,\ z) \tag{3.21}$$

$$\frac{\partial h(r, \theta, z, t)}{\partial r} = 0 \qquad \text{at} \quad (r = H_r,\ \theta,\ z) \tag{3.22}$$

$$h(r = 0,\ \theta,\ z,\ t) = h(r = 0,\ \theta = 0,\ z,\ t) \tag{3.23}$$

$$h(r,\ \theta = 0,\ z,\ t) = h(r,\ \theta = 2\pi,\ z,\ t) \tag{3.24}$$

$$\frac{\partial(h\,(r,\theta,z,t) + z)}{\partial z} = 1 \qquad \text{at} \quad (r,\ \theta,\ z = 0) \tag{3.25}$$

$$\frac{\partial(h\,(r,\theta,z,t))}{\partial z} = -1 - \frac{u_{\text{irr}}}{K(h)} \qquad \text{at} \qquad (r,\ \theta,\ z = H_z) \tag{3.26}$$

The zero gradient boundary condition is imposed at $r = 0$ and $r = H_r$ (H_r is the total radius of the field) as shown in Equations (3.21) and (3.22). Equation (3.23) describes the coordinates of the dependent variable, the pressure head (h), that coincide at $r = 0$. After one revolution, the starting point coincides with the ending point and this is represented by Equation (3.24). Equation (3.25) represents the free drainage boundary condition that is applied at the bottom of the field ($z = 0$). The Nuemann boundary condition, shown by Equation (3.26), is applied at the top of the field ($z = H_z,\ H_z$ is the depth of the field). u_{irr} (m/s) in Equation (3.26) represents the irrigation rate which is considered as the input in this work.

3.2.4 State-space Representation of the Field Model

Before introducing the state estimation method, we obtain a compact form of the field model by combining $(N_r\ +1) \times (N_\theta\ +1) \times (N_z\ +1)$ of Equation (3.17) for all the spatial nodes and boundary conditions, Equations (3.21) - (3.26). It is shown below.

$$\dot{x} = f(x(t), u(t)) + \omega(t) \tag{3.27}$$

where $x(t) \in \mathbb{R}^{N_x}$ represents the state vector containing $N_x = (N_r\ +1) \times (N_\theta\ +1) \times (N_z\ +1)$ pressure head values for the corresponding spatial nodes, defined at time instant t. $u(t) \in \mathbb{R}^{N_u}$ and $\omega(t) \in \mathbb{R}^{N_x}$ represent the input and the model disturbances respectively. The general output function, taking into account measurement noise is shown below.

$$y(t) = h(x(t), t) + v(t) \tag{3.28}$$

where $y(t) \in \mathbb{R}^{N_y}$, $v(t) \in \mathbb{R}^{N_y}$ respectively denote the measurement vector and the measurement noise. Equation (3.28) is the general form of Equation (3.11) since the microwave sensors provide volumetric water content θ measurements. In this work, the measurement locations change at each sampling time, due to the movement of the center pivot and this results in a time varying output function $h(\cdot)$.

Equations (3.25) and (3.26) form the state-space representation of the agro-hydrological framework.

3.3 State Estimator Design

In this work, the discrete-time Extended Kalman filter (EKF) is chosen as the state estimator. The EKF is a well-known method used for the estimation of nonlinear systems based on a successive linearization of the nonlinear system about the previous estimate of the states. The EKF is made up of two main steps, the prediction, and the update steps. The prediction step updates the state x and its covariance matrix P using the model of the system. The update step is carried out when measurements are available. In the presence of measurements, x and P are updated again by first computing the gain matrix K. The detailed steps are shown below.

Initialization

(1) The continuous-time system, Equations (3.27) and (3.28), is discretized to obtain its discrete-time equivalent. The discrete-time version can be expressed as:

$$x_{k+1} = F(x(k), u(k)) + \omega(k)$$
$$y_k = H(x(k), k) + v(k)$$

(2) The filter is initialised as follows:

$$E[x_0] = \hat{x}_0$$

$$E[(x_0 - \hat{x}_0)(x_0 - \hat{x}_0)^T] = P(0|0)$$

Prediction Step

(1) Given the previous state estimate $\hat{x}_{k|k}$, the previous observation sequence Y_k and the new input u_k to the system, the new state of the system at time t_{k+1}:

$$\begin{aligned}\hat{x}_{k+1|k} &= E[x_{k+1}|Y_k, u_k] \\ &= F(\hat{x}_{k|k}, u_k)\end{aligned}$$

where $Y_k \coloneqq \{y_0, y_1, \ldots.., y_k\}$.

The state covariance matrix can be calculated as:

$$\begin{aligned}P(k+1|k) &= E[(x_{k+1} - \hat{x}_{k+1|k})(x_{k+1} - \hat{x}_{k+1|k})^T|Y_k, u_k] \\ &= A_k P(k|k) A_k^T + Q\end{aligned}$$

where $A_k = \frac{\partial F}{\partial x}|_{\hat{x}_{k|k}, u_k}$ and Q is the covariance matrix of the process disturbance ω.

Filtering Step

In this step, we use the observation y_{k+1} at time t_{k+1} to update the state and its covariance.

(1) Kalman gain matrix, K_{k+1} calculation

$$K_{k+1} = P(k+1|k) H_{k+1}^T [H_{k+1}[P(k+1|k) H_{k+1}^T + R]^{-1}$$

where $H_{k+1} = \frac{\partial H}{\partial x}|_{\hat{x}_{k+1|k}}$ and R is the covariance matrix of the measurement noise v.

(2) State update

$$\begin{aligned}\hat{x}_{k+1|k+1} &= E[x_{k+1}|Y_{k+1}, u_k] \\ &= \hat{x}_{k+1|k} + K_{k+1}[y_{k+1} - H(\hat{x}_{k+1|k})]\end{aligned}$$

where $Y_{k+1} \coloneqq \{Y_k, y_{k+1}\}$

(3) State covariance update

$$\begin{aligned}P(k+1|k+1) &= E[(x_{k+1} - \hat{x}_{k+1|k+1})(x_{k+1} - \hat{x}_{k+1|k+1})^T|Y_{k+1}] \\ &= [I - K_{k+1}H_{k+1}]P\,(k+1|k)\end{aligned}$$

3.4 Simulation Results and Discussion

In this section, we provide simulation results to numerically demonstrate the performance of the EKF and hence the effectiveness of the proposed information fusion system under 4 different scenarios namely Scenarios 1, 2, 3, and 4.

Two simulation cases, namely the normal and the parameter uncertain cases are considered in each scenario. In the normal case, accurate soil hydraulic parameters are used in the EKF while in the parameter uncertain case, a 5% uncertainty is introduced into the soil hydraulic parameters.

3.4.1 System Description

A field of radius 50 m and depth of 0.30 m is investigated in this work. The field is divided into 6, 40 and 16 compartments in the radial, azimuthal and axial directions respectively. Consequently, the cylindrical coordinates version of the Richards equation is spatially discretized into a total of 3,840 states, with each state centered at its corresponding compartment. A schematic diagram of the investigated field is shown in Figure 3.5.

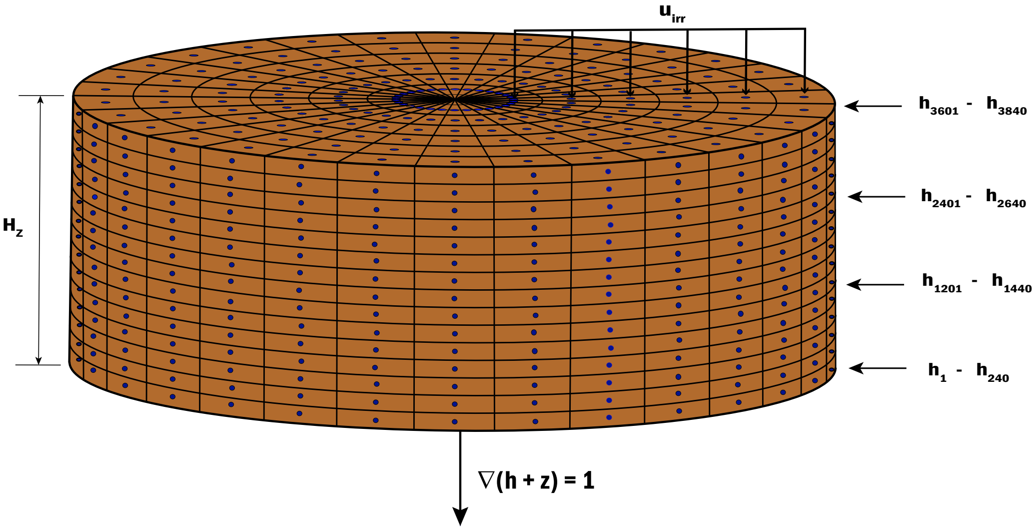

Figure 3.5: A schematic diagram of the investigated field.

In each scenario, the center pivot moves at a speed of 0.022 m/s. In Scenarios 1, 2, and 3, an irrigation amount of 7 mm/day is supplied to the surface of the field between 0:00 AM to 4:00 AM daily. In Scenario 4, an irrigation amount of 3.6 mm/day is supplied to the field's surface between 0:00 AM to 12:00 PM daily.

The soil moisture measurements that are fed into the EKF at each sampling time are obtained from the adjacent sector (represented with the red dots in Figure 3.6), in the anti-clockwise direction, of the presently irrigated sector (represented with the blue dots in Figure 3.6). Since the presently irrigated sector changes after a specific time, the measured nodes also change. This arrangement describes the operation of microwave sensors mounted on center pivots. In Scenarios 1, 2, and 3, 11 soil moisture measurements are used in the update step of the EKF at each sampling time. For Scenario 4, 16 soil moisture measurements are used in the update step at each sampling time.

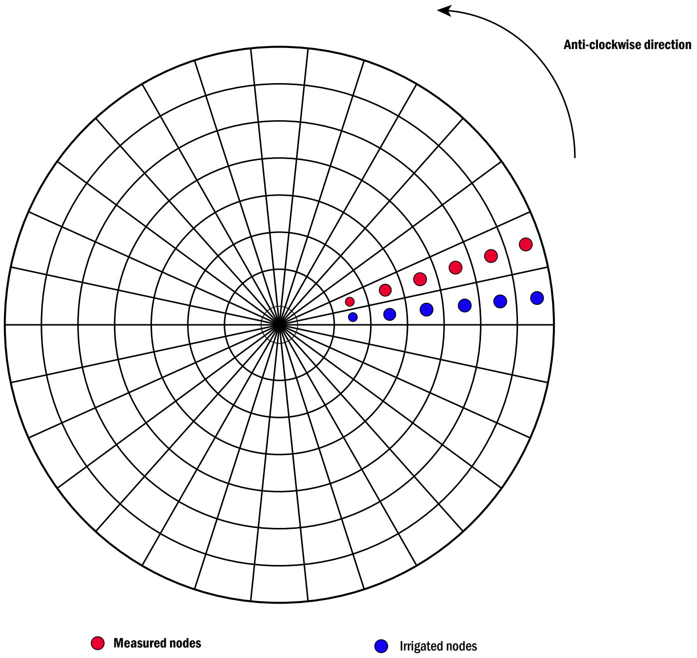

Figure 3.6: A schematic representation of center pivots equipped with microwave sensors.

This work considers the presence of a healthy barley crop in its development stage on the investigated field. Thus, crop coefficient values between 0.75 and 0.96 are used in this work. In Scenarios 1, 2 and 3, daily reference evapotranspiration values of 1.2 mm/day, 1.70 mm/day, 0.6 mm/day, 0.5 mm/day and 2.10 mm/day are used. Scenario 4 uses daily reference evapotranspiration values of 1.2 mm/day, 1.70 mm/day, 0.6 mm/day, 0.5 mm/day, 2.10 mm/day, 1.24 mm/day, 0.7 mm/day, 3.14 mm/day and 2.0 mm/day.

Process noise and measurement noise are considered in the simulations and they have zero mean and standard deviations of 1×10^{-5} m and 1×10^{-4} $\mathrm{m^3 m^{-3}}$ respectively.

The error sum of square in terms of the state, (SSE$_x$), is used to evaluate the performance of the EKF.

$$SSE_x = \Sigma_{i=1}^{N_x}(x_i - \hat{x}_i)^2 \tag{3.29}$$

Trajectories of the actual process states and the state estimates calculated by EKF are also compared for some selected nodes. The selected nodes are located at depths of 0.00 m (surface of the field), 0.06 m, 0.12 m, 0.18 m, 0.24 m, and 0.30 m (bottom of the investigated field). The actual process states and the estimates of the states are converted into volumetric moisture content using Equation (3.11). The absolute error (e_k) between the actual volumetric moisture content and the estimated volumetric moisture content is also computed.

$$e_k = |y_k - \hat{y}_k| \tag{3.30}$$

Moisture content maps are constructed to represent the calculated volumetric moisture content and absolute error. For the sake of brevity, a moisture content map constructed with the actual volumetric moisture content, the estimated volumetric soil moisture content, and the absolute error is referred to as the actual moisture content map, the estimated moisture content map, and the absolute error map respectively. The absolute error map will serve as the basis for comparing the estimated moisture content map to the actual moisture content map.

The code is written in Python and the simulations are carried out on a computer with Intel i7 CPU, 16.00 GB RAM.

3.4.2 Scenario 1

In this scenario, a single soil type and uniform initial conditions are considered in the investigated field. Specifically, it is assumed that the investigated field contains loamy soil. Table 3.1 shows the initial condition and the hydraulic properties of loamy soil. The last row of Table 3.1 shows the soil parameters that are used in the EKF during the parameter uncertain case.

Table 3.1: The initial condition and parameters of loamy soil.

	x_0 (m)	K_s (m/s)	θ_s (m^3/m^3)	θ_r (m^3/m^3)	α (1/m)	n (-)
Normal case	-0.8	2.889×10^{-6}	0.430	0.0780	3.60	1.56
Parameter uncertain case	-0.8	3.033×10^{-6}	0.452	0.0920	3.80	1.64

The EKF is initialized with $\hat{x}_0 = 1.2 \times x_0$ and the simulation is performed for 5 days.

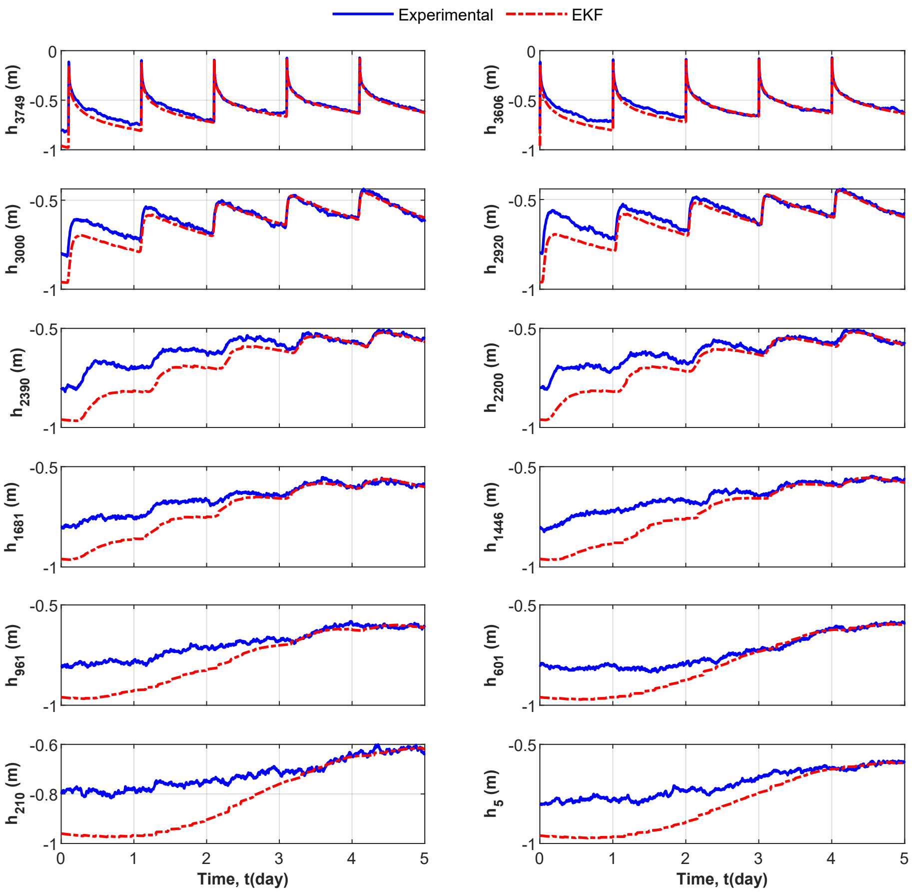

Figure 3.7: Selected trajectories of the actual process states and the state estimates in the normal case of Scenario 1.

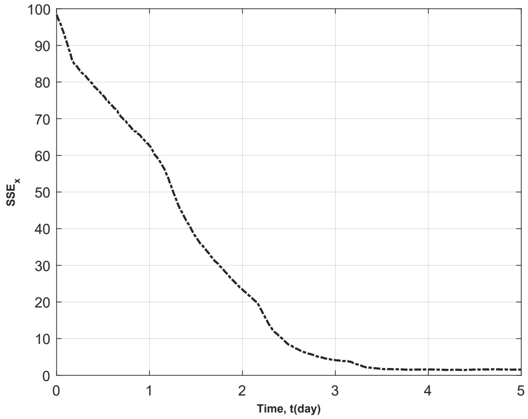

Figure 3.8: Trajectory of the SSE$_x$ in the normal case of Scenario 1.

From Figure 3.7, it can be seen that the EKF (red dash-dot) can track the actual process states (blue solid line) very well in the normal case. It can also be seen that the estimates of states located on the surface of the field ($h_{3749},\ h_{3606}$) converge to the actual process states faster than the other estimates. This is because the surface states serve as sensor nodes. It is also evident that for states below the surface, the closer the state is to the surface, the faster its estimates converge. It is observed that the estimates of h_5 and h_{210}, which are the farthest states from the surface in Figure 3.7, have the lowest convergence rates. From Figure 3.8, it can be seen that there is a monotonic decrease in the SSE_x from the beginning of the simulation up to about 3.5 days, where it attains a value of 1.80. After 3.5 days, it is observed that the value of the SSE_x stays fairly constant till the end of the simulation. From this figure, it can be inferred that all the estimates of the states in the investigated field converge after 3.5 days.

Next, the moisture content maps constructed at selected times during the simulation period, for the surface and the bottom of the field, are analysed.

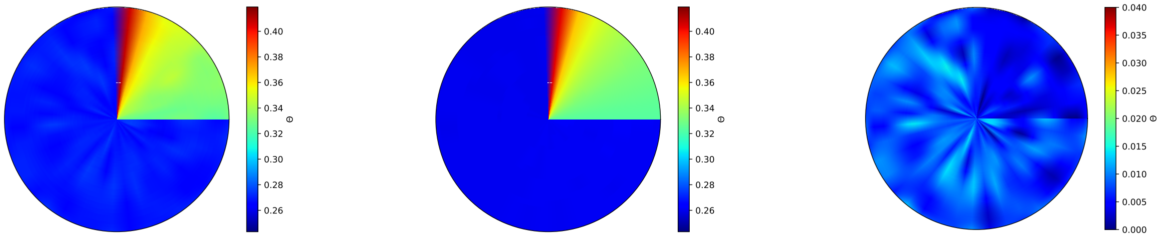

(a) Actual map. (b) Estimated map. (c) Absolute error map.

Figure 3.9: Surface moisture content maps at 01:00 HRS on Day 2 for the normal case of Scenario 1.

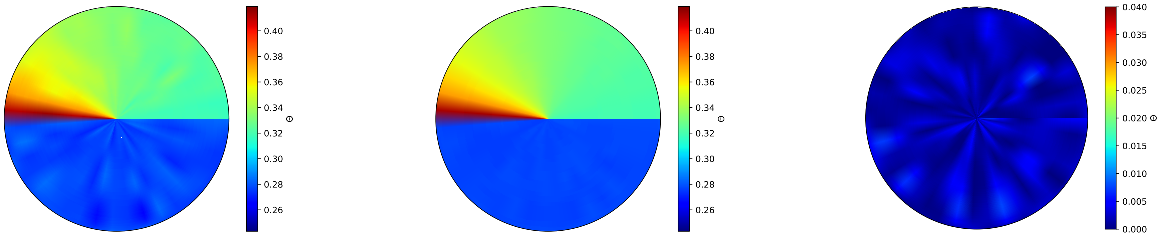

(a) Actual map. (b) Estimated map. (c) Absolute error map.

Figure 3.10: Surface moisture content maps at 02:00 HRS on Day 4 for the normal case of Scenario 1.

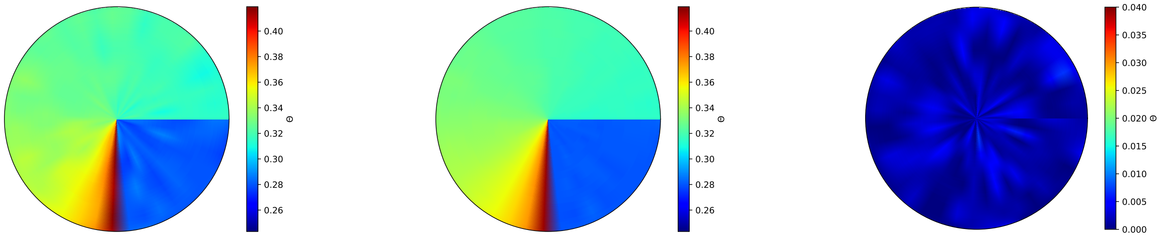

(a) Actual map.

(b) Estimated map.

(c) Absolute error map.

Figure 3.11: Surface moisture content maps at 03:00 HRS on Day 5 for the normal case of Scenario 1.

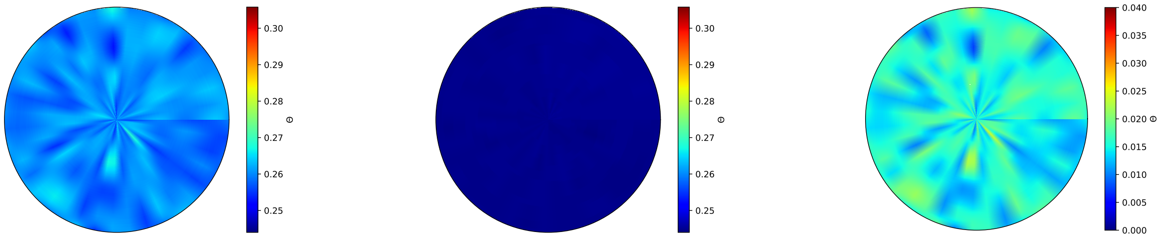

(a) Actual map.

(b) Estimated map.

(c) Absolute error map.

Figure 3.12: Maps at a depth of 0.3 m on Day 1 at 01:00 HRS for the normal case of Scenario 1.

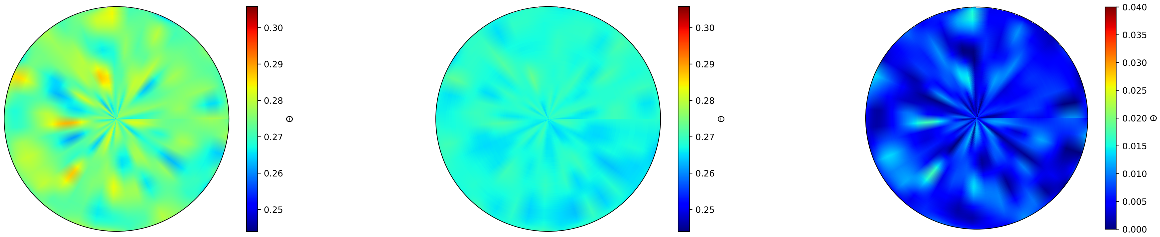

(a) Actual map.

(b) Estimated map.

(c) Absolute error map.

Figure 3.13: Maps at a depth of 0.3 m on Day 4 at 02:00 HRS for the normal case of Scenario 1.

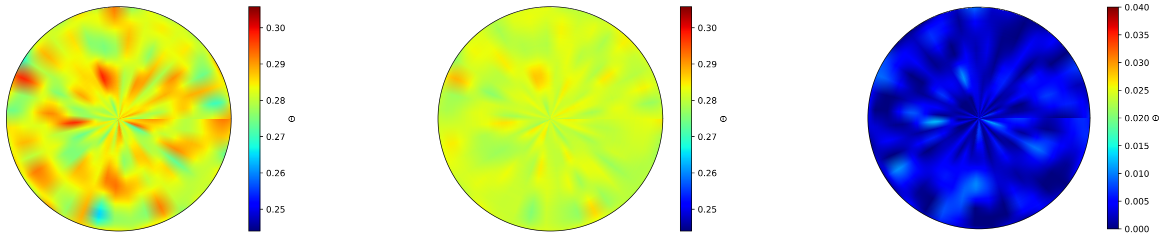

(a) Actual map. (b) Estimated map. (c) Absolute error map.

Figure 3.14: Maps at a depth of 0.3 m on Day 5 at 03:00 HRS for the normal case of Scenario 1.

From the moisture content maps, it is evident that the estimated moisture content maps approach the actual content maps as the simulation proceeds. This can be seen in the the evolution of the absolute error maps with time for both the surface and the bottom of the field. On Day 2, appreciable absolute error values are observed, as shown in Figures 3.9(c) and 3.12(c). These absolute error values decrease and approach 0 as the simulation proceeds and on Day 5, every location of the field attains an absolute error value of 0 or close to 0, as shown in Figures 3.11(c) and 3.14(c).

From Figure 3.9(c), it can be seen that, even though some locations posses appreciable absolute error values, most locations on the surface have absolute error values of 0. This occurrence signifies that most of the estimates of the states located on the surface converge on Day 2. For the bottom of the field, it can be seen that most states still posses an appreciable absolute error value on the second day, as shown in Figure 3.12 (c). Consequently, the actual moisture content map, Figure 3.12 (a), differs markedly from the estimated moisture content map, Figure 3.12 (b) on Day 2. These observations confirm the fact that the estimates of states located on the surface converge faster than other estimates and that the farther a state is from the surface, the longer it takes for its estimate to converge.

Next, the performance of the EKF is investigated in the presence of parameter uncertainty.

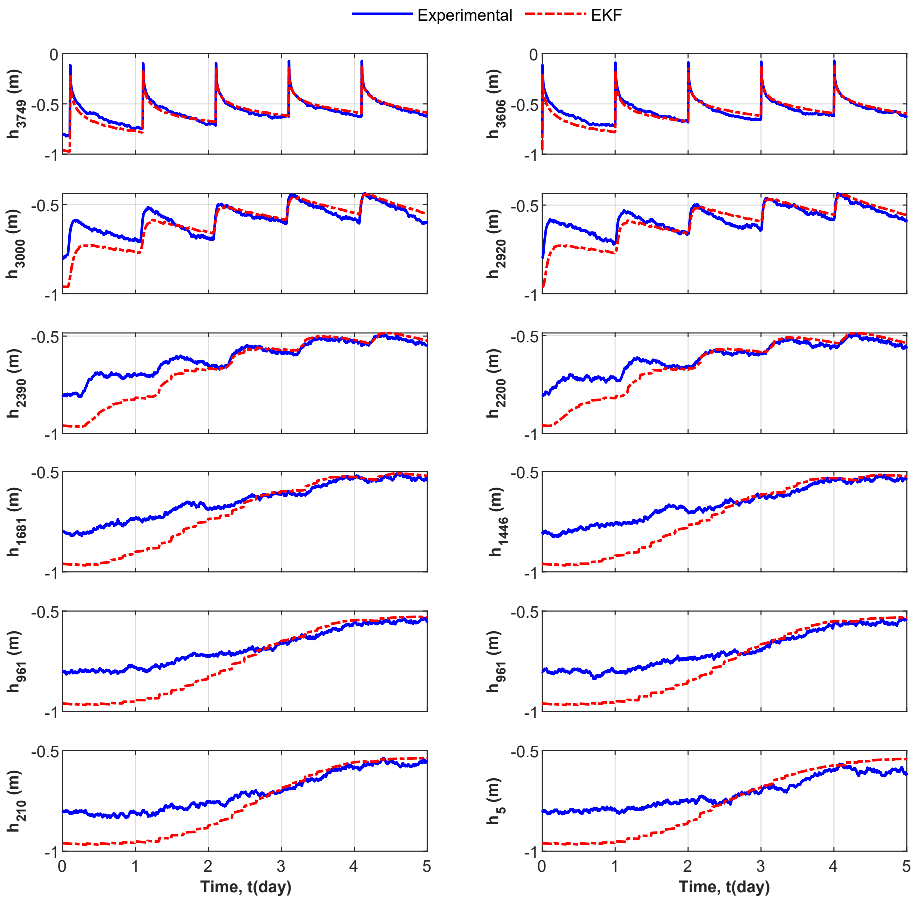

Figure 3.15: Selected trajectories of the actual process state and the state estimates in the parameter uncertain case of Scenario 1.

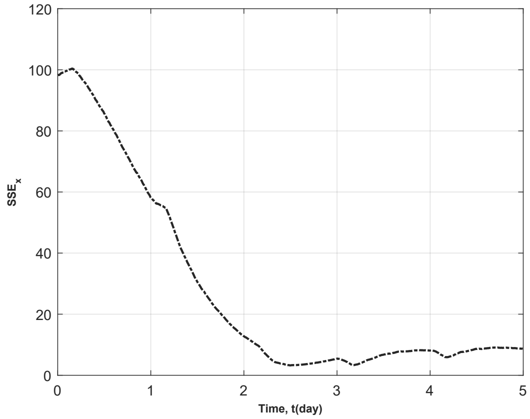

Figure 3.16: Trajectory of the SSE_x in the parameter uncertain case of Scenario 1.

From Figure 3.15, it can be seen that EKF can track the actual process states fairly well, especially for states located on and close to the surface of the field, and the state estimates are within reasonable error bounds from the actual process states. However, the tracking ability of the EKF declines when parameter uncertainty is introduced. It can be observed that there exist a noticeable offset, which is more prominent for states which are located far away from the surface, between the estimates provided by the EKF (red dash-dot) and the actual process state (solid blue line).

The decline in the performance of the EKF is further confirmed by the trajectory of SSE_x. From Figure 3.16, the SSE_x converges to a value of 8.5, which is higher than what is observed in the normal case. This explains the noticeable offset between the estimates of the states and the actual process states in the presence of parameter uncertainty. Similar to the normal case, it is observed that the estimates of the states on the surface of the field converge faster than other locations and the farther a state is from the surface, the longer it takes for its estimates to converge.

Next, the moisture content maps in the presence of parameter uncertainty are analysed.

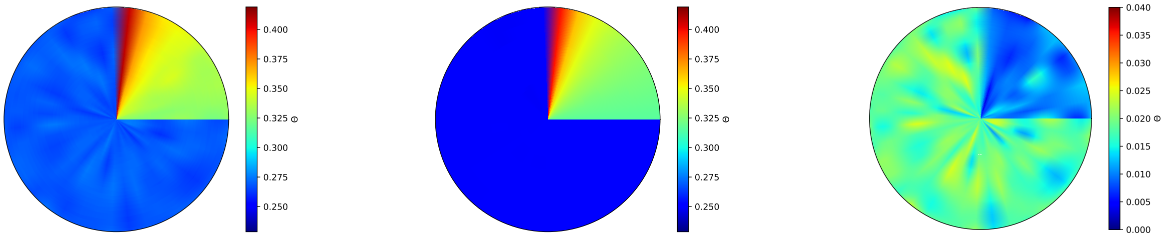

(a) Actual map. (b) Estimated map. (c) Absolute error map.

Figure 3.17: Surface moisture content maps at 1:00 HRS on Day 2 for the parameter uncertain case of Scenario 1.

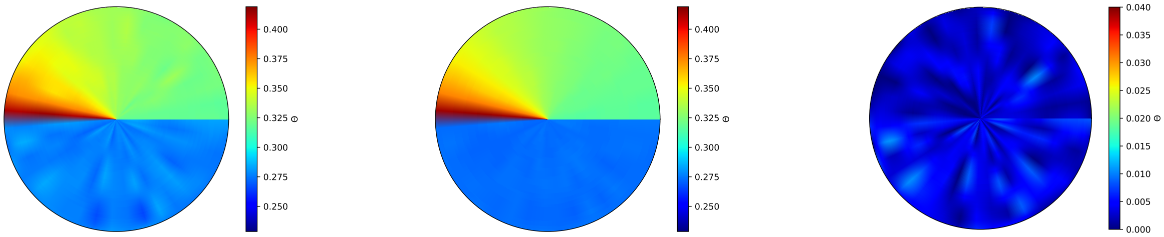

(a) Actual map.
(b) Estimate map.
(c) Absolute error map.

Figure 3.18: Surface moisture content maps at 2:00 HRS on Day 4 for the parameter uncertain case of Scenario 1.

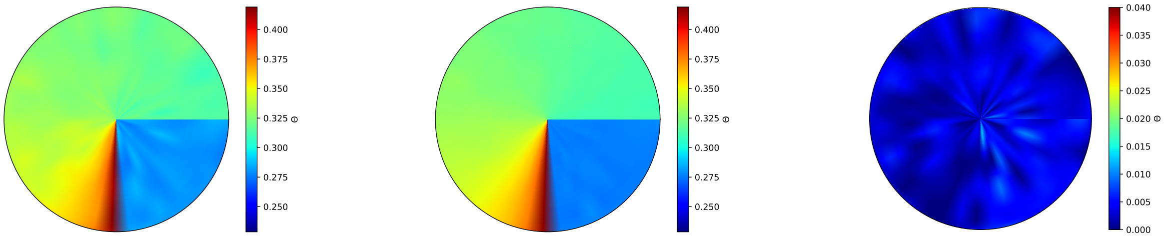

(a) Actual map.
(b) Estimated map.
(c) Absolute error map.

Figure 3.19: Surface moisture content maps at 3:00 HRS on Day 5 for the parameter uncertain case of Scenario 1.

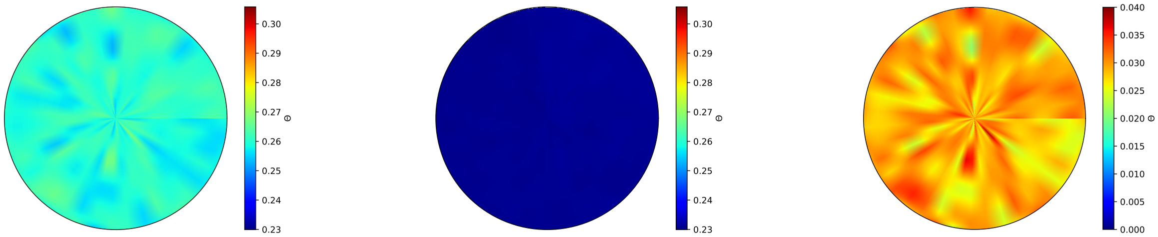

(a) Actual map.
(b) Estimated map.
(c) Absolute error map.

Figure 3.20: Maps at a depth of 0.3 m on Day 1 at 1:00 HRS for the parameter uncertain case of Scenario 1.

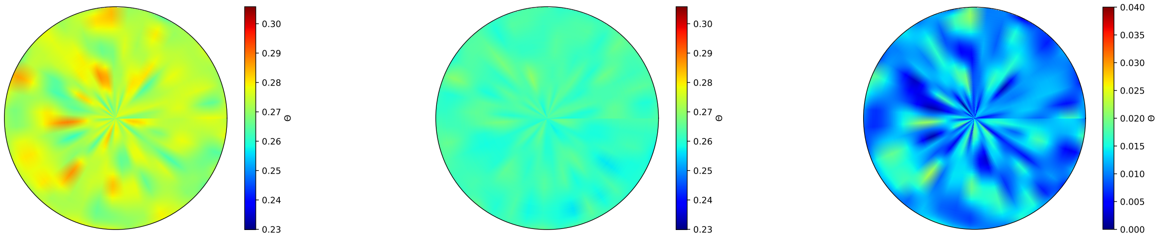

(a) Actual map.

(b) Estimated map.

(c) Absolute error map.

Figure 3.21: Maps at a depth of 0.3 m on Day 4 at 2:00 HRS for the parameter uncertain case of Scenario 1.

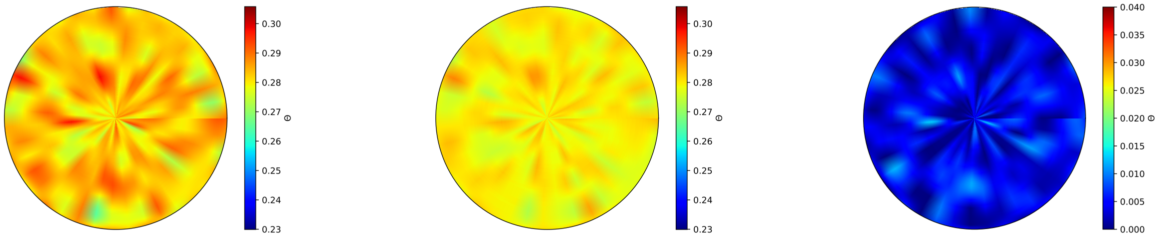

(a) Actual map.

(b) Estimated map.

(c) Absolute error map.

Figure 3.22: Maps at a depth of 0.3 m on Day 5 at 3:00 HRS for the parameter uncertain case of Scenario 1.

In the presence of parameter uncertainty, just like the normal case, it is evident that the estimated moisture content maps approach the actual content maps as the simulation advances. On Day 2, appreciable absolute error values are observed for most locations on the surface and the bottom of the field, as shown in Figures 3.17(c) and 3.20(c). These appreciable error values decrease and approach a value of 0 as the simulation proceeds. On Day 5, it is observed that the estimated moisture maps closely resemble the actual moisture maps, as shown in Figures 3.19(b), 3.19(a), 3.22(b) and 3.22(a).

There however exist some noticeable differences between the maps constructed in the parameter uncertain case and those constructed for the normal case. Comparing the maps generated in the two cases, it is observed that in the presence of parameter uncertainty, the estimates of all the states in the investigated field take longer to converge. In the normal case, it was observed that most estimates of the states located on the surface of the field converged on Day 2. A different observation is made in the presence of parameter uncertainty. From Figure 3.17(c), we observe that most locations on the surface of the field posses an appreciable absolute error on Day 2. Consequently, it cannot be said that most of the estimates of states on the surface have converged on the second day. A similar observation can be made for the bottom maps. In the normal case, it is observed that the absolute error values for Day 4 are closer to 0 than the observed absolute error values in the parameter uncertain case for the same day. On Day 4, in the parameter uncertain case, some locations at the bottom of the field still posses appreciable absolute error values.

Albeit a decline in tracking ability and a longer convergence of the estimates, in the presence of parameter uncertainty, the EKF is still able to provide moisture content maps which are within negligible error bounds at the end of the simulation period, as shown in Figures 3.19(c) and 3.22(c).

3.4.3 Scenario 2

In this scenario, the field is investigated in the presence of nonuniform initial conditions and a single soil type. This scenario is motivated by the fact that, it is usually common to find a nonuniform volumetric moisture content distribution and hence a nonuniform pressure head distribution across a field before the start of the irrigation cycle. Randomly generated pressure head values between -0.8 m and -0.9 m are used as the initial conditions in this scenario. Consequently, each node or state has a different initial condition. The soil type considered in this scenario is loamy soil. The soil parameters in Table 3.1 are thus used in the normal and parameter uncertain cases for this scenario.

The EKF is initialized with $\hat{x}_0 = 1.2 \times x_0$ and the simulation is performed for 5 days.

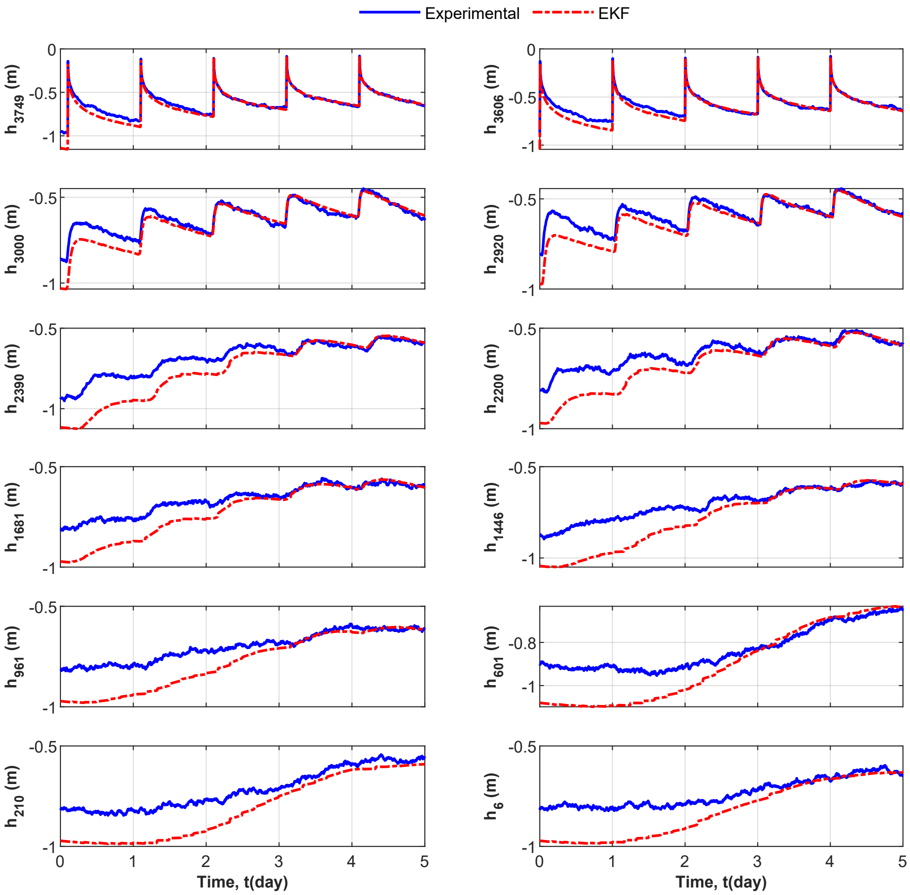

Figure 3.23: Selected trajectories of the actual process states and the state estimates in the normal case of Scenario 2.

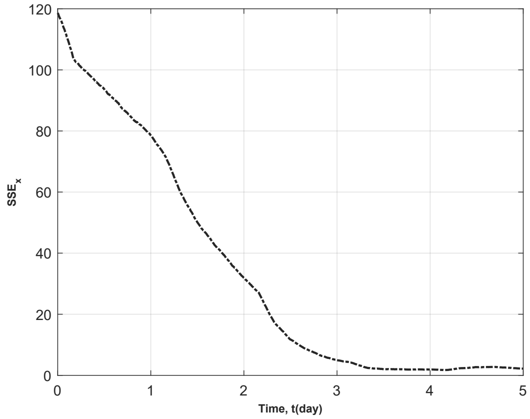

Figure 3.24: Trajectory of the SSE$_x$ in the normal case of Scenario 2.

From Figure 3.23, it can be seen that the EKF provides accurate estimates and the estimates of states located on the surface of the field converges faster than the other estimates. It is also clear from Figure 3.24 that there is a monotonic decrease in the SSE_x from the beginning of the simulation up to about 3.5 days after which the SSE_x stays constant. This observation is similar to the normal case in Scenario 1 except that the SSE_x in Scenario 2 has a higher initial value and also converges to a slightly higher value. In summary, the EKF maintains its good performance in the presence of nonuniform initial conditions.

Next, the moisture content maps in this scenario are analysed.

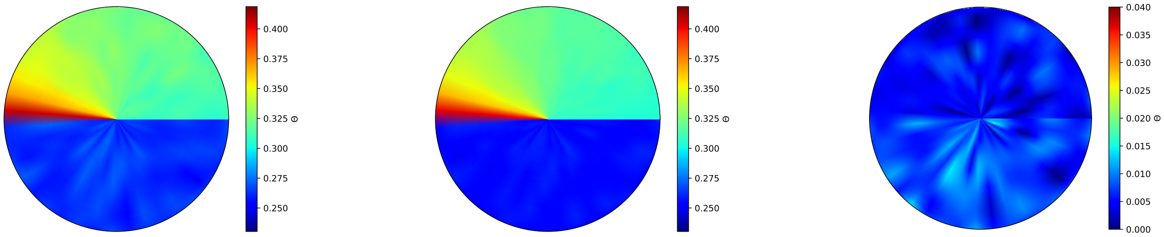

(a) Actual map.
(b) Estimated map.
(c) Absolute error map.

Figure 3.25: Surface moisture content maps at 02:00 HRS on Day 2 for the normal case of Scenario 2.

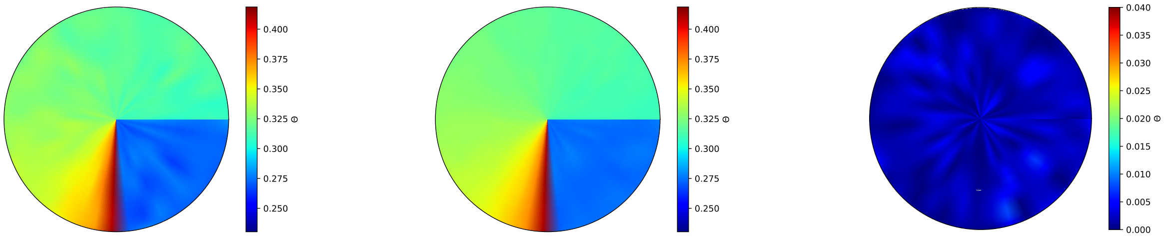

(a) Actual map.
(b) Estimated map.
(c) Absolute error map.

Figure 3.26: Surface moisture content maps at 03:00 HRS on Day 4 for the normal case of Scenario 2.

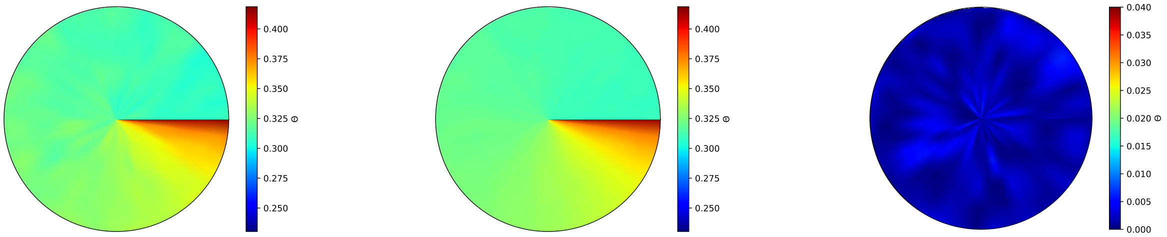

(a) Actual map. (b) Estimated map. (c) Absolute error map.

Figure 3.27: Surface moisture content maps at 04:00 HRS on Day 5 for the normal case of Scenario 2.

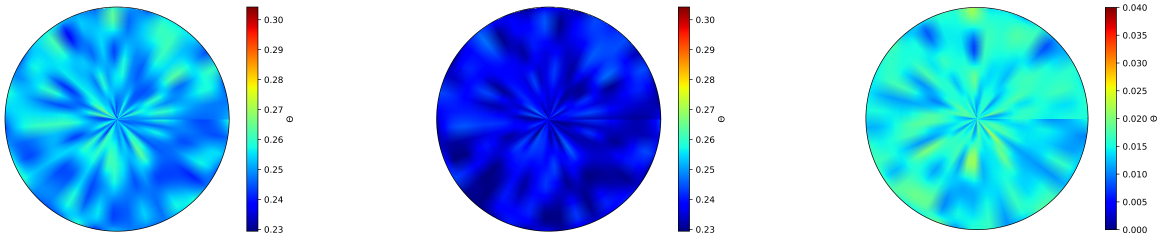

(a) Actual map. (b) Estimated map. (c) Absolute error map.

Figure 3.28: Maps at a depth of 0.3 m on Day 2 at 02:00 HRS for the normal case of Scenario 2.

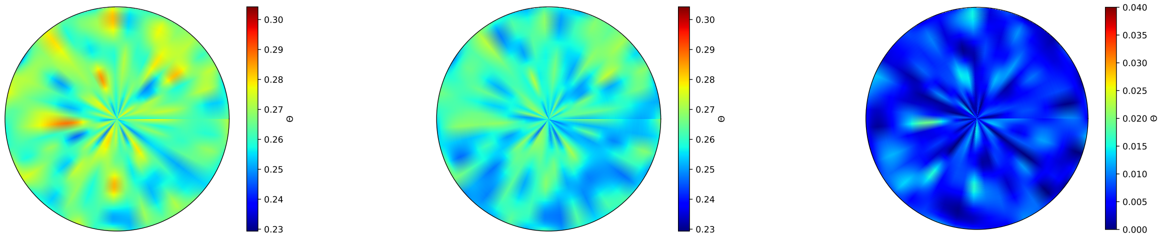

(a) Actual map. (b) Estimated map. (c) Absolute error map.

Figure 3.29: Maps at a depth of 0.3 m on Day 4 at 03:00 HRS for the normal case of Scenario 2.

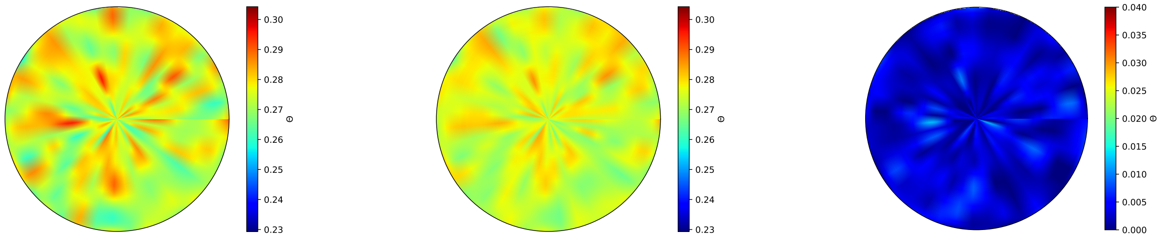

(a) Actual map.

(b) Estimated map.

(c) Absolute error map.

Figure 3.30: Maps at a depth of 0.3 m on Day 5 at 04:00 HRS for the normal case of Scenario 2.

From the surface maps and the maps constructed for the bottom of the field, it is evident that the estimated maps approach the actual maps as the simulation proceeds. At the end of the simulation period, the EKF provides estimates whose moisture content maps are the same as the actual maps, especially for the surface of the field. The maps generated for the bottom of the field are also within negligible error bounds from the actual maps.

Next, we study the performance of the EKF in the parameter uncertain case of this scenario.

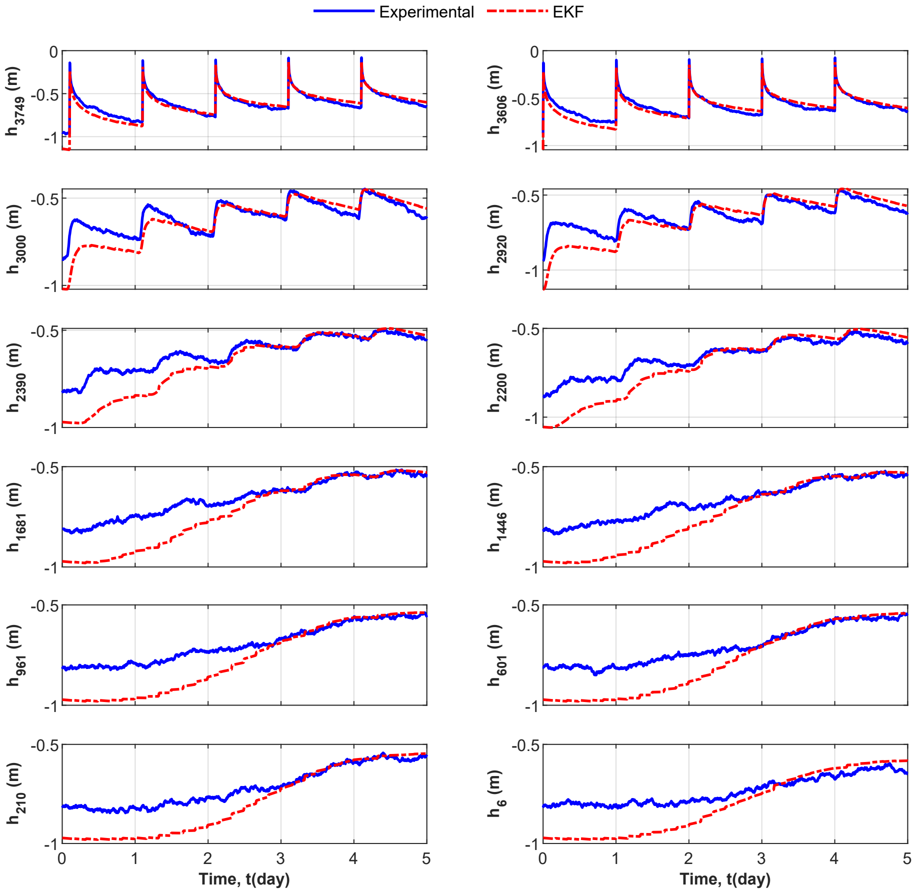

Figure 3.31: Selected trajectories of the actual process state and the state estimates in the parameter uncertain case of Scenario 2.

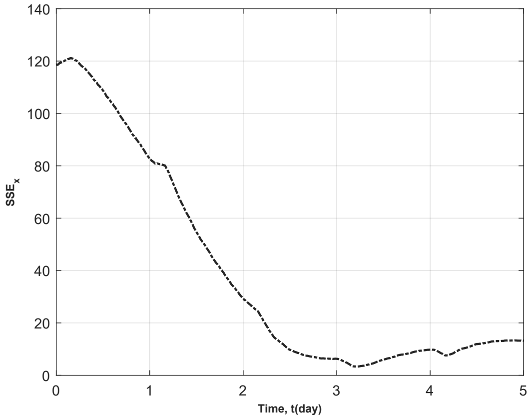

Figure 3.32: Trajectory of the SSE$_x$ in the parameter uncertain case of Scenario 2.

Similar to Scenario 1, the tracking ability of the EKF reduces in the presence of parameter uncertainty. There is a noticeable offset between the estimates of the states and the true process states especially for states which are far away from the surface. The trajectory of the SSEx, shown in Figure 3.32, also confirms that the performance of the EKF degrades when parameter uncertainty is introduced into the EKF. Compared to the normal case, the SSE_x in the parameter uncertain case converges to a much higher value.

Next, the moisture content maps in the parameter uncertain case are analyzed.

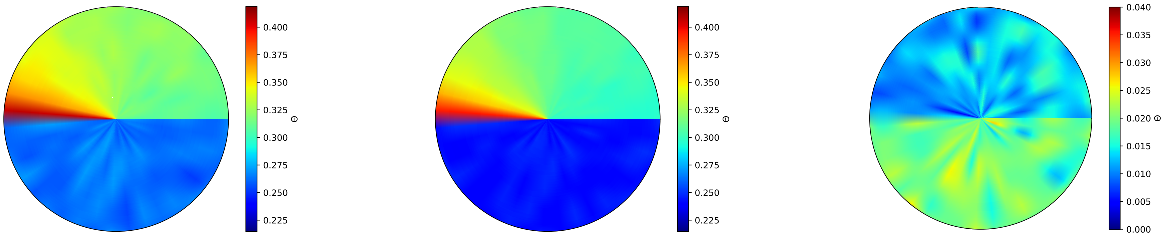

(a) Actual map.
(b) Estimated map.
(c) Absolute error map.

Figure 3.33: Surface moisture content maps at 02:00 HRS on Day 2 for the parameter uncertain case of Scenario 2.

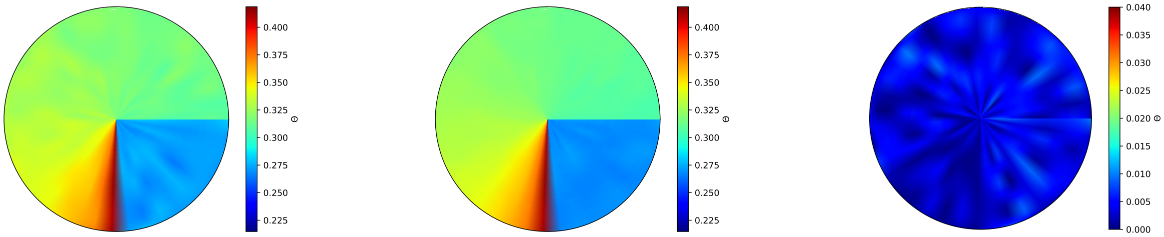

(a) Actual map.
(b) Estimated map.
(c) Absolute error map.

Figure 3.34: Surface moisture content maps at 03:00 HRS on Day 4 for the parameter uncertain case of Scenario 2.

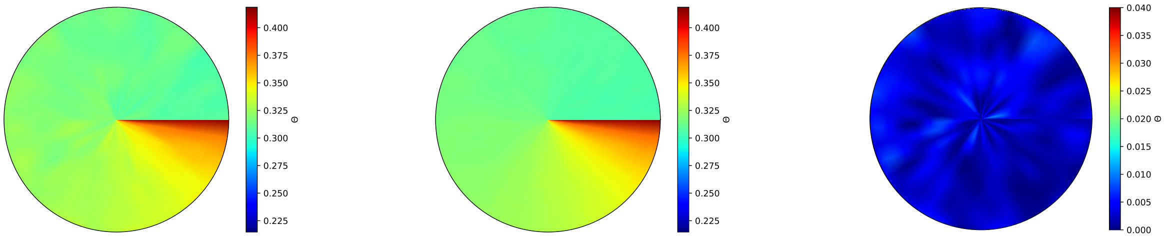

(a) Actual map. (b) Estimated map. (c) Absolute error map.

Figure 3.35: Surface moisture content maps at 04:00 HRS on Day 5 for the parameter uncertain case of Scenario 2.

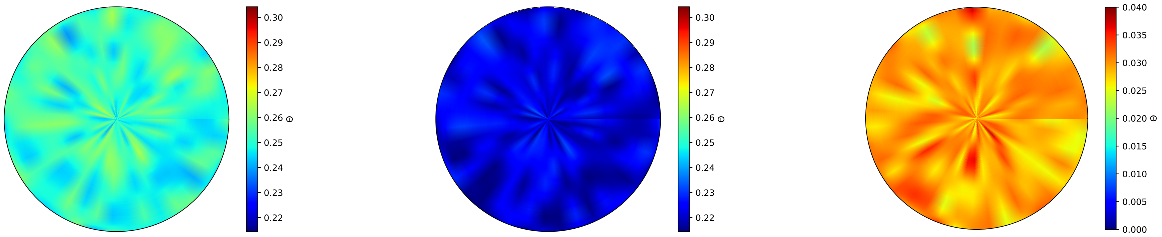

(a) Actual map. (b) Estimated map. (c) Absolute error map.

Figure 3.36: Maps at a depth of 0.3 m on Day 2 at 02:00 HRS for the parameter uncertain case of Scenario 2.

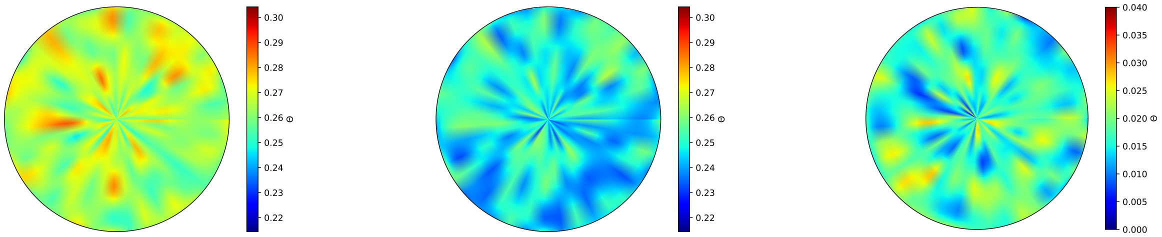

(a) Actual map. (b) Estimated map. (c) Absolute error map.

Figure 3.37: Maps at a depth of 0.3 m on Day 4 at 03:00 HRS for the parameter uncertain case of Scenario 2.

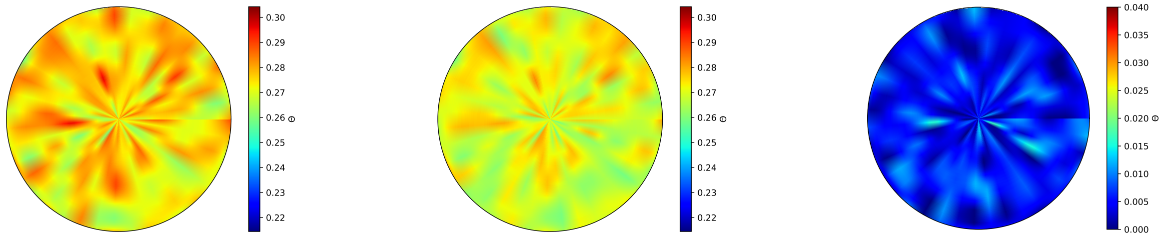

(a) Actual map.

(b) Estimated map.

(c) Absolute error map.

Figure 3.38: Maps at a depth of 0.3 m on Day 5 at 04:00 HRS for the parameter uncertain case of Scenario 2.

From the moisture content maps, it is evident that in the presence of parameter uncertainty, the estimates take longer to converge. It is also clear that even though the tracking ability of the EKF declines, in the presence of the parameter uncertainty, the estimated maps obtained towards the end of the simulation are within negligible error bounds from the actual maps, as can be seen in Figures 3.35 o(c) and 3.38(c).

3.4.4 Scenario 3

In nature, soils are seldom uniform over significant length scales, and layered soils are ubiquitous [45]. In this scenario, a field made up of two soil layers is considered. Specifically, the investigated field is made of a loamy layer and a sandy clay loam layer. The loamy layer occupies a depth of 0.16 m while the sandy clay loam layer occupies a depth of 0.14 m and the loamy layer is above the sandy clay loam layer as shown in Figure 3.39.

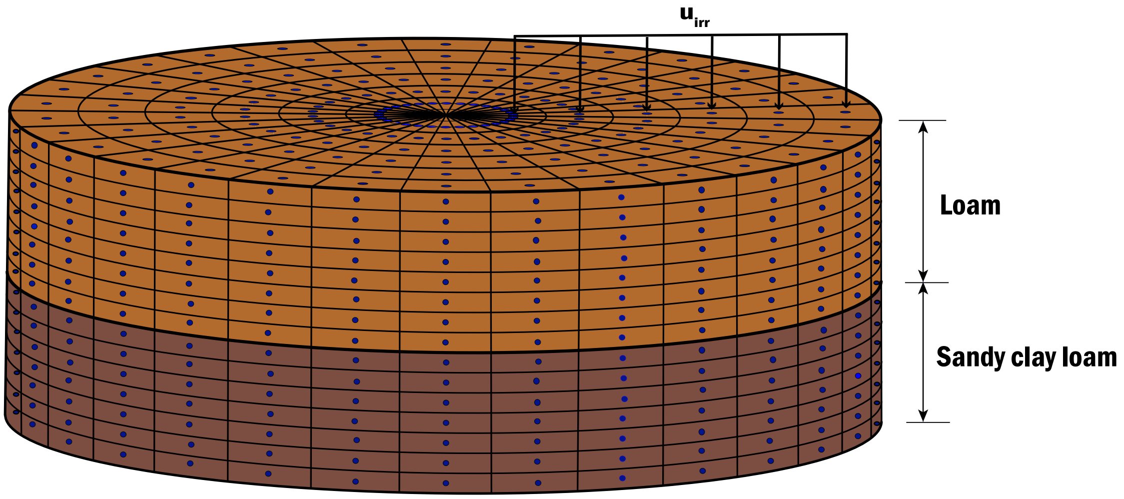

Figure 3.39: A schematic diagram of the investigated field in Scenario 3.

The hydraulic properties of sandy clay loam are shown in Table 3.2.

Table 3.2: The hydraulic parameters of sandy clay loam soil.

	K_s (m/s)	θ_s (m^3/m^3)	θ_r (m^3/m^3)	α (1/m)	n (-)
Normal case	7.222×10^{-7}	0.410	0.090	1.90	1.31
Parameter uncertain case	7.581×10^{-7}	0.431	0.095	2.00	1.38

In layered soils, the volumetric water content is discontinuous across the interface between the layers because of the unique capillary head relationships in different soils of layers [46]. Rather, the pressure head which represents the state in this work is continuous across the layers [45]. Thus in this scenario, it is suitable to directly use the pressure head values at the measured nodes as the output, y, in the update step of the EKF. This results in a modification of the output function in the state space representation of the field model. In this scenario, the output function is

$$y_k = C_k x_k + v_k \tag{3.31}$$

C_k is a matrix whose entries are made up of 0's and 1's and it is used to determine the measured states.

Uniform initial conditions are assumed in this scenario and the EKF is initialized with $\hat{x}_0 = 1.2 \times x_0$. The simulation is performed for 5 days.

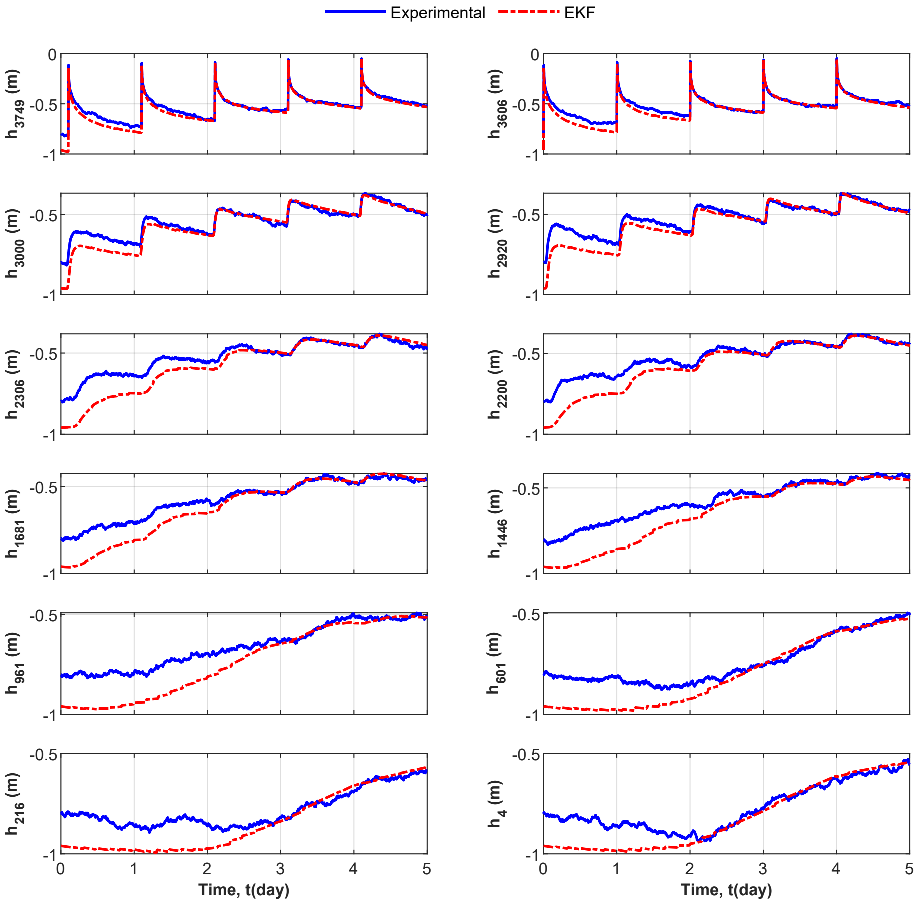

Figure 3.40: Selected trajectories of the actual process states and the state estimates in the normal case of Scenario 3.

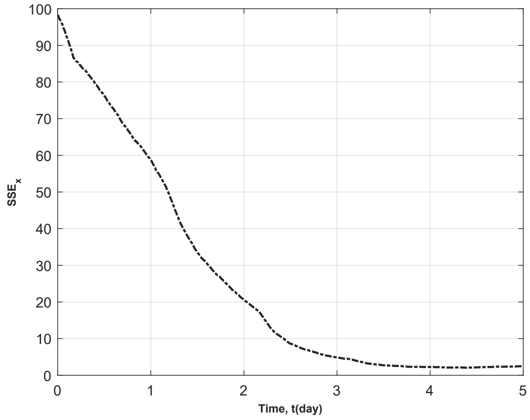

Figure 3.41: Trajectory of the SSE$_x$ in the normal case of Scenario 3.

From Figure 3.40, it is evident that the EKF produces accurate estimates when a layered field is considered. As shown in Figure 3.40, the estimates of the states located in the sandy clay loam layer (h_4, h_{216}, h_{601}, h_{961}, h_{1446}, h_{1681}) can track their corresponding true process states very well. A similar observation is made for the estimates of the states located in the loam layer (h_{2200}, h_{2306}, h_{2920}, h_{3000}, h_{3606}, h_{3749}) although these estimates are observed to converge faster than the estimates in the sandy clay loam layer. This is because these states are closer to the surface of the field. The trajectory of the SSE$_x$ in Figure 3.41 exhibits a monotonic decrease from the beginning of the simulation until about 3.5 days after which it assumes a constant value.

The moisture content maps for the normal case of the layered field are analysed in the sequel.

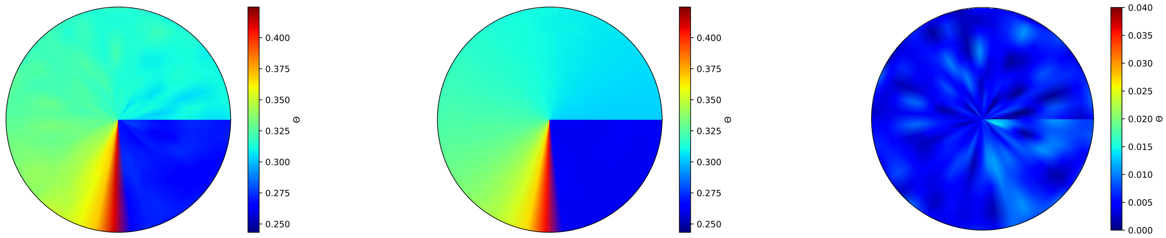

(a) Actual map.

(b) Estimated map.

(c) Absolute error map

Figure 3.42: Surface moisture content maps at 03:00 HRS on Day 2 for the normal case of Scenario 3.

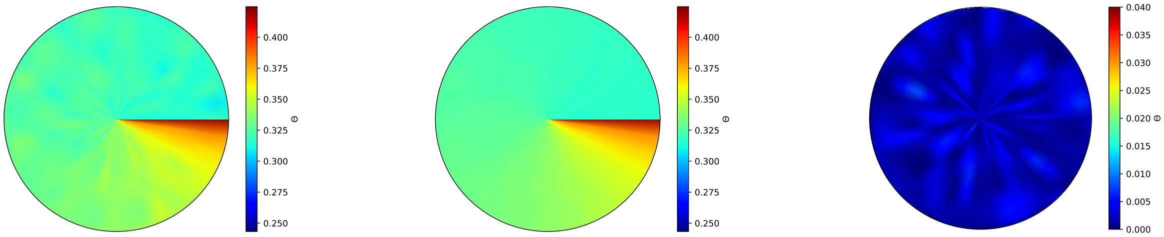

(a) Actual map. (b) Estimated map. (c) Absolute error map.

Figure 3.43: Surface moisture content maps at 04:00 HRS on Day 4 for the normal case of Scenario 3.

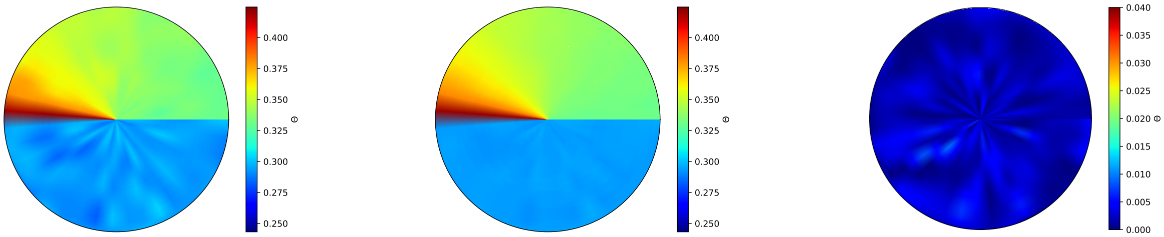

(a) Actual map. (b) Estimated map. (c) Absolute error map.

Figure 3.44: Surface moisture content maps at 02:00 HRS on Day 5 for the normal case of Scenario 3.

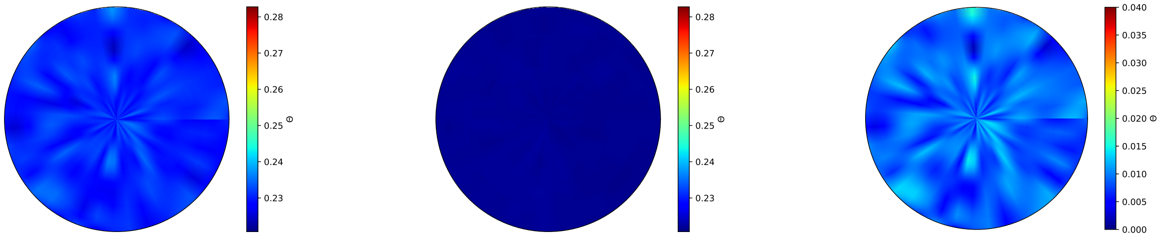

(a) Actual map. (b) Estimated map. (c) Absolute error map.

Figure 3.45: Maps at a depth of 0.3 m on Day 2 at 3:00 HRS for the normal case of Scenario 3

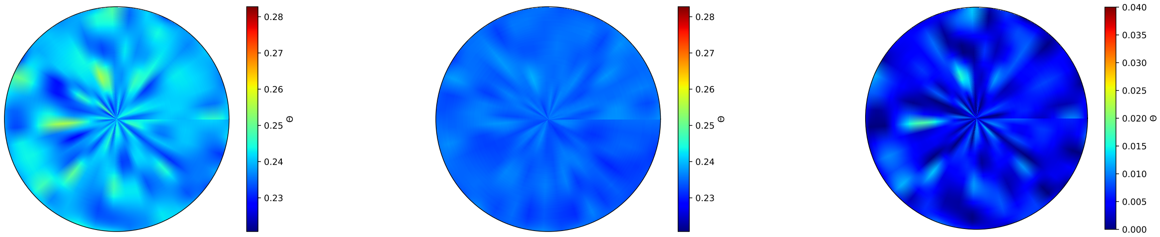

(a) Actual map. (b) Estimated map. (c) Absolute error map.

Figure 3.46: Maps at a depth of 0.3 m on Day 4 at 04:00 HRS for the normal case of Scenario 3.

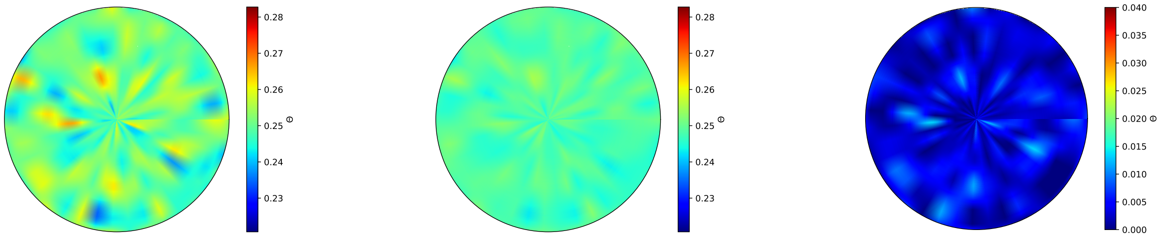

(a) Actual map. (b) Estimated map. (c) Absolute error map.

Figure 3.47: Maps at a depth of 0.3 m on Day 5 at 02:00 HRS for the normal case of Scenario 3.

The surface maps and the bottom maps are located in the loam and sandy clay loam layers respectively. From these moisture content maps, there is a strong agreement between the estimated maps and the actual moisture content maps as the simulation proceeds. These maps also confirm that the estimates of the states located in the loam layer converge faster than the estimates of the states located in the sandy clay loam layer.

Next, we study the performance of the EKF in the presence of parameter uncertainty for a layered field.

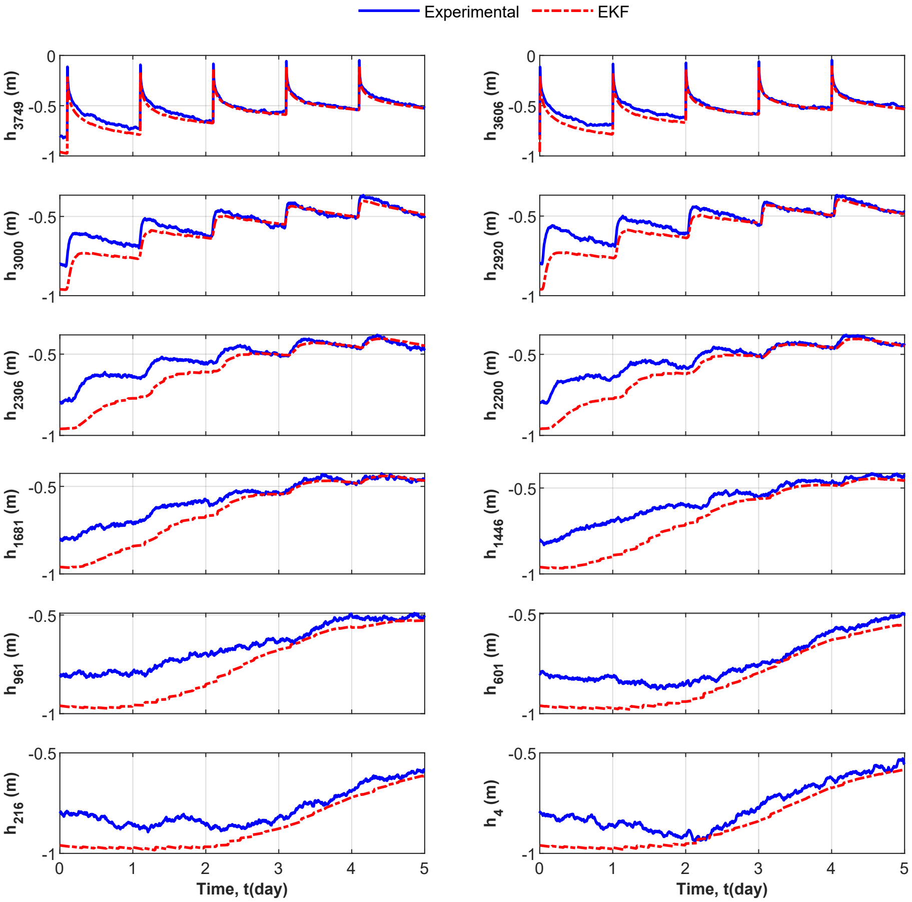

Figure 3.48: Selected trajectories of the actual process states and the state estimates in the parameter uncertain case of Scenario 3.

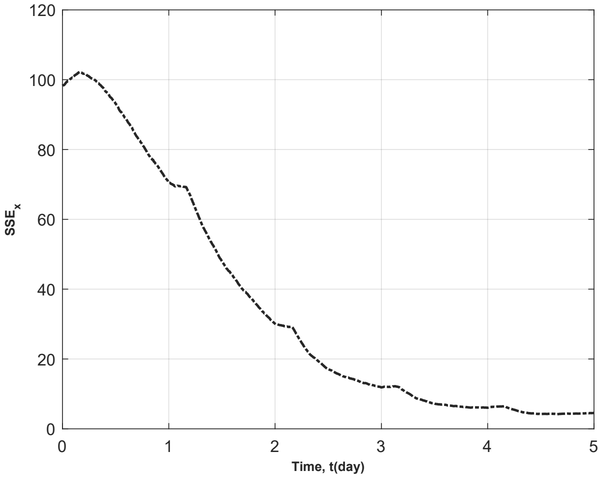

Figure 3.49: Trajectory of the SSE_x in the parameter uncertain case of Scenario 3.

In the presence of parameter uncertainty, for a layered field, we observe from Figure 3.48 that the estimates of the states located in the loam layer can track their corresponding true process states very well. For the states located in the sandy clay loam layer, even though the estimates tend to approach the true process states, there is a noticeable offset between them. The decline in the performance of the EKF in the presence of parameter uncertainty is evident in the trajectory of the SSE_x in Figure 3.49. From the figure, the SSE_x is seen to converge after about 4.5 days and it tends to converge to a much higher value compared to the normal case.

The moisture content maps in the presence of parameter uncertainty are discussed next.

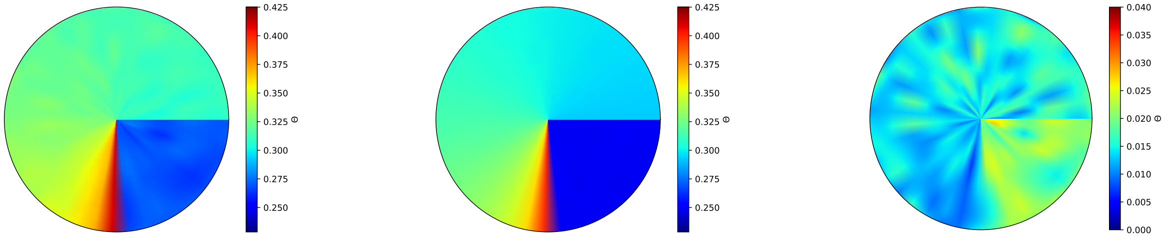

(a) Actual map. (b) Estimated map. (c) Absolute error map.

Figure 3.50: Surface moisture content maps at 3:00 HRS on Day 2 for the parameter uncertain case of Scenario 3.

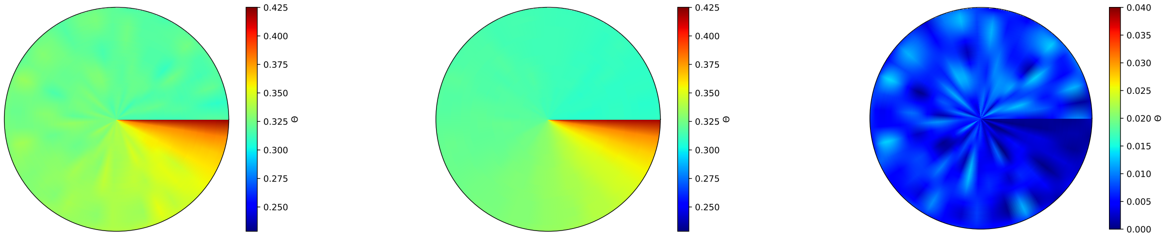

(a) Actual map. (b) Estimated map. (c) Absolute error map.

Figure 3.51: Surface moisture content maps at 4:00 HRS on Day 4 for the parameter uncertain case of Scenario 3

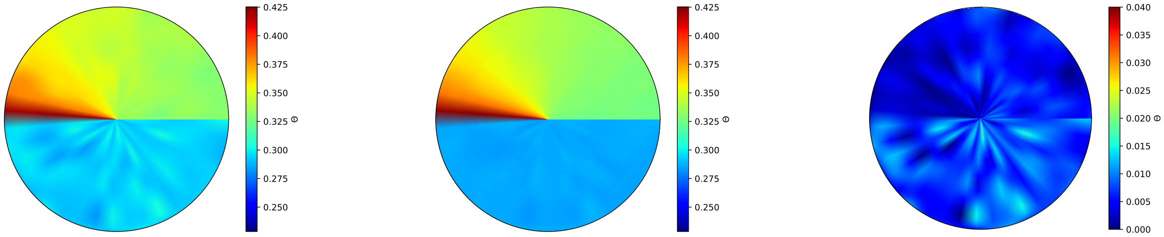

(a) Actual map. (b) Estimated map. (c) Absolute error map.

Figure 3.52: Surface moisture content maps at 02:00 HRS on Day 5 for the parameter uncertain case of Scenario 3.

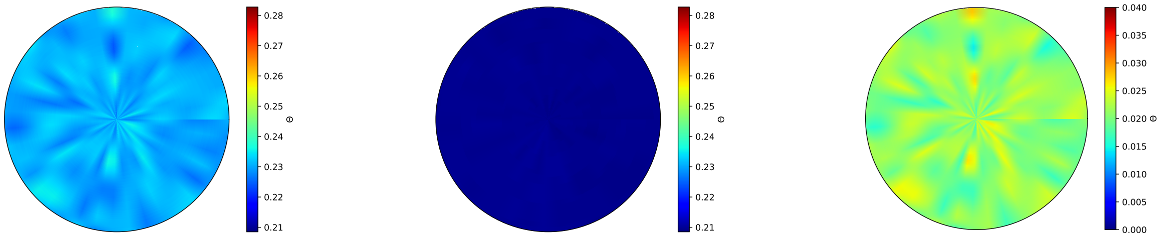

(a) Actual map. (b) Estimated map. (c) Absolute error map.

Figure 3.53: Maps at a depth of 0.3 m on Day 2 at 03:00 HRS for the parameter uncertain case of Scenario 3.

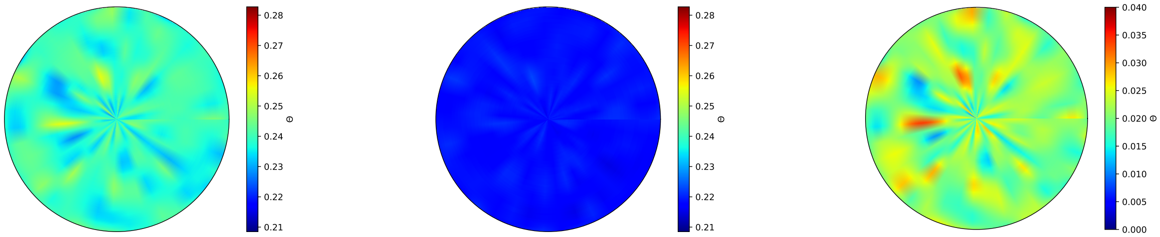

(a) Actual map. (b) Estimated map. (c) Absolute error map.

Figure 3.54: Maps at a depth of 0.3 m on Day 4 at 04:00 HRS for the parameter uncertain case of Scenario 3.

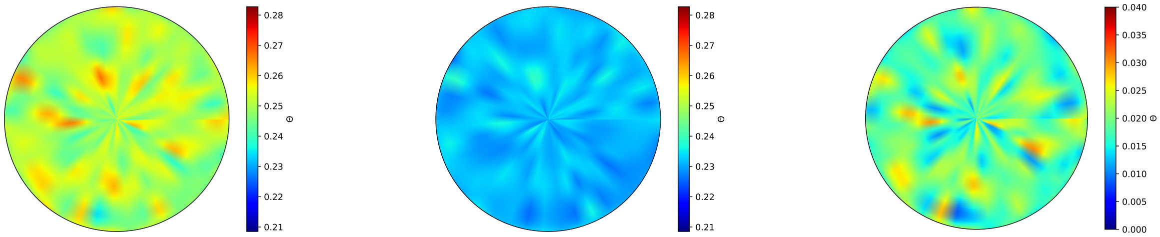

(a) Actual map.

(b) Estimated map.

(c) Absolute error map.

Figure 3.55: Maps at a depth of 0.3 m on Day 5 at 02:00 HRS for the parameter uncertain case of Scenario 3.

In the presence of parameter uncertainty, it can be seen that the estimates of the states in both layers take longer to converge. This is pronounced in the estimates of the states located in the sandy clay loam layer. For the states in the loamy layer, it is observed that the estimated maps (Figures 3.51(b) and 3.52(b)) on Days 4 and 5 are similar to the actual maps (Figures 3.51(a) and 3.52(a)). For the bottom maps, we observe that even though the absolute error values for most locations decrease as the simulation proceeds, the absolute error map (Figure 3.55(c)) on Day 5 still shows appreciable absolute error values for some locations. These error values, though appreciable, are however within reasonable bounds.

3.4.5 Scenario 4

In this scenario, the simulation is performed with soil hydraulic parameters obtained from a soil texture survey experiment conducted on a demo farm, located at the Alberta Irrigation Center in Lethbridge. The soil hydraulic parameters are represented with the following maps.

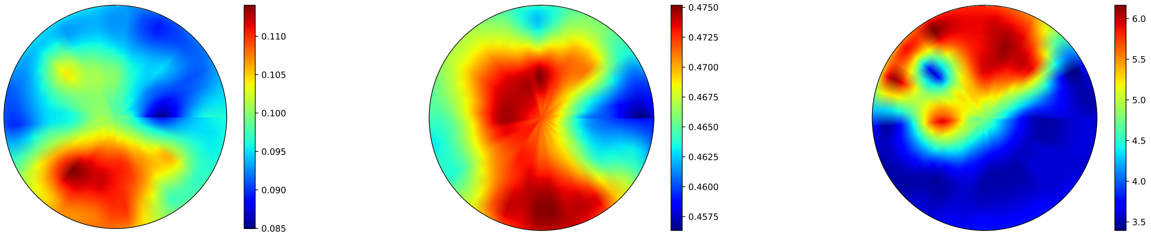

(a) θ_r (b) θ_s (c) α

(d) n (e) K_s

From the maps, it can be seen that each state or node possesses a unique set of soil hydraulic parameters. This occurrence gives rise to a nonuniform soil type across the field and so it is suitable to use Equation (3.31) as the output function in the update step of the EKF. In this scenario too, uniform initial conditions are assumed and the EKF is also initialized with $\hat{x}_0 = 1.2 \times x_0$. The simulation is performed for 8 days and 9 days in the normal and parameter uncertain cases respectively.

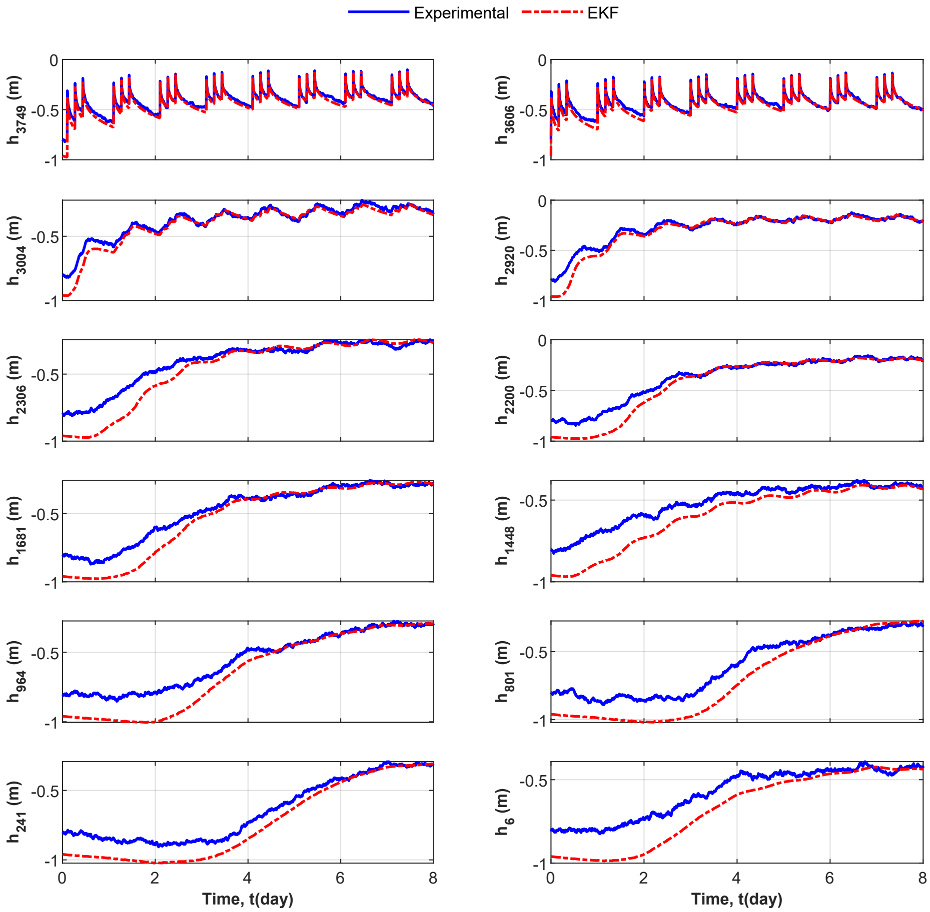

Figure 3.56: Selected trajectories of the actual process states and the state estimates in the normal case of Scenario 4.

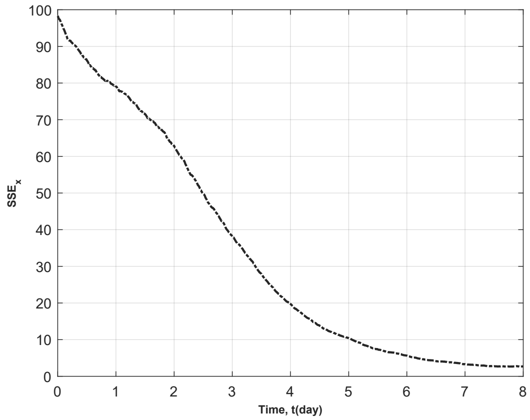

Figure 3.57: Trajectory of the SSE_x in the normal case of Scenario 4.

From Figure 3.56, it can be seen that the EKF provides very accurate estimates of the states. The estimates of the states located on the surface of the soil converge faster than the other estimates. From Figure 3.57, a monotonic decrease in the SSE$_x$ is observed up to about the 7th day, after which it attains a constant value. We can infer that all the estimates of the state in this scenario converge on the 7th day.

Comparing the trajectory of the SSE$_x$ in the normal case of this scenario with the trajectories of the SSE$_x$ in the normal cases of Scenarios 1, 2 and 3, it can be seen that when soil parameters vary from state (node) to state (node), the entire system takes longer to converge.

Next, the moisture content maps constructed in this scenario are analyzed.

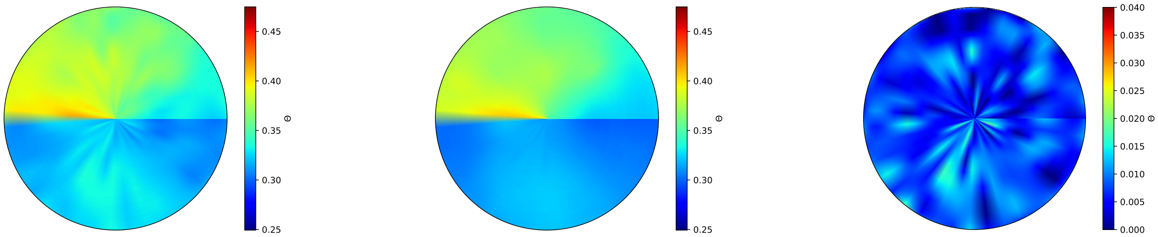

(a) Actual map. (b) Estimated map. (c) Absolute error map.

Figure 3.58: Surface moisture content maps at 02:00 HRS on Day 2 for the normal case of Scenario 4.

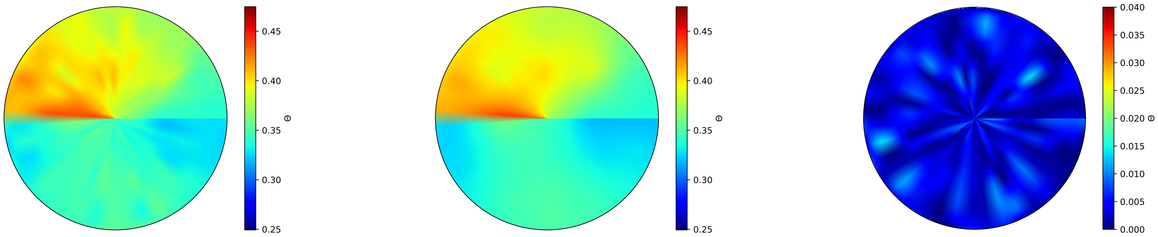

(a) Actual map. (b) Estimated map. (c) Absolute error map.

Figure 3.59: Surface moisture content maps at 02:00 HRS on Day 4 for the normal case of Scenario 4.

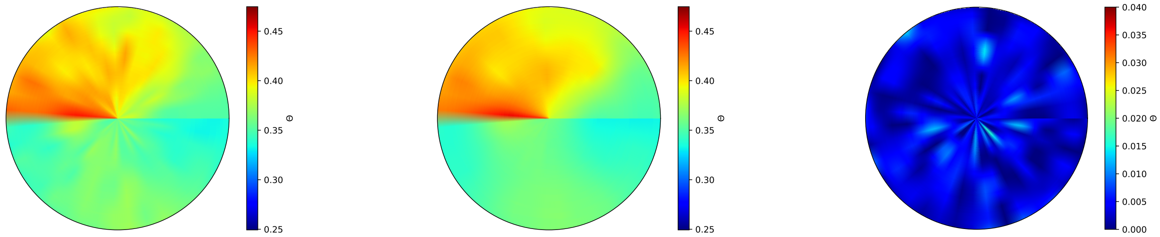

(a) Actual map. (b) Estimated map. (c) Absolute error map.

Figure 3.60: Surface moisture content maps at 02:00 HRS on Day 8 for the normal case of Scenario 4.

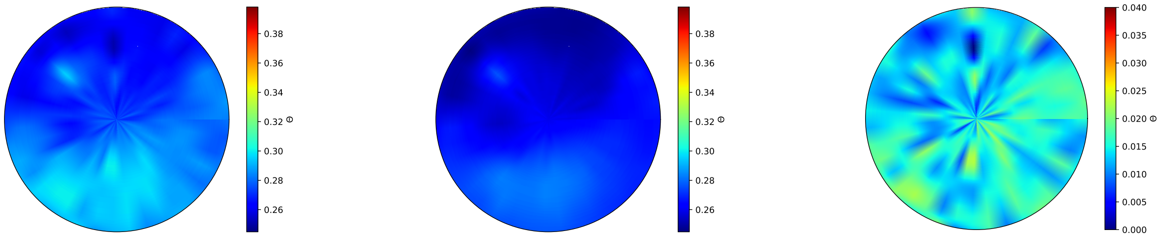

(a) Actual map. (b) Estimated map. (c) Absolute error map.

Figure 3.61: Maps at a depth of 0.3 m on Day 2 at 02:00 HRS for the normal case of Scenario 4.

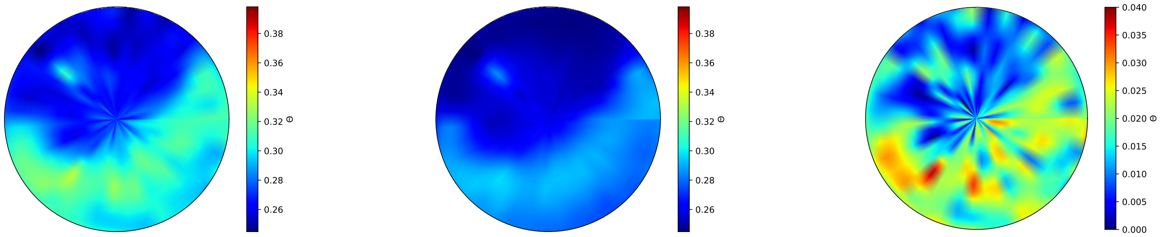

(a) Actual map. (b) Estimated map. (c) Absolute error map

Figure 3.62: Maps at a depth of 0.3 m on Day 4 at 02:00 HRS for the normal case of Scenario 4.

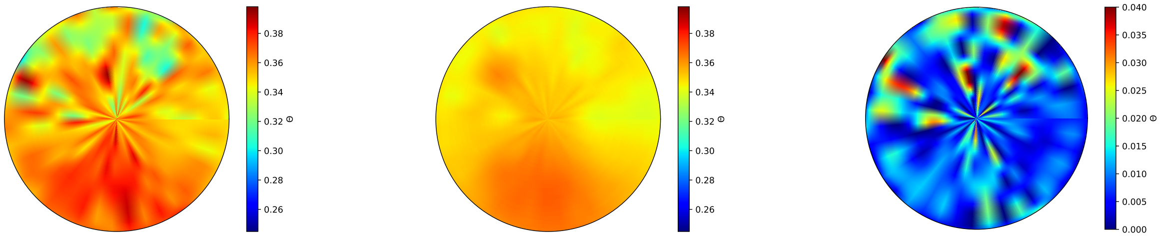

(a) Actual map. (b) Estimated map. (c) Absolute error map.

Figure 3.63: Maps at a depth of 0.3 m on Day 8 at 02:00 HRS for the normal case of Scenario 4.

From the moisture content maps, it is evident that the estimates of states located on the surface converge faster than the other estimates. The absolute error map, Figure 3.61(c), for the bottom maps initially depicts appreciable absolute error values, but these values reduce as the simulation progresses, as shown in Figure 3.62(c) which represents the absolute error map obtained on Day 4. On the 8th day, it can be observed that most locations at the bottom of the field attain absolute error values close to 0, as shown in Figure 3.63(c).

Next, we investigate the performance of the EKF in the presence of parameter uncertainty for this scenario.

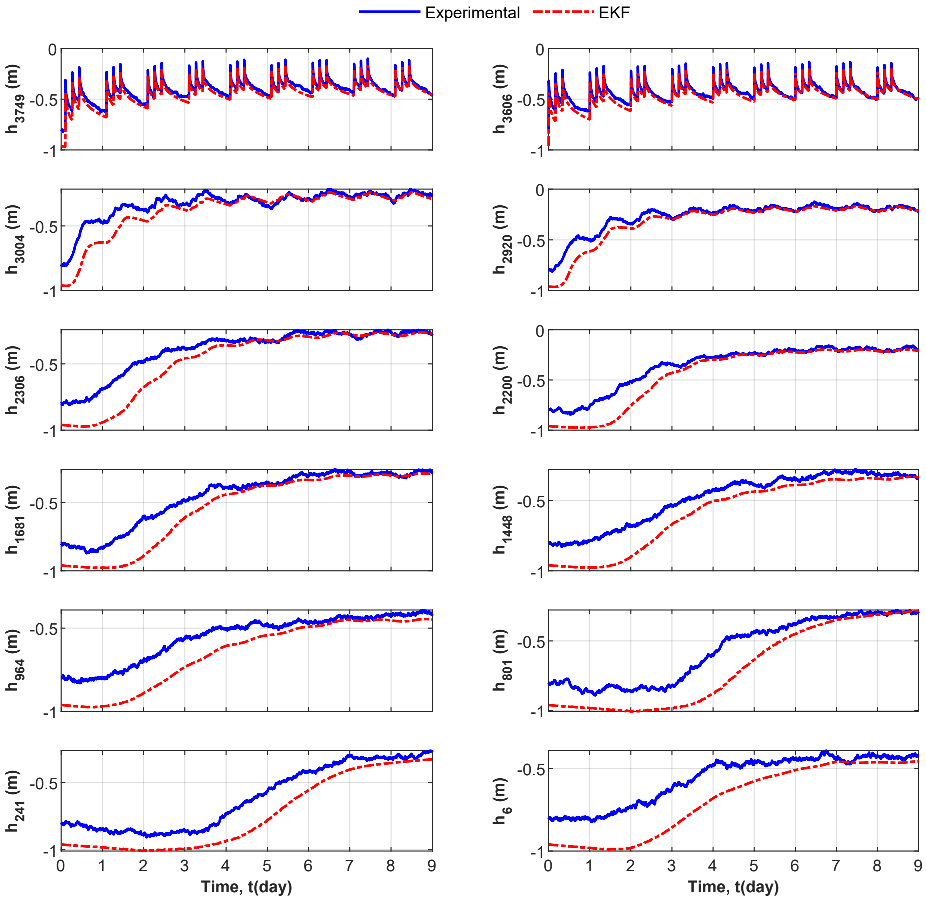

Figure 3.64: Selected trajectories of the actual process states and the state estimates in the parameter uncertain case of Scenario 4.

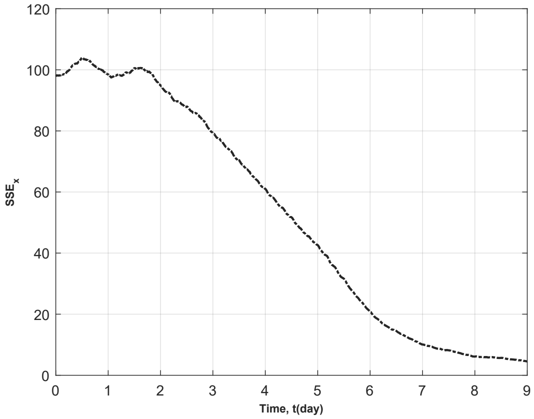

Figure 3.65: Trajectory of the SSE_x in the parameter uncertain case of Scenario 4.

From Figure 3.64, we observe that the EKF is still able to track the true process states.

However, there is a noticeable offset between the estimates and the true process states and this is more pronounced in states which are located far away from the surface of the field. From Figure 3.65, it is evident that the entire system, in the presence of parameter uncertainty, takes longer to converge, compared to the normal case of this scenario.

The moisture content maps constructed, in the presence of parameter uncertainty, are analyzed.

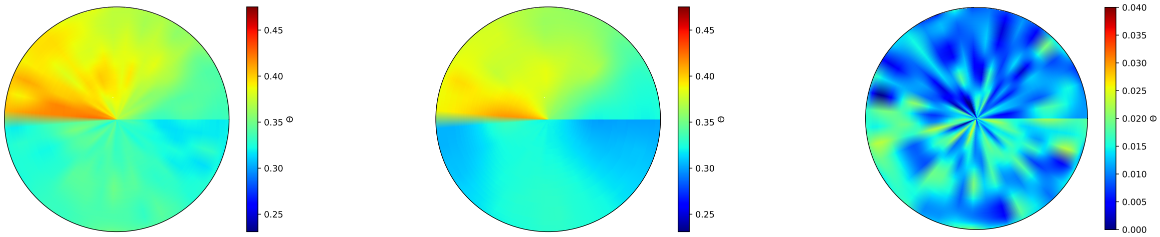

(a) Actual map. (b) Estimated map. (c) Absolute error map.

Figure 3.66: Surface moisture content maps at 02:00 HRS on Day 3 for the parameter uncertain case of Scenario 4.

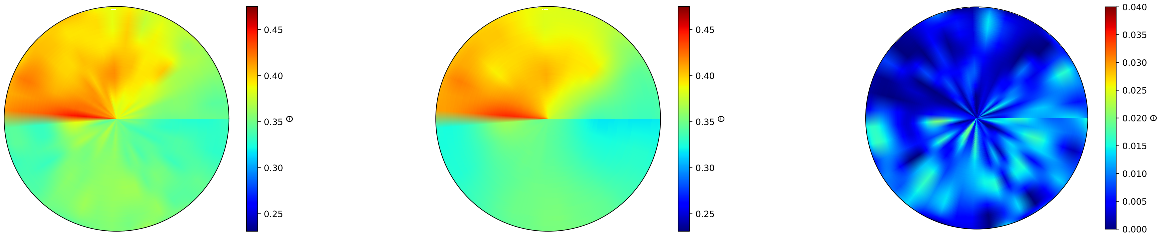

(a) Actual map. (b) Estimated map. (c) Absolute error map.

Figure 3.67: Surface moisture content maps at 02:00 HRS on Day 6 for the parameter uncertain case of Scenario 4.

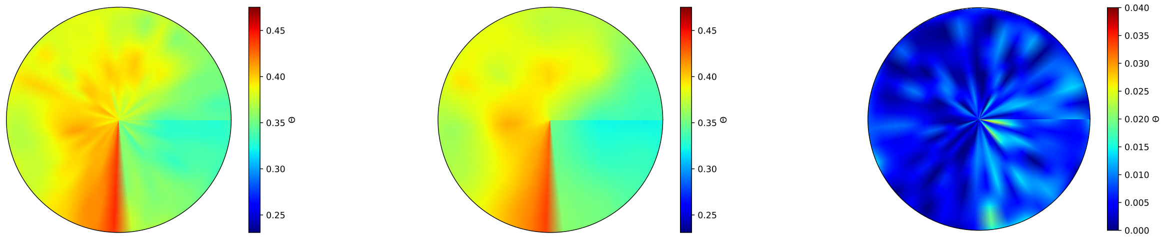

(a) Actual map. (b) Estimated map. (c) Absolute error map.

Figure 3.68: Surface moisture content maps at 03:00 HRS on Day 9 for the parameter uncertain case of Scenario 4.

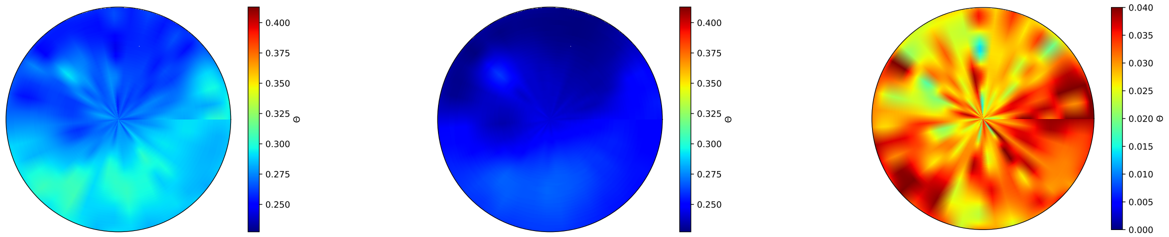

(a) Actual map. (b) Estimated map. (c) Absolute error map.

Figure 3.69: Maps at a depth of 0.3 m on Day 3 at 02:00 HRS for the parameter uncertain case of Scenario 4.

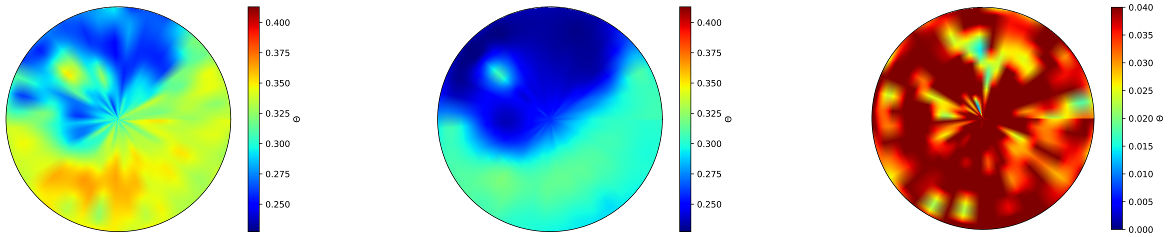

(a) Actual map. (b) Estimated map. (c) Absolute error map.

Figure 3.70: Maps at a depth of 0.3 m on Day 6 at 02:00 HRS for the parameter uncertain case of Scenario 4.

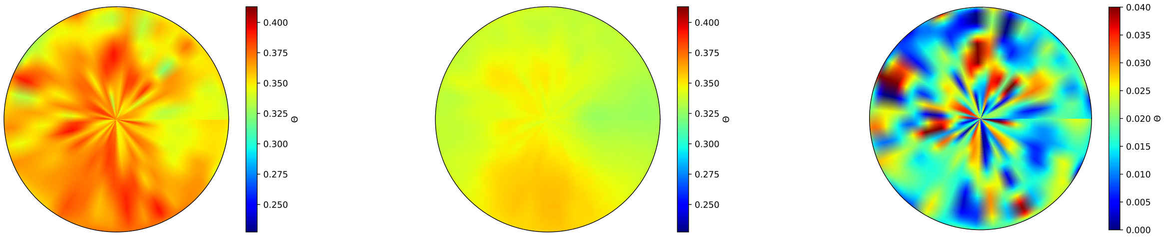

(a) Actual map.
(b) Estimated map.
(c) Absolute error map.

Figure 3.71: Maps at a depth of 0.3 m on Day 9 at 03:00 HRS for the parameter uncertain case of Scenario 4.

The estimates of the states located on the surface, even though they eventually converge, take a longer time to converge when parameter uncertainty is introduced. There is a noticeable discrepancy between the actual map and the estimated map for the surface on the 3rd day. This difference however decreases as the simulation advances and on the 6th and 9th days, the estimated maps (Figures 3.67(b) and 3.68(b)) for the surface closely resemble the actual maps (Figures 3.67(a) and 3.68(a)). For the bottom maps, the absolute error map (Figure 3.70(c)) on Day 6 still depicts appreciable absolute error values at most locations. On Day 9, the absolute error map (Figure 3.71(c)) however reveals relatively lower values, even though most locations still possess appreciable absolute error values. Thus, there exists a significant discrepancy between the estimated map (Figure 3.71(b)) and the actual map (Figure 3.71(a)) on the final day of the simulation.

3.5 Summary

In this chapter, the performance of the EKF and hence the effectiveness of the proposed information fusion system has been studied under 4 different scenarios. First, the cylindrical coordinates form of the Richards equation was derived and the finite difference model of the resulting PDE was developed. A case study that mimics microwave sensors mounted on center pivots was also described. From the simulation results, in the presence of accurate knowledge of soil parameters, the EKF exhibits good state estimation performance. The moisture content maps generated with the EKF estimates closely mirrored the moisture content maps constructed with the actual process states. In the presence of parameter uncertainty, the performance of the EKF declined, especially for states located far away from the surface. From the simulations, it was observed that the decline in the EKF performance was more pronounced when the soil type in the investigated field is nonuniform. It is worth mentioning that even though the performance of the EKF declined in the presence of parameter uncertainty, the EKF estimates and hence the resulting moisture content maps are within reasonable error bounds from the true process states.

Chapter 4

Soil Moisture Map Construction - A Real Case Study

In this chapter, we demonstrate the effectiveness, consistency, and accuracy of the proposed information fusion system by considering microwave remote sensor measurements obtained from a field equipped with a center pivot irrigation system. Essentially, the modeling and estimation methods described in Chapter 3 are used in this chapter. In Section 4.1, a description of the study area is provided. A series of data preprocessing steps, which result in a suitable data representation for the state estimator are enumerated and discussed in detail in Section 4.2. In Section 4.3, the criteria for evaluating the performance of the state estimation and hence the information fusion system are mentioned and discussed. Section 4.4 describes how the measurements are mapped to the nodes in the field model. Section 4.5 shows the results of the investigation. Section 4.6 provides a summary of the work covered in this chapter.

4.1 Field Description

The Alberta Irrigation Center is located east of the City of Lethbridge, Alberta, Canada, with an approximate area of 0.81 km^2. The main soil texture is clayey loam with few lenses of sand within the soil profile. The layout of the center is shown in Figure 4.1.

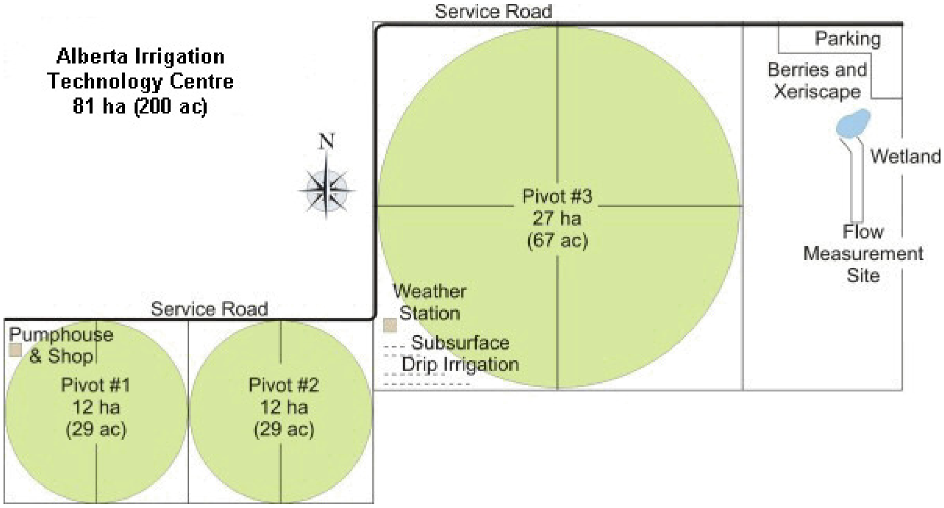

Figure 4.1: Layout of the Alberta Irrigation Center.
Available at: http://www.demofarm.ca/layout.htm (Accessed on 20 May 2020).

The field under study is the one covered by Pivot #3. The Lethbridge Demo Farm Irrigation Management Climate Information Network (IMCIN) provides meteorological parameters such as temperature, incoming solar radiation, and wind. Real-time data from this weather station can be obtained from the Alberta Climate Information Service (ACIS) website (https://agriculture.alberta.ca/acis/).

4.2 Microwave Data Preprocessing

The raw measurements obtained from the sensors at the end of the center pivot's rotation cycle are interpolated using an appropriate technique in order to obtain unknown moisture content values in unmeasured locations such as areas between the sensor tracks. The resulting interpolated data set is considered in this investigation. This data set depicts the GPS coordinates, which represent the location of the measurement on the investigated field, and the time at which each measurement was obtained. Table 4.1 shows a section of the interpolated data obtained on 21st June, 2019 and Figure 4.2 shows the map of the GPS coordinates of all the measurements obtained on that day.

Table 4.1: A snapshot of the interpolated microwave data obtained on 21st June, 2019.

Time	**GPS Coordinates**	**Volumetric Water Content**
2019-06-20-11:16:52	(49.6879953, -112.7430468)	0.371
2019-06-20-11:21:57	(49.6880852, -112.7437415)	0.266
2019-06-19-00:16:46	(49.6871862, -112.7374888)	0.436
2019-06-19-01:01:58	(49.6876357, -112.7374888)	0.476
2019-06-21-07:14:39	(49.6873660, -112.7380446)	0.142
2019-06-21-07:22:43	(49.6873660, -112.7381836)	0.117

Figure 4.2: GPS coordinates map of all measurements obtained on 21st June, 2019.

The interpolated data set goes through a series of preprocessing steps in order to obtain data that can be used in the state estimation algorithm. Next, the preprocessing steps employed in this work are enumerated and explained.

4.2.1 Discarding Measurements beyond the Circular Track

It is considered that only measurements on and within the circular track of the center pivot are useful measurements. Consequently, all measurements whose locations fall beyond the circular track are identified and excluded. In order to identify the measurements to be excluded, we employ the following steps:

- Obtain the GPS coordinates of the center of the field, G_c, and the radius of the field,

H_r (m).

- For any measurement with GPS coordinates, G_i, compute the distance, $d_{c,i}$, between G_c and G_i.
- If $d_{c,i} \in [0, H_r]$, keep the measurement with GPS coordinates G_i.
- Else discard the measurement associated with GPS coordinates G_i.

We illustrate this preprocessing step with the interpolated data set obtained on 21st June 2019. Figure 4.3(a) shows the measurements with GPS coordinates that are on and within the circular track of the pivot and Figure 4.3(b) shows the measurements that lie beyond the track. All measurements illustrated in Figure 4.3(b) are discarded.

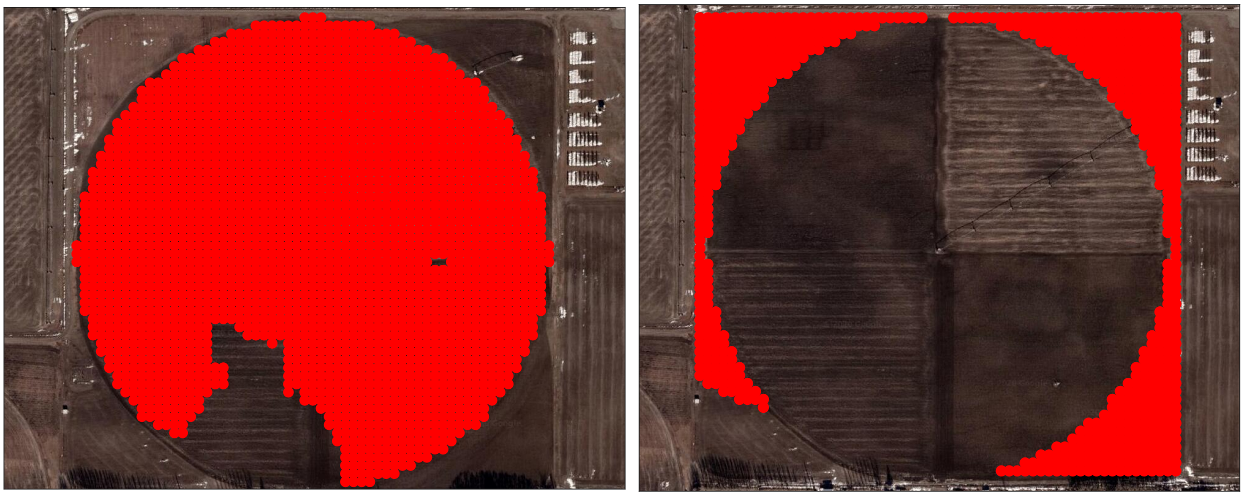

(a) Points on and within the circular track.

(b) Points beyond the circular track.

Figure 4.3: Sorting measurements according to points within and beyond the circular track of the pivot.

4.2.2 Sorting Measurements by Date and Time

As has already been mentioned, the volumetric moisture measurements obtained from the microwave sensors at the end of one rotation cycle comprise of measurements obtained at different times of one or a few days within the cycle. From Table 4.1, it can be seen that the data obtained on the 21st of June consists of measurements obtained on the 19th, 20th and 21st of June, 2019.

After excluding the measurements that fall beyond the circular track of the pivot, the retained data is sorted by date. Measurements obtained on a specific day are further sorted by time in ascending order. The measurements are shown in Figure 4.3(a) were obtained from three consecutive days. The separation of measurements according to date is shown in Figure 4.4.


(a) Measurements obtained on June 19th.

(b) Measurements obtained on June 20th.

(c) Measurements obtained on June 21st.

Figure 4.4: Sorting measurements by dates.

4.2.3 Sorting Measurements by Quadrants

For a large field, like the one considered in this chapter, the field model will be made up of a high number of nodes (states). Solving such a model numerically is computationally expensive. To make the model computationally tractable, we propose the division of the field model into four submodels, with each submodel representing one of the four quadrants of the entire field. Each submodel will then be used to obtain the volumetric moisture content estimates and hence the moisture content map of its respective quadrant. The maps obtained from each submodel can then be combined to obtain a single map for the entire field. Dividing the field model into four submodels also requires that measurements obtained on a particular day are sorted by the quadrants in which they are located. Figure 4.5 shows the four quadrants of the investigated field.

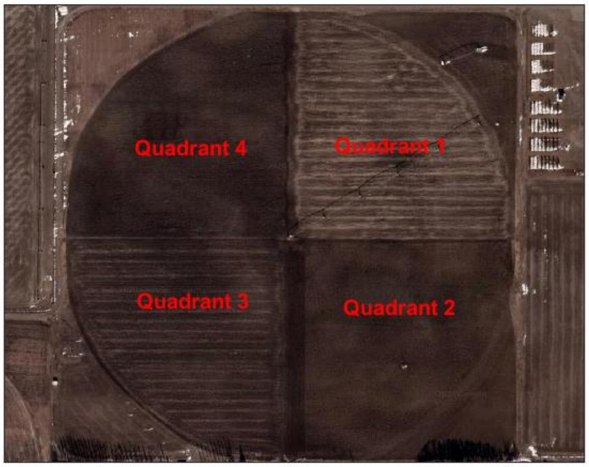

Figure 4.5: Quadrant description of the investigated field.

The following steps are employed to sort the measurements by the quadrants in which they are located.

- Obtain the GPS coordinates, G_c, of the center of the field.
- Given the GPS coordinates of any measurement, G_i, compute the bearing $B_{c,i}$ between G_c and G_i.
- If $B_{c,i} \in [0, 90)$, assign the measurement corresponding to G_i to Quadrant 1.
- Else if $B_{c,i} \in [90, 180)$, assign the measurement corresponding to G_i to Quadrant 2.
- Else if $B_{c,i} \in [180, 270)$, assign the measurement corresponding to G_i to Quadrant 3.
- Else assign the measurement corresponding to G_i to Quadrant 4.

Using these steps, we sort the measurements obtained on the 20th of June shown in Figure 4.4(b), by their respective quadrants and the results are shown in Figure 4.6.

(a) Measurements located in Quadrant 1.

(b) Measurements located in Quadrant 2.

(c) Measurements located in Quadrant 3.

(d) Measurements located in Quadrant 4.

Figure 4.6: Sorting measurements obtained on June 20th by their respective quadrants.

4.2.4 Center Pivot Movement Detection

Since the microwave sensors measure the soil moisture of the field as the center pivot rotates, the movement of the center pivot can be inferred from how the measurement locations change with time in each of the four quadrants. The idea is to group the measurements in each quadrant according to a specific sampling time, T_s, such that the change in measurement locations with time models the anticlockwise movement of the center pivot. In this work, it was observed that when $T_s = 32$ minutes, the measurements, Y_θ, model the movement of the center pivot. The detailed steps of how the measurements are grouped according to T_s are outlined below:

1. Arrange measurements in ascending order of time to obtain an array of soil moisture

measurements, $Y = \{y_1, ..., y_N\}$ and its corresponding time array, $T = \{T_1, ..., T_N\}$, where N is the total number of measurements in the quadrant.

2. Obtain $T_{\text{current}} \coloneqq T_1 + T_s$ and define $Y_{T_s} = [\ \ ]_{M,1}$ where Y_{T_s} is an array which contains M measurements obtained T_s minutes after T_1.
3. If $T_i \leq T_c$, where $i = 1, .., N$, append the corresponding measurement, y_i, to Y_{T_s}.
4. Delete $T_1, ..., T_M$, and $y_1, ..., y_M$ from T and Y respectively to obtain $T = \{T_{M+1}, ..., T_N\}$ and $Y = \{y_{M+1}, ..., y_N\}$.
5. Update $T_{\text{new}} = T_{\text{current}} + T_s$ and define $Y_{2T_s} = [\ \ ]_{M_1,1}$ where Y_{2T_s} is an array which contains M_1 measurements obtained T_s minutes after T_{current}.
6. If $T_i \leq T_{\text{new}}$, where $i = M + 1, .., N$, append the corresponding measurement, y_i, to Y_{2T_s}.
7. Delete $T_{M+1}, ..., T_{M_1}$, and $y_{M+1}, ..., y_{M_1}$ from T and Y respectively to obtain $T = \{T_{M_1+1}, ..., T_N\}$ and $Y = \{y_{M_1+1}, ..., y_N\}$.
8. Steps 4, 5, 7 and 8 are repeated until $Y = \{\ \}$ and $T = \{\ \}$.
9. Finally we obtain measurement arrays $Y_{T_s}, Y_{2T_s}, ..., Y_{kT_s}$ which contain the measurements obtained after $T_s, 2T_s, ..., kT_s$ from T_1. respectively. k is the least positive integer such that $T_N \leq kT_s$.

We use the measurements located in Quadrant 4 on the June 20th, shown in Figure 4.6(d), to illustrate the steps outlined in this preprocessing stage. For measurements in this quadrant, it was observed that when $k = 17$, $Y = \{\ \}$. Thus we obtain measurement arrays $Y_{T_s}, Y_{2T_s}, ..., Y_{17T_s}$. The GPS coordinates associated with the measurements in each of the arrays are mapped to the investigated quadrant to obtain Figures 4.7(a) to 4.7(q). From these plots, we observe that as time proceeds from T_s to $17T_s$, the change in the measurement locations models the anticlockwise movement of the center pivot.

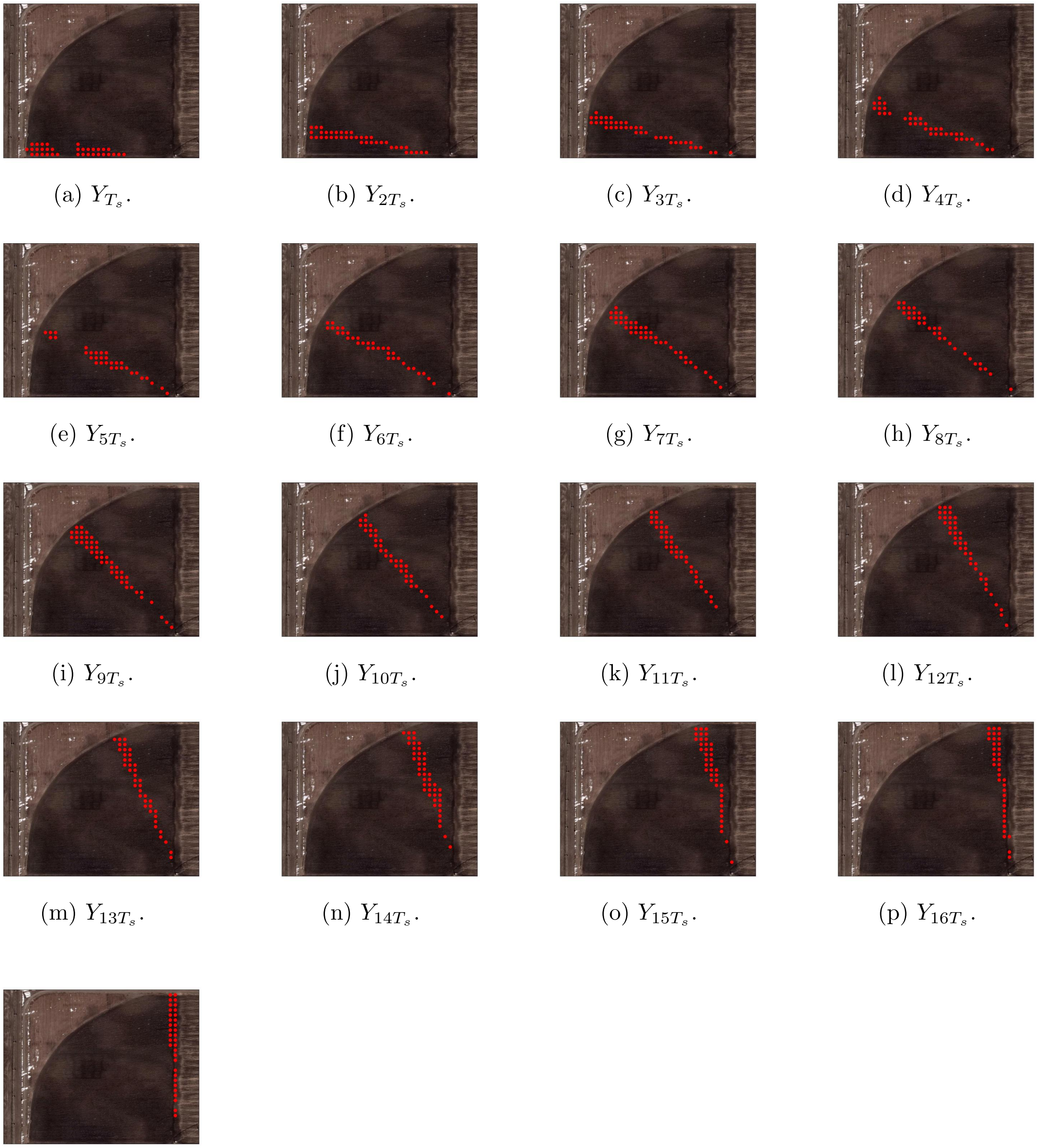

(a) Y_{T_s}.

(b) Y_{2T_s}.

(c) Y_{3T_s}.

(d) Y_{4T_s}.

(e) Y_{5T_s}.

(f) Y_{6T_s}.

(g) Y_{7T_s}.

(h) Y_{8T_s}.

(i) Y_{9T_s}.

(j) Y_{10T_s}.

(k) Y_{11T_s}.

(l) Y_{12T_s}.

(m) Y_{13T_s}.

(n) Y_{14T_s}.

(o) Y_{15T_s}.

(p) Y_{16T_s}.

(q) Y_{17T_s}.

Figure 4.7: Center pivot movement detection in Quadrant 4 on June 20th, 2019.

4.2.5 Outlier Detection

In this stage, suspicious volumetric moisture measurements are identified and excluded from the soil moisture measurement arrays. For a given soil type present in a quadrant, moisture measurements which are lower than the residual moisture content, θ_r, are discarded. Similarly, moisture measurements greater than the saturated moisture content, θ_s, are also discarded.

4.3 Evaluation Criteria

To evaluate the performance of the EKF and hence the information fusion system in providing consistent and accurate soil moisture estimates, the following evaluation methods are employed:

(1) Cross-validation.

(2) The Normalized Innovation Squared (NIS) test.

(3) Evolution of the state covariance matrix's trace.

A detailed explanation of the aforementioned methods is provided in the sequel.

4.3.1 Cross-validation

Here, the measurements in each measurement array, Y_{aT_s}, where $a = 1, ..., k$, are divided in two sets: a training set, $Y_{aT_s,\text{train}}$ and a validation set, $Y_{aT_s,\text{valid}}$. $Y_{aT_s,\text{train}}$ is used in the update step of the EKF. Measurements in the validation are compared with their corresponding estimates provided by the EKF. A reasonable difference between the measurements in the validation set and the soil moisture estimates indicates that the EKF and hence the proposed information fusion system provides accurate soil moisture estimates.

4.3.2 Normalized Innovation Squared (NIS) Test

In practice, we cannot measure the performance of the EKF with respect to the state, in this case, the pressure head h (m), since we do not know its true value. We can however measure the performance of the EKF by comparing the predicted and true values of the measurements. The measurement residual, known as the **innovation** e_k, is defined as the difference between the actual measurement, y_k, and the best available prediction based on the system model and previous measurements, $\hat{y}_k$. Mathematically, e_k is defined as:

$$e_k = y_k - \hat{y}_k \tag{4.1}$$

$$\hat{y}_k = H(\hat{x}_{k|k-1}) \tag{4.2}$$

where $H(\cdot)$ is the output function and $\hat{x}_{k|k-1}$ is *a priori*. The covariance matrix, E_k of e_k is:

$$E_k = H_k P(k|k-1) H_k^T + R \tag{4.3}$$

where R is the measurement noise covariance matrix, $P(k|k-1)$ is the covariance matrix of the state $\hat{x}_{k|k-1}$ and $H_k = \frac{\partial H}{\partial x}|_{\hat{x}_{k|k-1}}$. The EKF is working properly if e_k is Gaussian, zero-mean, white (uncorrelated), and with covariance equal to E_k. To verify this, a statistical test term is defined in terms of E_k and e_k. This statistic is known as the normalized innovation squared (NIS) [47] and it is defined as:

$$\Omega^2_{d,k} = e_k^T E_k^{-1} e_k \tag{4.4}$$

A null hypothesis which supposes that the sample observations result purely from chance can be formulated as:

$$H_0 : E(e_k) = 0 \tag{4.5}$$

H_0 can be tested against the alternative hypothesis:

$$H_1 : E(e_k) \neq 0 \tag{4.6}$$

$\Omega^2_{d,k}$ follows a χ^2 distribution with the probability relationship:

$$P\{\Omega^2_{d,k} \leq \chi^2_{m,1-\alpha}|H_0\} = 1 - \alpha \tag{4.7}$$

where the subscript m, the degrees of freedom, corresponds to the number of observations at time instant k and α is the significance level.

If $\Omega^2_{d,k} < \chi^2_{m,1-\alpha}$, the null hypothesis can be accepted [48]. We can conclude that there is no significant discrepancy between the system estimate and the measurement model.

4.3.3 Evolution of the State Covariance Matrix's Trace

In the EKF, the presence of measurements reduces the uncertainty of the state estimates. The trace of the state covariance matrix P quantifies the uncertainty of the state estimates. As a means of testing the performance of the EKF, the trace of the state covariance matrix is monitored in the presence of measurements. A continuous decrease in the trace, in the presence of measurements, shows that the EKF is performing well.

4.4 Mapping Measurements to Nodes in the Field Model

Before the state estimation is performed, every measurement provided by the microwave sensors must be mapped to a corresponding node in the field model. To achieve this, the following detailed steps are employed.

1. For a particular quadrant, we generate GPS coordinates whose arrangement is similar to the arrangement of nodes in the field model.

2. For an incoming measurement from the sensors, the distances between its GPS coordinates and all the generated coordinates are computed.

3. The measurement is assigned to the node which has the least distance from the incoming measurement location.

4.5 Results and Discussion

In this section, we provide results to demonstrate the effectiveness of the proposed approach. Firstly, we describe the case study from which the results are based on. Then we demonstrate that the proposed approach has the ability to provide soil moisture estimates in the form of frequently updated soil water content maps. The results of the predictive capability of the proposed approach are also shown. Finally, we provide results of the earlier outlined performance evaluation criteria.

4.5.1 System Description

In order to adapt the Equation (3.17) to a sector of the circular track, two extra boundary conditions are imposed in the θ-direction, and the boundary condition expressed by Equation (3.24) is omitted. Specifically, the zero-gradient boundary condition is imposed at the boundaries of the sector in the θ-direction.

$$\frac{1}{r}\frac{\partial h(r,\theta,z,t)}{\partial \theta} = 0 \qquad at \quad (r, \theta = 1.5\pi, z) \tag{4.8}$$

$$\frac{1}{r}\frac{\partial h(r,\theta,z,t)}{\partial \theta} = 0 \qquad at \quad (r, \theta = 2\pi, z) \tag{4.9}$$

where the coordinates $(r, \theta = 1.5\pi, z)$ describe the nodes along the starting location of the center pivot and the coordinates $(r, \theta = 2\pi, z)$ represent the nodes along the final location of the pivot after an angular rotation of θ_{sector}.

Quadrant 4 is chosen for the numerical investigation. We point out that although the proposed approach targets the entire field, only one quadrant is chosen for the sake of simplicity and with no loss of generality. Indeed, the current approach can be applied to the remaining quadrants by considering the field conditions and the microwave measurements obtained in those quadrants.

Quadrant 4 has a radius (H_r) of 290 m and the center pivot describes a total angle (H_θ) of 0.5π radians in order to fully traverse it. The depth of soil (H_z) investigated is 0.6 m. H_r and H_θ are equally divided into 30 and 17 equally spaced compartments respectively. H_z is divided into 10 unequally spaced compartments with a finer discretization near the soil surface and a coarsening discretization away from the soil surface. Correspondingly, the field submodel representing Quadrant 4 is discretized into a total of $5,100$ states (N_x) in the r, θ, and z directions with each state located at the center of its corresponding compartment. A schematic diagram of the investigate quadrant is shown in Figure 4.8.

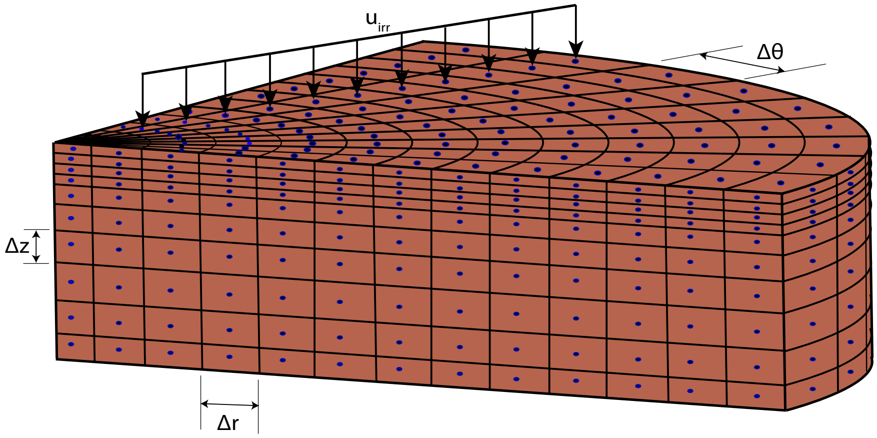

Figure 4.8: A schematic diagram of the investigated quadrant.

Measurements provided by the microwave sensors between the period of June 20th, 2019 to August 27th, 2019 are considered. Barley was cultivated on the chosen quadrant during the period under investigation. Consequently, crop coefficient values of barley between 0.6 and 1.5 are used. The irrigation applied during the period is shown in Figure 4.9(b). The soil hydraulic parameters of clay loam, the soil type in the investigated quadrant, and the initial guess of the state are shown in Table 4.2. Weather information in the form of reference evapotranspiration for the period under investigation was obtained from the ACIS website and the observed values are shown in Figure 4.9(a).

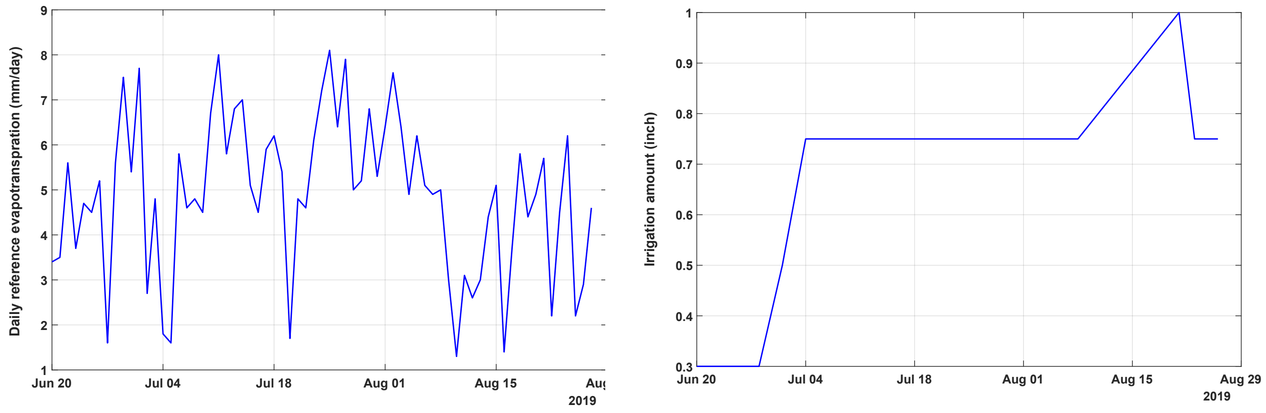

(a) Daily reference evapotranspiration.

(b) Irrigation amount applied.

Figure 4.9: Observed weather conditions and applied irrigation between June 20th - August 27th, 2019.

Table 4.2: The initial condition and parameters of clay loam soil.

	$\hat{x}_0$ (m)	K_s (m/s)	θ_s (m^3/m^3)	θ_r (m^3/m^3)	α (1/m)	n (-)
Clay Loam	-0.5	7.222×10^{-7}	0.420	0.095	1.90	1.31

4.5.2 Moisture Content Map Construction

In this section, we demonstrate the ability of the proposed approach to provide frequently updated soil water content maps. We also demonstrate that our approach can provide soil water maps at greater depths below the soil surface, hence the root zone, knowledge of which is needed for automated irrigation management. The predictive capability of our approach, in cases where the center pivot is stationary, is also demonstrated.

4.5.2.1 Frequently Updated Moisture Content Maps

We provide results that demonstrate the construction of frequently updated moisture content maps. We employ the near-surface maps obtained on June 20^{th}, 2019 from 11:47 am to 20:19 pm for the illustration. After every sampling time $T_s = 32$ minutes, within the simulation period, the microwave measurements are integrated with the field model and the EKF in the proposed information fusion system. The state estimates provided by the EKF are converted into volumetric moisture using Equation (3.11). The resulting volumetric moisture estimates are represented in moisture content maps. When new measurements are obtained, after every T_s minutes, the volumetric moisture estimates and hence the moisture content maps are updated. This process is repeated until all the measurements in the selected quadrant and on a particular day have been considered. The process of frequently updating the volumetric moisture estimates and hence the moisture content maps is illustrated in Figures 4.10(a) to 4.10(q).

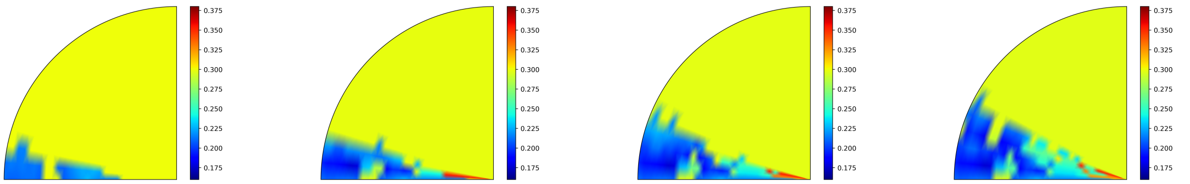

(a) Map at 11:47:57 am.
(b) Map at 12:19:57 pm.
(c) Map at 12:51:57 pm.
(d) Map at 13:23:57 pm.

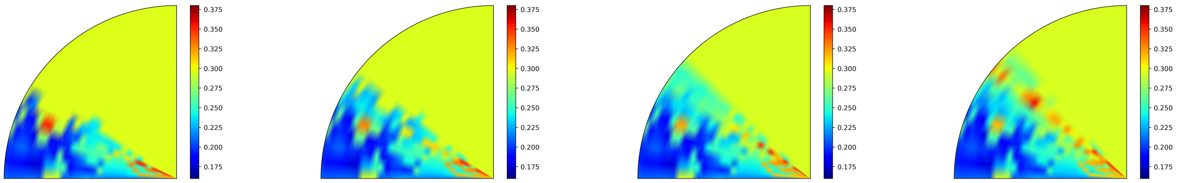

(e) Map at 13:55:57 pm.
(f) Map at 14:27:57 pm.
(g) Map at 14:59:57 pm.
(h) Map at 15:31:57 pm.

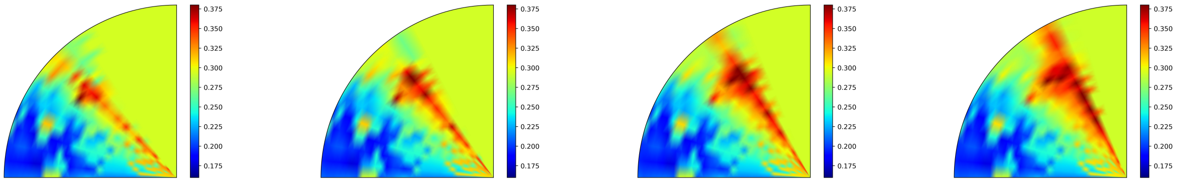

(i) Map at 16:03:57 pm.
(j) Map at 16:35:57 pm.
(k) Map at 17:07:57 pm.
(l) Map at 17:39:57 pm.

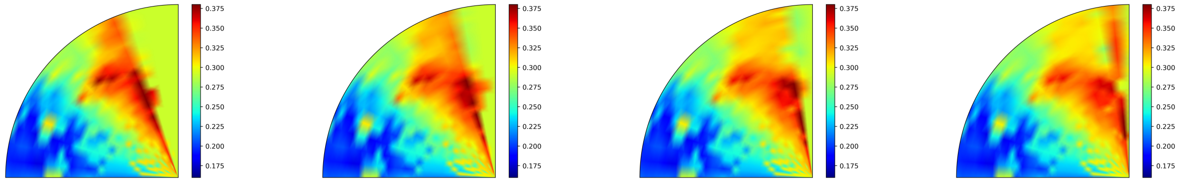

(m) Map at 18:11:57 pm. (n) Map at 18:43:57 pm. (o) Map at 19:15:57 pm. (p) Map at 19:47:57 pm.

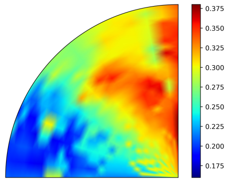

(q) Map at 20:19:57 pm.

Figure 4.10: Frequently updated moisture content maps from 11:47:57 am to 20:19:57 pm on June 20th, 2019.

4.5.2.2 Moisture Content Maps for Selected Days

We show moisture content maps generated on some selected days (July 6th, 2019, and August 27th, 2019) during the simulation period. Here, in addition to the near-surface maps, maps at greater depths below the soil surface are also shown. Figure 4.11(a) and Figure 4.12(a) respectively depict the near-surface maps after all the measurements on July 6th and August 27th were processed. On 6th July, the moisture map at the depth of 0.16 m from the soil surface is shown in Figure 4.11(b). The map at a depth of 0.42 m from the soil surface on the 27th of August is shown in Figure 4.12(b).

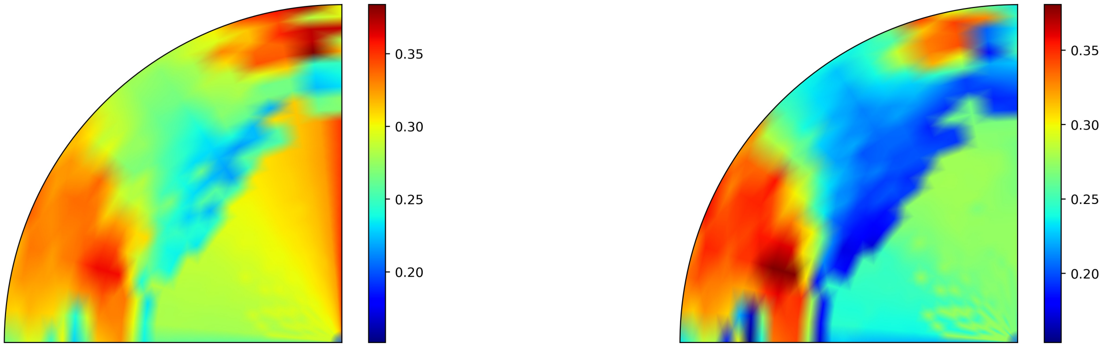

(a) Near-surface map.

(b) Map at depth = 0.16 m.

Figure 4.11: Moisture content maps on July 6th, 2019 at 21:55:57 pm.

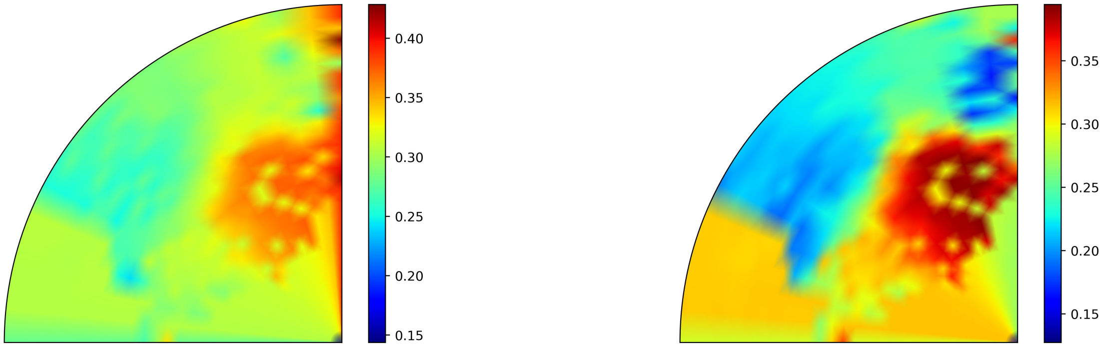

(a) Near-surface map.

(b) Map at depth = 0.42 m.

Figure 4.12: Moisture content maps on August 27th, 2019 at 15:31:57 pm.

4.5.2.3 Predictive Capability of the Proposed Approach

Figures 4.13 and 4.14 are examples of moisture content maps constructed on days within the simulation period where the center pivot was stationary. These maps were constructed using soil moisture predictions provided by the field model. Figure 4.13(a) shows the predicted near-surface soil water content on 25th June 2019 and Figure 4.13(b) shows the predicted soil water content at a depth of 0.60 m. Similarly, on the 18th of August, when the center pivot was stationary, the predicted near-surface soil moisture content is as shown in Figure 4.14(a). And Figure 4.14(b) provides a summary of the predicted soil water content at a depth of 0.16 m.

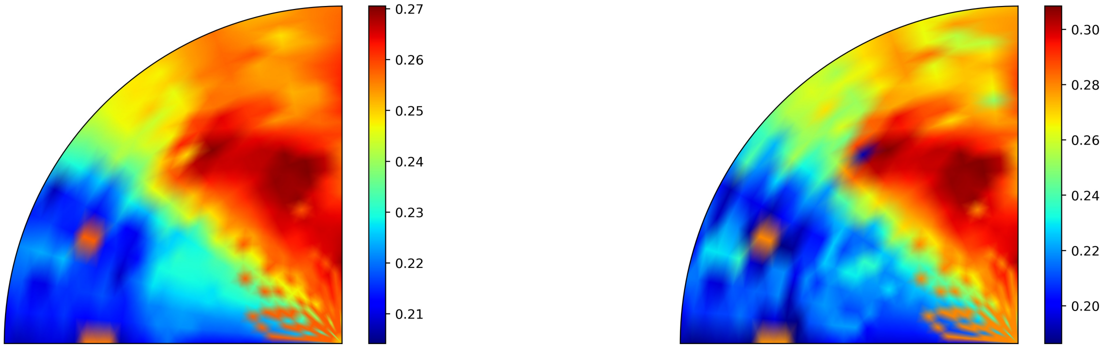

(a) Near-surface map.

(b) Map at depth = 0.6 m.

Figure 4.13: Moisture content maps (prediction) on June 25th at 9:40:57 am.

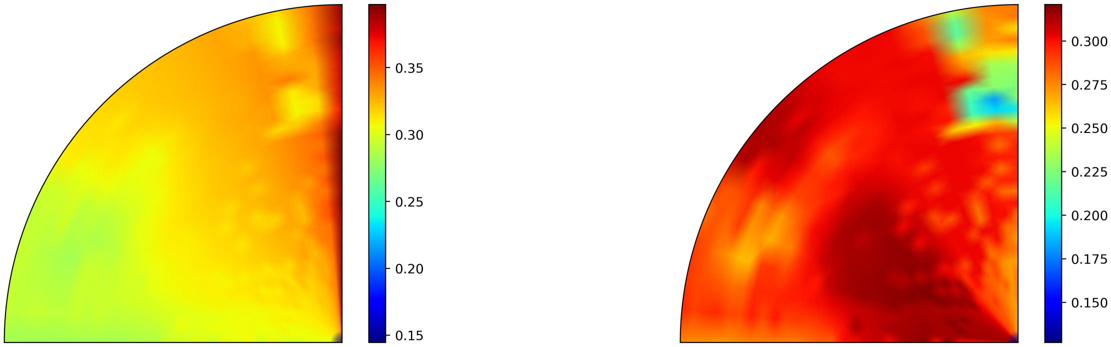

(a) Near-surface map.

(b) Map at depth = 0.16 m.

Figure 4.14: Moisture content maps (prediction) on August 18th at 23:59:57 pm.

4.5.3 Evaluation of the Proposed Approach

In this section, we evaluate the performance of the proposed approach using the three evaluation criteria that have been outlined.

4.5.3.1 Trace of the State Covariance Matrix

In Figure 4.15, the trajectory of the trace of the state covariance matrix for the simulation period is shown. For the sake of clarity, the overall trajectory is divided into three segments:

from June 20th to July 20th, from July 11th to July 31st and finally from August 1st to 27th. As is evident in all the subfigures of Figure 4.15, in the presence of microwave measurements, there is a decrease in the trace of the state covariance matrix. This observation is true for all the days on which the EKF updates were performed, illustrated with the red dash-dot segments in Figure 4.15.

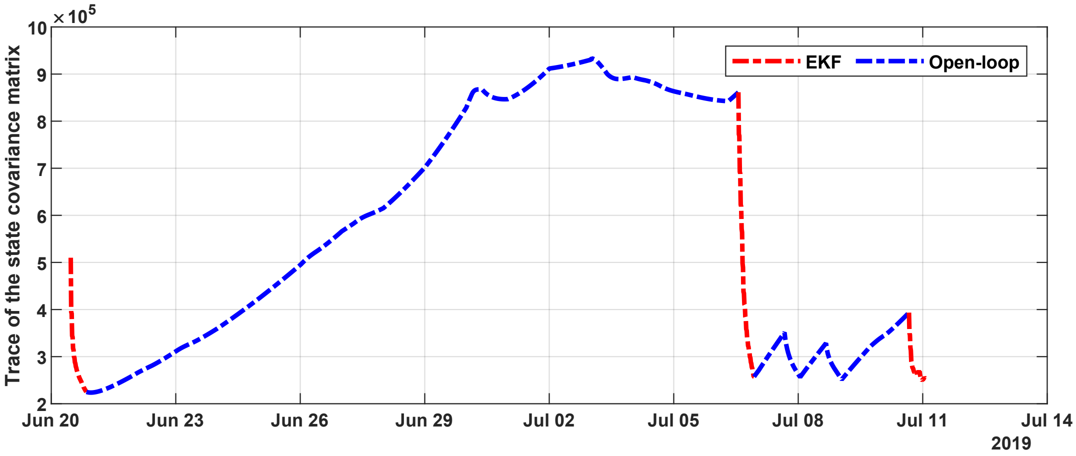

(a) Trajectory of the trace from June 20th to July 10th, 2019.

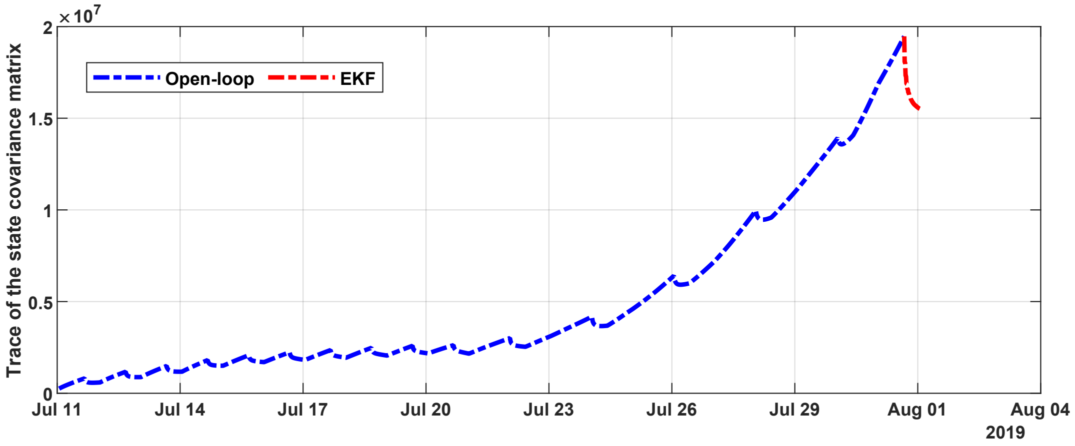

(b) Trajectory of the trace from July 11thto July 31st, 2019.

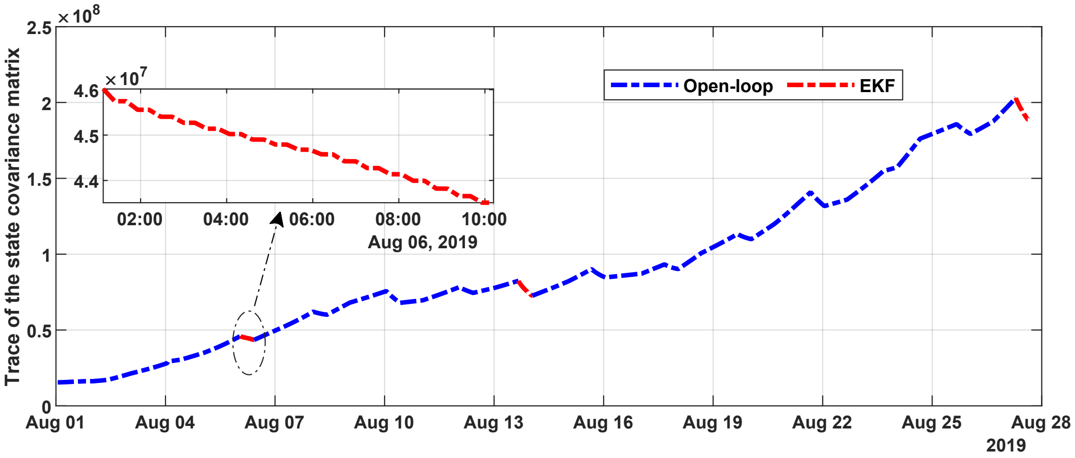

(c) Trajectory of the trace from August 11th to August 27th, 2019.

Figure 4.15: Trajectories of the trace of the state covariance matrix from June 20th to August 27th, 2019.

4.5.3.2 Results of the NIS test

Figure 4.16 shows the results of the NIS test for some selected days (June 20th, July 6th, July 10th, July 31st, August 6th and August 27th) performed at a 5% significance level. From the figure, it is evident that, at each time instant t_k, $\Omega^2_{d,k}$ (blue hexagon) is less than $\chi^2_{m,1-0.05}$ (red dots). We can therefore accept the null hypothesis that the sample observations result purely from chance and thus conclude that there is no significant discrepancy between the state estimates provided by the proposed solution and the measurements obtained from the microwave sensors.

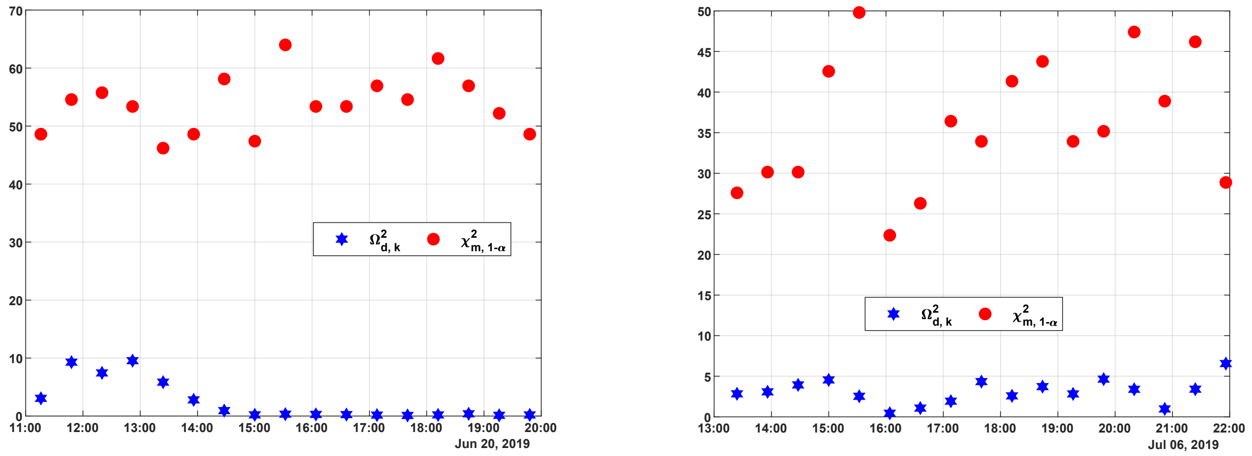

(a) NIS test - June 20th, 2019.

(b) NIS test - July 6th, 2019.

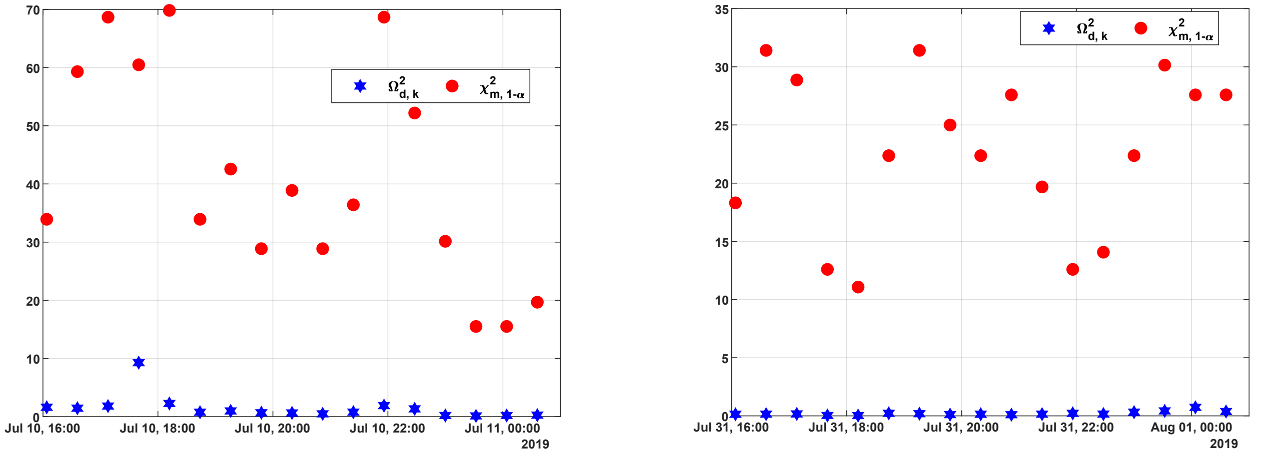

(c) NIS test - July 10th, 2019.

(d) NIS test - July 31st, 2019.

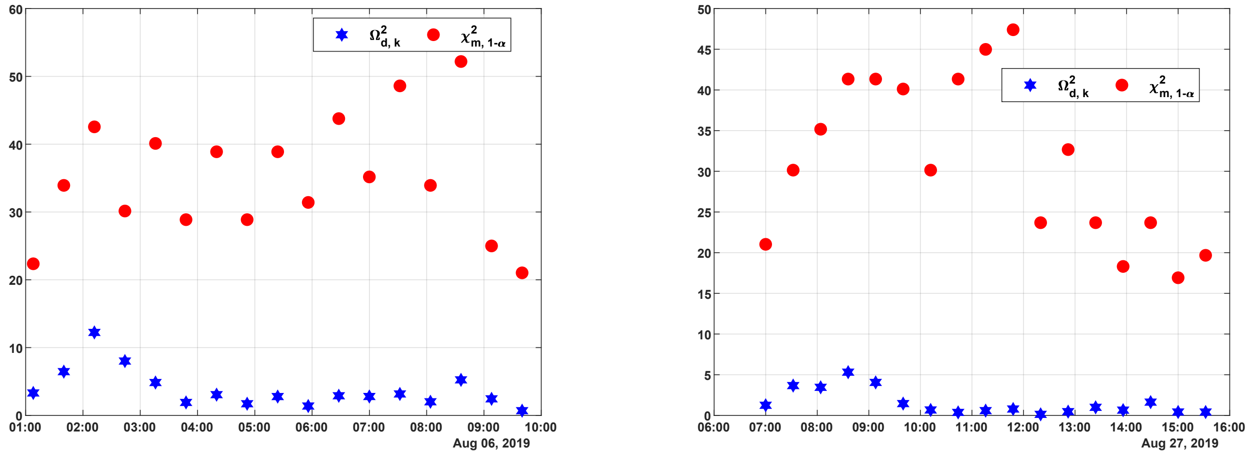

(e) NIS test - August 6th, 2019.

(f) NIS test - August 27th, 2019.

Figure 4.16: Results of the NIS test from June 20th to August 27th, 2019.

4.5.3.3 Results of the Cross-validation

Figure 4.17 and Figure 4.18 show the results of the cross-validation. Two kinds of cross-validation were performed.

In the first kind, shown in Figure 4.17, the cross-validation is performed on a fraction (validation set) of the total preprocessed measurements obtained on the day under consideration. In this approach, we randomly split the total measurements into a training set and a validation set, in a ratio of 80% to 20%. From Figures 4.17(a), 4.17(b), 4.17(c) and 4.17(d), it is observed that the approximate average absolute error between the actual observations and their corresponding estimates is 0.049, 0.0379, 0.0397 and 0.0273 for July 10th, July 31st, August 6th and August 27th respectively. The soil moisture estimates were able to capture the trend in the measurements present in the validation set. Consequently, it can be concluded that the EKF estimates are within negligible and practical error bounds from the true measurements.

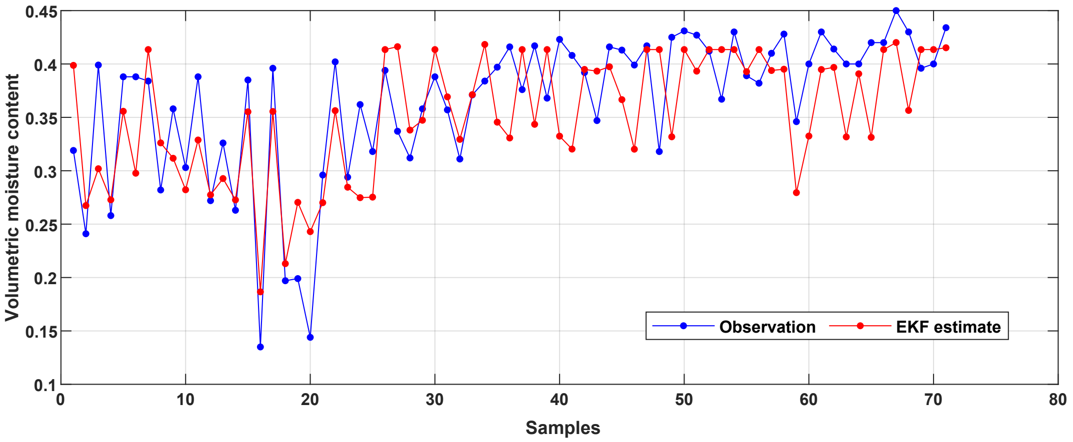

(a) Cross-validation results - July 10th, 2019.

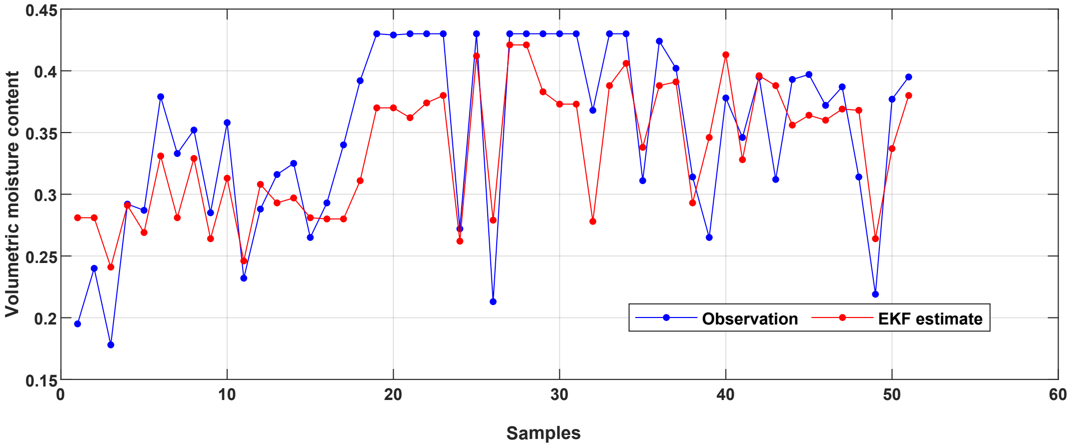

(b) Cross-validation results - July 31st, 2019.

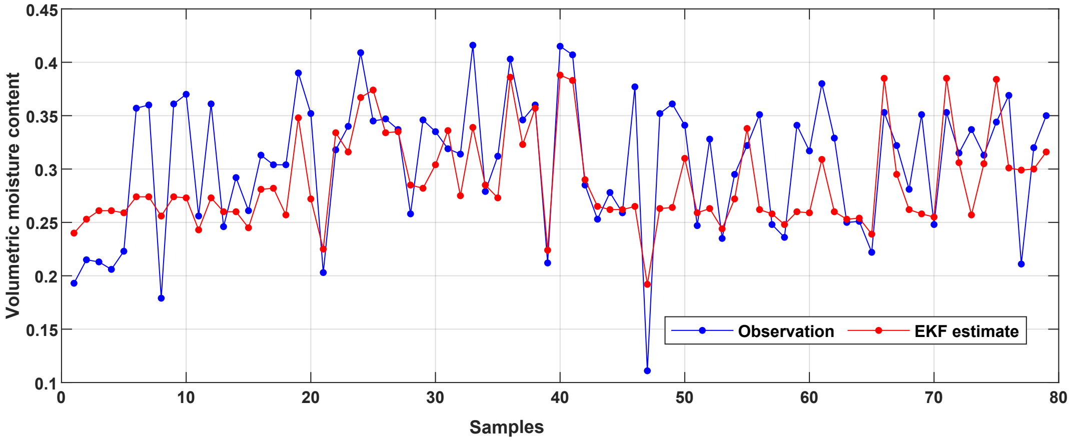

(c) Cross-validation results - August 6th, 2019.

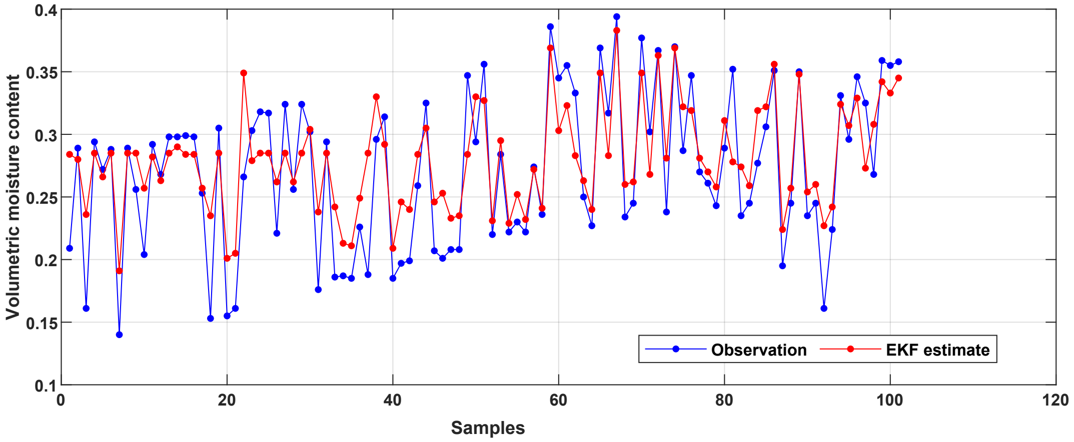

(d) Cross-validation results - August 27th, 2019.

Figure 4.17: Results of the cross-validation performed for some selected days.

In the second kind, the cross-validation is performed on all the preprocessed measurements obtained on the 13^{th} of August. This was done by simulating the field model, taking into consideration the applied irrigation and the prevailing weather conditions observed on the 13^{th} of August. The soil moisture predictions resulting from the simulation, shown in Figure 4.18(b) is then compared with the actual measurements, shown in Figure 4.18(a). From the absolute error map, Figure 4.18(c), it is evident that the proposed information fusion system, after it has been run for a sufficiently long period, can provide soil moisture predictions that are within satisfactory error bounds from the actual measurements obtained from the microwave sensors. From the results of the cross-validation, we can conclude that the soil moisture predictions and estimates provided by the information fusion system are reliable and accurate.

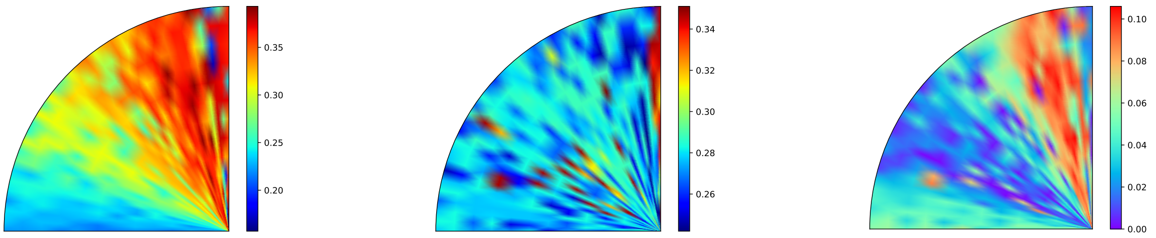

(a) Actual Map. (b) Predicted Map. (c) Absolute Error Map.

Figure 4.18: Validation results using all the measurements obtained on August 13^{th}, 2019.

4.6 Summary

In this chapter, microwave sensor measurements have been used to investigate the performance of the EKF and hence the proposed information fusion system. A description of the study was first provided. A series of data preprocessing steps, which resulted in a suitable data representation for the state estimator were enumerated and discussed in detail. The three methods which were employed to evaluate the performance of the EKF were discussed in detail. The chapter then proceeded with a description of the investigated field. The numerical investigation was then carried out using preprocessed measurements obtained from

June 20th to August 27th. Results were shown to demonstrate the construction of frequently updated moisture content maps and the predictive capability of the proposed approach. Maps illustrating the soil moisture information at greater depths below the soil surface were provided as well. Finally, the chapter concluded with the results of the performance evaluation.

In summary, the EKF and hence the proposed information fusion system demonstrated a good performance when real microwave sensor measurements were considered.

Chapter 5

Conclusions and Future Work

5.1 Conclusions

This thesis sought to improve the usability of soil moisture measurements obtained from microwave sensors mounted on center pivots in automated irrigation management. A process system engineering approach was used to find solutions to the current challenges facing the microwave remote sensing approach. Specifically, an information fusion system that assimilates microwave sensor measurements into a suitable agro-hydrological using the EKF was proposed to deal with the challenges. The information fusion system provided estimates and predictions of soil moisture in the form of moisture content maps.

Chapter 3 of this thesis developed an agro-hydrological model, the cylindrical coordinate version of the Richards equation, which is suitable for describing agro-hydrological systems equipped with center pivot irrigation systems. The finite difference model of the resulting equation was consequently developed. The proposed information fusion system was then studied and evaluated with simulated microwave sensor measurements under the following scenarios: (i) uniform initial conditions and uniform soil parameters; (ii) nonuniform initial conditions and uniform soil parameters; (iii) uniform initial conditions and two layers of soil in the investigated field and (iv) uniform initial conditions and a unique set of soil parameters at each node in the investigated field. Each scenario consisted of two cases: a normal case and a parameter uncertain case. In the normal case, the true soil parameters, which are the soil parameters that were used for the model simulation, were used in the EKF whereas, in the parameter uncertain case, a 5% offset was introduced into the soil parameters which were used in the EKF. The simulation results demonstrated the ability of the soil moisture estimates to track the actual soil moisture values under all the investigated scenarios. A strong agreement between the estimated moisture content maps and the actual moisture content maps was also evident from the simulation results. The parameter uncertain cases revealed that the accuracy and convergence speed of the soil moisture estimates was strongly dependent on the use of accurate soil hydraulic parameters in the EKF. That said, under parameter uncertainty, the information fusion system was able to provide soil moisture estimates which were within reasonable error bounds from the actual soil moisture values. The simulation results also revealed that the decline in the accuracy of the soil moisture estimates under parameter uncertainty was more significant when the investigated field was made up of different soil layers/types.

Soil moisture measurements of a field at the Alberta Irrigation Center, Lethbridge, obtained from passive microwave sensors mounted on a center pivot was used as the observations in Chapter 4 of this thesis. Frequently updated moisture content maps were constructed to demonstrate the ability of the information fusion system to eliminate the time delay associated with the current microwave remote sensing approach. Moisture content maps depicting soil moisture predictions were also obtained from the field model when the center pivot was stationary. It was also found that the information fusion system provided soil moisture estimates and predictions and thus moisture content maps at greater depths below the soil surface. Three evaluation criteria were used to study the performance of the information fusion system in Chapter 4. From the results of the performance evaluation, it was evident that when measurements were available from the microwave sensors, there was a continuous reduction in the uncertainty of the soil moisture estimates. It was also found out that, there was no significant discrepancy between the systems estimates and the measurement model. Cross-validation performed on the information fusion system revealed that the soil moisture estimates were within reasonable error bounds from the observed data in the validation set. In summary, it can be concluded from this chapter that the soil moisture estimates are consistent and accurate when the information fusion system considers observations from a real case study.

5.2 Future Work

- *Parameter estimation using observed data from microwave sensors mounted on center pivots.* The parameters of soil hydraulic functions are essential to the accurate estimation and prediction of soil moisture based on the Richards equation. This fact was confirmed by the simulation results in the parameter uncertain case of this work. Thus it will be of vital importance to include a parameter estimator in the information fusion system to improve its performance.

- *Constructing management zones based on soil moisture and parameter estimates for Variable rate irrigation (VRI) implementation.* As a further step towards the mitigation of the global water supply crisis, VRI technologies can be implemented. VRI allows easy application of varying rates of irrigation water based on individual management zones within a field. Management zones are areas on a field possessing homogeneous features for landscape, soil properties, and soil water requirements. In the future work, management zones can be constructed based on soil moisture and parameter estimates and a control system can then be designed for center pivots which will allow the pivot to supply the right amount of water to the individual management zones.

Bibliography

[1] A. Srivastava. Technology assisted knowledge agriculture for sustainable development goals. *Advances in Crop Science and Technology*, 6(5):1–8, 2018.

[2] Global multidimensional poverty index (MPI) 2017/2018 — OPHI. Website accessed on May 20, 2020.

[3] J. S. Wallace. Increasing agricultural water use efficiency to meet future food production. *Agriculture, Ecosystems and Environment*, 82(1-3):105–119, 2000.

[4] Global demand for food is rising. Can we meet it?. Website accessed on May 24, 2020.

[5] D. Wichelns and J. D. Oster. Sustainable irrigation is necessary and achievable, but direct costs and environmental impacts can be substantial. *Agricultural Water Management*, 86(1-2):114–127, 2006.

[6] FAO (2016) AQUASTAT Main Database, Food and Agriculture Organization of the United Nations (FAO) .Website accessed on Apr. 05, 2020.

[7] Water in a changing world: the United Nations world water development report 3 - UNESCO Digital Library. 2009.

[8] G. P. Petropoulos, G. Ireland, and B. Barrett. Surface soil moisture retrievals from remote sensing: Current status, products & future trends. *Physics and Chemistry of the Earth, Parts A/B/C*, 83:36–56, 2015.

[9] M. Gupta, P. K. Srivastava, and T. Islam. Integrative use of near-surface satellite soil moisture and precipitation for estimation of improved irrigation scheduling parameters. In *Satellite Soil Moisture Retrieval*, pages 271–288. Elsevier, 2016.

[10] Y. Shi, K. J. Davis, F. Zhang, C. J. Duffy, and X. Yu. Parameter estimation of a physically-based land surface hydrologic model using an ensemble Kalman filter: A multivariate real-data experiment. *Advances in water resources*, 83:421–427, 2015.

[11] W. W. Verstraeten, F. Veroustraete, and J. Feyen. Assessment of evapotranspiration and soil moisture content across different scales of observation. *Sensors*, 8(1):70–117, 2008.

[12] P. M. Huang, Y. Li, and M. E. Sumner. *Handbook of soil sciences: properties and processes*. CRC Press, 2011.

[13] D. A. Robinson, C. S. Campbell, J. W. Hopmans, B. K. Hornbuckle, S. B. Jones, R. Knight, F. Ogden, J. Selker, and O. Wendroth. Soil moisture measurement for ecological and hydrological watershed-scale observatories: A review. *Vadose Zone Journal*, 7(1):358–389, 2008.

[14] D. A. Robinson, S. B. Jones, J. M. Wraith, D. Or, and S. P. Friedman. A review of advances in dielectric and electrical conductivity measurement in soils using time domain reflectometry. *Vadose Zone Journal*, 2(4):444–475, 2003.

[15] T. J. Dean, J. P. Bell, and A. J. B. Baty. Soil moisture measurement by an improved capacitance technique, part i. sensor design and performance. *Journal of Hydrology*, 93(1-2):67–78, 1987.

[16] D. Moghadas and A. Badorreck. Machine learning to estimate soil moisture from geophysical measurements of electrical conductivity. *Near Surface Geophysics*, 17(2):181–195, 2019.

[17] H. Vereecken, J. A. Huisman, Y. Pachepsky, C. Montzka, J. Van Der Kruk, H. Bogena, L. Weihermüller, M. Herbst, G. Martinez, and J. Vanderborght. On the spatio-temporal dynamics of soil moisture at the field scale. *Journal of Hydrology*, 516:76–96, 2014.

[18] G. C. Topp, J. L. Davis, and A. P. Annan. Electromagnetic determination of soil water content: Measurements in coaxial transmission lines. *Water resources research*, 16(3):574–582, 1980.

[19] J. D. McNeill. Electromagnetic terrain conductivity measurement at low induction numbers. *Geonics Ltd., Technical Note*, 1980.

[20] M. D. Sherlock and J. J. McDonnell. A new tool for hillslope hydrologists: spatially distributed groundwater level and soilwater content measured using electromagnetic induction. *Hydrological Processes*, 17(10):1965–1977, 2003.

[21] Y. H. Kerr, P. Waldteufel, J.-P. Wigneron, J. M. Martinuzzi, J. Font, and M. Berger. Soil moisture retrieval from space: The soil moisture and ocean salinity (SMOS) mission. *IEEE transactions on Geoscience and remote sensing*, 39(8):1729–1735, 2001.

[22] B. D. Tapley, S. Bettadpur, J. C. Ries, P. F. Thompson, and M. M. Watkins. Grace measurements of mass variability in the Earth system. *Science*, 305(5683):503–505, 2004.

[23] M. T. Hallikainen, F. T. Ulaby, M. C. Dobson, M. A. El-Rayes, and L.-K. Wu. Microwave dielectric behavior of wet soil-part 1: Empirical models and experimental observations. *IEEE Transactions on Geoscience and Remote Sensing*, GE-23(1):25–34, 1985.

[24] T. Schmugge, P. Gloersen, T. Wilheit, and F. Geiger. Remote sensing of soil moisture with microwave radiometers. *Journal of Geophysical Research*, 79(2):317–323, 1974.

[25] T. J. Jackson. Estimation of surface soil moisture using microwave sensors. *Encyclopedia of Hydrological Sciences*, 2006.

[26] F. T. Ulaby, R. K. Moore, and A. K. Fung. *Microwave remote sensing: Active and passive*. Artech House microwave library. Artech House, 1981.

[27] E. G. Njoku and D. Entekhabi. Passive microwave remote sensing of soil moisture. *Journal of hydrology*, 184(1-2):101–129, 1996.

[28] J. P. Wigneron, L. Laguerre, and Y. H. Kerr. A simple parameterization of the L-band microwave emission from rough agricultural soils. *IEEE Transactions on Geoscience and Remote Sensing*, 39(8):1697–1707, 2001.

[29] M. Gupta and P. K. Srivastava. Integrating GIS and remote sensing for identification of groundwater potential zones in the hilly terrain of Pavagarh, Gujarat, India. *Water International*, 35(2):233–245, 2010.

[30] H. Lü, Z. Yu, Y. Zhu, S. Drake, Z. Hao, and E. A. Sudicky. Dual state-parameter estimation of root zone soil moisture by optimal parameter estimation and extended Kalman filter data assimilation. *Advances in water resources*, 34(3):395–406, 2011.

[31] J. M. Sabater, L. Jarlan, J.-C. Calvet, F. Bouyssel, and P. De Rosnay. From near-surface to root-zone soil moisture using different assimilation techniques. *Journal of Hydrometeorology*, 8(2):194–206, 2007.

[32] R. H. Reichle, D. B. McLaughlin, and D. Entekhabi. Hydrologic data assimilation with the ensemble Kalman filter. *Monthly Weather Review*, 130(1):103–114, 2002.

[33] H. Medina, N. Romano, and G. B. Chirico. Kalman filters for assimilating near-surface observations into the Richards equation – Part 2: A dual filter approach for simultaneous retrieval of states and parameters. *Hydrology and Earth System Sciences*, 18(7):2521–2541, 2014.

[34] H. Moradkhani, S. Sorooshian, H. V. Gupta, and P. R. Houser. Dual state–parameter

estimation of hydrological models using ensemble Kalman filter. *Advances in water resources*, 28(2):135–147, 2005.

[35] W. Chen, C. Huang, H. Shen, and X. Li. Comparison of ensemble-based state and parameter estimation methods for soil moisture data assimilation. *Advances in Water Resources*, 86:425–438, 2015.

[36] M. Pan, E. F. Wood, R. Wójcik, and M. F. McCabe. Estimation of regional terrestrial water cycle using multi-sensor remote sensing observations and data assimilation. *Remote Sensing of Environment*, 112(4):1282–1294, 2008.

[37] C. Montzka, H. Moradkhani, L. Weihermüller, H.-J. Hendricks Franssen, M. Canty, and H. Vereecken. Hydraulic parameter estimation by remotely-sensed top soil moisture observations with the particle filter. *Journal of hydrology*, 399(3-4):410–421, 2011.

[38] S. Bo, S. R. Sahoo, X. Yin, J. Liu, and S. L. Shah. Parameter and state estimation of one-dimensional infiltration processes: A simultaneous approach. *Mathematics*, 8(1):134, 2020.

[39] S. Bo and J. Liu. A decentralized framework for parameter and state estimation of infiltration processes. *Mathematics*, 8(5):681, 2020.

[40] L. A. Richards. Capillary conduction of liquids through porous mediums. *Physics*, 1(5):318–333, 1931.

[41] R. A. Feddes, P. J. Kowalik, and H. Zaradny. *Simulation of field water use and crop yield*. Centre for Agricultural Publishing and Documentation, Netherlands, 1982.

[42] C. Babajimopoulos, A. Budina, and D. Kalfountzos. SWBACROS: A model for the estimation of the water balance of a cropped soil. *Environmental Software*, 10(3):211–220, 1995.

[43] S. Al-Khafaf, P. J. Wierenga, and B. C. Williams. Evaporative flux from irrigated cotton as related to leaf area index, soil water, and evaporative demand. *Agronomy Journal*, 70(6):912–917, 1978.

[44] M. Th. van Genuchten. A Closed-form equation for predicting the hydraulic conductivity of unsaturated soils. *Soil Science Society of America Journal*, 44(5):892–898, 1980.

[45] M. W. Farthing and F. L. Ogden. Numerical solution of Richards' equation: A review of advances and challenges. *Soil Science Society of America Journal*, 81(6):1257–1269, 2017.

[46] S. Assouline. Infiltration into soils: Conceptual approaches and solutions. *Water Resources Research*, 49(4):1755–1772, 2013.

[47] Y. Bar-Shalom, X. R. Li, and T. Kirubarajan. *Estimation with applications to tracking and navigation: Theory algorithms and software*. John Wiley & Sons, 2004.

[48] S. Gamse, F. Nobakht-Ersi, and M. A. Sharifi. Statistical process control of a Kalman filter model. *Sensors*, 14(10):18053–18074, 2014.

[49] A. Carrassi and S. Vannitsem. State and parameter estimation with the extended Kalman filter: An alternative formulation of the model error dynamics. *Quarterly Journal of the Royal Meteorological Society*, 137(655):435–451, 2011.

[50] X. Sun, Li Jin, and M. Xiong. Extended Kalman filter for estimation of parameters in nonlinear state-space models of biochemical networks. *PloS one*, 3(11):e3758, 2008.

[51] R. Piché. Online tests of Kalman filter consistency. *International Journal of Adaptive Control and Signal Processing*, 30(1):115–124, 2016.

[52] N. B. Rossello, R. F. Carpio, A. Gasparri, and E. Garone. A novel observer-based architecture for water management in large-scale (Hazelnut) orchards. *IFAC-PapersOnLine*, 52(30):62–69, 2019.

[53] J. Behari. *Microwave dielectric behaviour of wet soils*, volume 8. Springer Science & Business Media, 2006.

[54] G. De Lannoy, P. de Rosnay, and R. H. Reichle. Soil moisture data assimilation. *Handbook of Hydrometeorological Ensemble Forecasting*, 2015.

[55] S. Mazumder. *Numerical methods for partial differential equations: Finite difference and finite volume methods.* Academic Press, 2015.

[56] D. Simon. *Optimal state estimation: Kalman, H infinity, and nonlinear approaches.* John Wiley & Sons, 2006.

[57] R. G. Gibbs. New Kalman filter and smoother consistency tests. *Automatica*, 49(10):3141–3144, 2013.

[58] X. R. Li and Z. Zhao. Practical measures for performance evaluation of estimators and filters. In *Proc. Workshop on Estimation, Tracking, and Fusion—A Tribute to Yaakov Bar-Shalom*, pages 467–480, 2001.

[59] X. R. Li, Z. Zhao, and V. P. Jilkov. Practical measures and test for credibility of an estimator. In *Proc. Workshop on Estimation, Tracking, and Fusion—A Tribute to Yaakov Bar-Shalom*, pages 481–495. Citeseer, 2001.

[60] A. Lippitsch and C. Lasseur. An alternative approach in metrological network deformation analysis employing kinematic and adaptive methods. In *Proceedings of the 12th FIG Symposium, Baden, Germany*, volume 2224, 2006.